

Understanding feedback loops in membrane  
dynamics using a tuneable synthetic system in  
*Saccharomyces cerevisiae*

Rukmini Jonnalagadda

2019

A thesis presented for the degree of  
Doctor of Philosophy in Cell Biology

University of  
**Kent**

School of Biosciences

University of Kent

## Affidavit

I hereby declare that to the best of my knowledge, this PhD thesis titled, "A tuneable synthetic system to study membrane dynamics in *Saccharomyces cerevisiae*" is my own work and all the assistance received in preparing this thesis and sources have been acknowledged.

Rukmini Jonnalagadda

September, 2019

## Acknowledgment

I would like to thank Dr. Chieh Hsu, without whom this project would not have been possible and for all the hours spent on developing the machine-learning scripts and the quantification method used in this thesis. I am also deeply grateful for your guidance and patience, which have made this such an enjoyable experience and have allowed me to develop my own scientific voice and acumen.

I would also like to take this opportunity to thank my family for their kindness and unconditional support. To my parents, I would like to thank my mother and my father for supporting me and encouraging me to make the most out of this opportunity. I would also like to thank my sister, who has been a great source of emotional support and inspiration throughout the last few years.

## Abbreviations

<b>DNA</b>	Deoxyribonucleic acid
<b>GEV</b>	Gal4dbd-ER-VP16 fusion protein
<b>GFP</b>	Green Fluorescent protein
<b>PEG</b>	Polyethylene glycol
<b>PCR</b>	Polymerase Chain Reaction
<b>PH</b>	Plecksterin homology domain
<b>PI(4,5)P<sub>2</sub></b>	Phosphatidylinositol-(4,5)- bisphosphate
<b>PI(3,4,5)P<sub>3</sub></b>	Phosphatidylinositol-(3,4,5)triphosphate
<b>PI3K</b>	Phosphatidylinositol-3- Kinase
<b>p110<sub>αC</sub></b>	Cytosolic version of p110 <sub>α</sub>
<b>p110<sub>αL</sub></b>	Positive feedback version of p110 <sub>α</sub>
<b>p110<sub>αM</sub></b>	Membrane version of p110 <sub>α</sub>
<b>PTEN</b>	Phosphatase and tensin homologue
<b>PTEN<sub>C</sub></b>	Cytosolic version of PTEN
<b>PTEN<sub>L</sub></b>	Positive feedback version of PTEN
<b>PTEN<sub>M</sub></b>	Membrane version of PTEN
<b>rtTA</b>	Reverse tetracycline-controlled transactivator

## Abstract

The spatio-temporal organisation of molecules in a cell plays an important role in regulating important biological processes such as cell differentiation or cell death. Molecular organisation at cell membranes is an important process through which cells carry out crucial functions. For example, at the plasma membrane, molecules that are involved in signal transduction processes form enriched regions on the membrane to allow the cell to respond to changes in its environment. The enrichment of molecules at membranes is thought to be mainly governed by positive feedback; however, as cellular membranes constitute several types of molecules that interact with one another it is difficult to identify what mechanisms trigger the switch between diffused and enriched states at the membrane. Many competing theoretical models have been proposed to describe what governs the switch between the two states but little experimental data is available to validate these models.

The aim of this thesis is to build a quantifiable synthetic system, which is uncoupled from other feedback in the cell so that it can be used to understand the roles of positive feedback at the plasma membrane. To do this, we have constructed a tuneable synthetic system that exploits the absence of PI(3,4,5)P<sub>3</sub> in cellular membranes and the presence of its precursor PI(4,5)P<sub>2</sub> at the plasma membrane of *Saccharomyces cerevisiae* cells. In this thesis, I show that using the catalytic subunit, p110 $\alpha$  and PTEN, we can alter phosphatidylinositol metabolism in *Saccharomyces cerevisiae* cells without observing toxic effects on the cell. I will also introduce the method that was developed to detect and quantify the relative changes in PI(3,4,5)P<sub>3</sub> levels at the plasma membrane using a dual reporter system. A machine-learning algorithm was developed to automate quantification of the differences across cells with different PI(3,4,5)P<sub>3</sub> conditions which is reflected in the *PIP*<sub>3</sub>-Index. Statistical significance of the *PIP*<sub>3</sub>-Index across the population distribution was determined using Mann-Whitney test and significance of bimodality was determined using Hartigan's Dip-test.

Using the methods developed in this study, the simplified positive feedback system, was able to show bistability and hysteresis across the cell population. Cells

---

that contain the positive feedback versions of p110 $\alpha$  and PTEN (two-loop) and had previously encountered high PI(3,4,5)P<sub>3</sub> levels, maintained high levels even after co-expression of p110 $\alpha$  and PTEN in the cell. Significant differences ( $p < 0.05$ ) were observed between the response to co-expression of p110 $\alpha$  and PTEN in cells that previously experienced high PI(3,4,5)P<sub>3</sub> levels, compared to cells that did not experience high PI(3,4,5)P<sub>3</sub>. The difference between the population means of experienced and naïve cells (or cells that did not experience high levels of PI(3,4,5)P<sub>3</sub>) was 20%. Bistability in the cell was associated with a higher range of bimodality observed in the two-loop construct compared to the one-loop construct and hysteresis was observed at high levels of PTEN expression in the two-loop construct. The one-loop construct was made up of a the positive feedback version of p110 $\alpha$  and a cytosolic version of PTEN and did not show significant bistability across experienced and naïve cell populations. This study confirms that positive feedback at the plasma membrane can result in bistability and memory across the population. These results provide insight for future models of molecular organisation at the membrane that should incorporate elements in addition to a two-loop positive feedback.

# Contents

<b>Abstract</b>	<b>4</b>
<b>1 Introduction</b>	<b>19</b>
1.1 Summary	19
1.2 Review of the molecular complexity involved at the plasma membrane	19
1.2.1 The three tiers of plasma membrane organisation	20
Plasma membrane compartmentalisation	20
Mesoscale rafts	21
Dimers, oligomers and complexes	22
1.3 Distinction between hard and soft patterns at the plasma membrane	24
1.3.1 Hard patterns driven by extracellular cues	24
1.3.2 Soft patterns driven by intracellular cues	25
1.4 Review of theoretical models describing pattern formation at the plasma membrane	30
1.4.1 Wave-pinning model yields multiple peaks that may underpin cluster formation at the plasma membrane	31
1.4.2 Turing-type models yield a single sharp peak that may underpin spontaneous pole formation at the plasma membrane	34
1.5 Goals of this project	36
<b>2 Design of the synthetic system</b>	<b>37</b>
2.1 Summary	37
2.2 Introduction to phosphatidylinositols	38
2.3 Literature survey of heterologous expression of PI3K in <i>S. cerevisiae</i>	40

2.3.1	Toxicity observed using p110 $\alpha$ was greater than using p110 $\beta$ subunit . . . . .	40
2.3.2	High expression levels of p110 $\alpha$ showed more toxicity than low expression levels . . . . .	41
2.3.3	Membrane bound of p110 $\alpha$ was associated with more toxicity than cytosolic constructs . . . . .	41
2.3.4	Design considerations of p110 $\alpha$ expression in <i>S. cerevisiae</i> . . .	41
2.4	Components of the system . . . . .	47
2.4.1	Controlling p110 $\alpha$ dynamics at the plasma membrane . . . . .	47
2.4.2	Controlling PTEN dynamics at the plasma membrane . . . . .	48
2.4.3	Dual reporter system to observe membrane dynamics . . . . .	49
2.4.4	Theory of the dual-reporter system . . . . .	50
2.4.5	Machine-learning based quantification method . . . . .	52
<b>3</b>	<b>Building the synthetic system in <i>S. cerevisiae</i></b>	<b>59</b>
3.1	Summary . . . . .	59
3.2	Investigating p110 $\alpha$ toxicity using the GEV system . . . . .	59
3.3	Constructing a robust dual reporter system . . . . .	61
3.3.1	Increased promoter strength resulted in increased detection range of PI(4,5)P <sub>2</sub> binding GFP reporter . . . . .	62
3.3.2	Orientation of PI(3,4,5)P <sub>3</sub> - binding mCherry reporter affected fluorescence signal . . . . .	64
3.3.3	Illustrating <i>P_TEF1</i> , codon optimised PI(3,4,5)P <sub>3</sub> - binding mCherry construct showed increased detection range compared to <i>P_CLN3</i> , non-codon optimised mCherry construct . . . . .	65
3.4	Automated measurement . . . . .	66
3.5	Discussion of building the synthetic system . . . . .	67
3.5.1	Expression of p110 $\alpha$ was tolerated in the cell . . . . .	67
3.5.2	Increased detection range of dual reporter is due to larger amount of reporter available in the cell . . . . .	68

3.5.3	Advantages and limitations of using machine-learning based algorithm . . . . .	69
<b>4</b>	<b>Testing functionality of the components of the system</b>	<b>70</b>
4.1	Summary . . . . .	70
4.2	Quantification of p110 $\alpha$ dynamics at the plasma membrane . . . . .	71
4.2.1	p110 $\alpha_M$ showed highest plasma membrane activity due to basal expression . . . . .	71
4.2.2	Activity due to basal expression of p110 $\alpha_C$ and p110 $\alpha_L$ are comparable . . . . .	72
4.2.3	Induced activity of p110 $\alpha_C$ did not have a significant increase in mCherry at the plasma membrane . . . . .	72
4.2.4	Induced activity of p110 $\alpha_L$ and p110 $\alpha_M$ resulted in high levels of mCherry at the plasma membrane . . . . .	73
4.3	Quantification across the cell population reflected differences observed across the different versions of p110 $\alpha$ . . . . .	73
4.4	PTEN functionality test . . . . .	75
4.5	Quantification of basal expression levels of p110 $\alpha_C$ and PTEN $_C$ . . . . .	78
4.6	Discussion for testing functionality of the components of the system . . . . .	79
4.6.1	Quantification method showed differences in p110 $\alpha$ membrane dynamics. . . . .	79
4.6.2	PTEN component was found to be functional and was used to study plasma membrane dynamics . . . . .	81
4.6.3	PTEN basal activity in cells increases with p110 $\alpha_C$ induction . . . . .	82
<b>5</b>	<b>Understanding bistability at the plasma membrane</b>	<b>84</b>
5.1	Summary . . . . .	84
5.2	Assessment of conditions for bimodality across cell populations . . . . .	84
5.3	The two-loop construct showed ability to behave based on PI(3,4,5)P $_3$ history . . . . .	90
5.4	Bimodality was observed across a larger concentration range in the two-loop construct . . . . .	94

---

5.5	The two-loop construct shows robust response even under leaky expression of $PTEN_L$ . . . . .	94
5.6	Expression of $PTEN_L$ is required for bistable response in two-loop construct . . . . .	96
5.7	Expression of $PTEN_L$ at high levels resulted in hysteresis in the two-loop construct . . . . .	97
5.8	Discussion for understanding bistability at the plasma membrane . . .	99
<b>6</b>	<b>Discussion</b>	<b>105</b>
6.1	Thesis summary . . . . .	105
6.2	The two-loop synthetic system is analogous to the toggle-switch hypothesis . . . . .	105
6.3	The two-loop construct results in all-or-nothing responses at the membrane . . . . .	108
6.4	Increasing non-linearity in the system may result in polarisation at the membrane . . . . .	110
6.5	Future perspectives . . . . .	112
<b>7</b>	<b>Materials and methods</b>	<b>114</b>
7.1	Plastic consumables . . . . .	114
7.2	General glassware . . . . .	114
7.3	Protein gels and buffers . . . . .	114
7.4	DNA ladders and protein markers . . . . .	115
7.5	List of chemicals and reagents . . . . .	115
7.6	stains . . . . .	116
7.7	Media and supplements . . . . .	116
7.8	Stock solutions and media . . . . .	116
7.8.1	Stock solutions . . . . .	116
7.8.2	Media preparation . . . . .	116
	Bacterial media . . . . .	117
	Yeast media . . . . .	117
7.9	Molecular biology commercial kits . . . . .	118

---

7.10	Antibodies . . . . .	119
7.11	Enzymes and enzyme buffers . . . . .	119
7.12	Bacterial and yeast organisms . . . . .	119
7.12.1	Bacterial organaisms . . . . .	119
7.12.2	Yeast organisms . . . . .	120
7.13	Oligonucleotides and primer design . . . . .	120
7.13.1	Primers used for cloning . . . . .	120
7.13.2	Primers for copy number verification . . . . .	122
7.13.3	Sequencing primer . . . . .	122
7.14	External plasmids . . . . .	123
7.15	Software . . . . .	124
7.16	DNA methods . . . . .	124
7.16.1	General cloning strategy . . . . .	124
7.16.2	Plasmids constructed in this study . . . . .	125
7.16.3	Restriction enzyme digestion and DNA fragment purification . . . . .	126
7.16.4	DNA gel electrophoresis . . . . .	126
7.16.5	T <sub>4</sub> - ligation . . . . .	127
7.16.6	Phusion <sup>®</sup> high fidelity DNA polymerase chain reaction . . . . .	127
7.16.7	Quick-Fusion cloning kit . . . . .	129
7.16.8	Heat-shock transformation protocol of chemically competent <i>E. coli</i> cells . . . . .	129
7.16.9	Bacterial colony PCR and Mini-Prep . . . . .	130
7.16.10	DNA concentration and purity determination . . . . .	131
7.16.11	DNA sequencing . . . . .	131
7.16.12	LiAc/carrier DNA/ PEG transformation protocol for plasmid integration to <i>S. cerevisiae</i> genome . . . . .	132
7.16.13	Glycerol stocks of yeast strains . . . . .	133
7.16.14	Haploid strains constructed in this study . . . . .	133
7.16.15	Copy number determination of integrated plasmid to <i>S. cere-</i> <i>visiae</i> genome . . . . .	133
	Copy number determination using quantitative PCR (qPCR) . . . . .	133

Calculating the number of copies using $C_q$ values . . . . .	135
7.16.16 Diploid strains constructed for this study . . . . .	136
Yeast mating . . . . .	136
7.17 Inducing protein expression using synthetic promoters . . . . .	139
7.17.1 Inducing expression using the GEV system . . . . .	139
7.17.2 Inducing expression of TET-ON system . . . . .	139
7.18 Yeast growth rate analysis . . . . .	140
7.18.1 Promoter strength analysis . . . . .	141
7.19 Fluorescence microscopy and quantification method . . . . .	142
7.19.1 Sample preparation . . . . .	142
7.19.2 Wide-field microscope Set-up and Image acquisition . . . . .	142
7.19.3 Setting scale-bar on ImageJ . . . . .	142
7.20 Image quantification . . . . .	143
7.20.1 Machine learning based algorithm for quantification of cells . . . . .	143
7.20.2 Hysteresis experiments . . . . .	143
7.21 Protein methods . . . . .	144
7.21.1 Preparation of cell- free lysate . . . . .	144
7.21.2 Protein quantification using UV-Spectrometer . . . . .	144
Equation used to calculate protein concentration . . . . .	144
7.21.3 Gel electrophoresis and wet-transfer procedure . . . . .	144
7.21.4 Immunoblotting for detection of Protein . . . . .	145
<b>A Review of Phosphoinositol metabolism in <i>S. cerevisiae</i></b> . . . . .	<b>147</b>
A.0.1 PI(3)P and PI(3,5)P <sub>2</sub> are present on membranes involved in sensing environmental changes in the cell . . . . .	147
A.0.2 PI(4)P and PI(4,5)P <sub>2</sub> are present on membranes that are in- volved in sensing growth conditions . . . . .	148
<b>B Source Code</b> . . . . .	<b>151</b>
B.1 Image segmentation . . . . .	151
B.1.1 Image restructuring .tiff → .jpeg . . . . .	151
B.1.2 Identification of squares containing cells in the image . . . . .	153

---

B.1.3	Data import . . . . .	159
B.1.4	Generating cell profiles . . . . .	160
B.1.5	Discard ROI's that are too small . . . . .	165
B.1.6	Boundary detection of cell . . . . .	166
B.1.7	Discard non-circular shaped ROI's . . . . .	168
B.1.8	Add selection to ROI manager . . . . .	169
B.2	Identification of redundant cells in GFP channel . . . . .	170
B.3	Quantification of $PIP_3$ -Index . . . . .	173
B.3.1	File import . . . . .	173
B.3.2	Cells defined by mCherry channel . . . . .	173
B.3.3	Cell profiles defined by mCherry channel . . . . .	173
B.3.4	Cells defined by GFP channel . . . . .	174
B.3.5	Cell profiles defined by GFP channel . . . . .	174
B.3.6	Identifying cells for quantification . . . . .	174
B.3.7	Calculating $PIP_3$ -Index . . . . .	175

# List of Figures

1.1	Schematic representation of the three tiers that make up the plasma membrane. . . . .	23
1.2	Distinction between two types of molecule enrichment at the plasma membrane. . . . .	29
2.1	Structure of a phosphatidylinositol molecule. . . . .	39
2.2	Schematic diagram of PTEN mutant cytosolic construct (PTEN <sub>C</sub> ). . .	48
2.3	Geometric model showing changes in cell shape due to increasing plasma membrane signal. . . . .	51
2.4	Training data used to retrain Mobilenet v2 model. . . . .	53
2.5	Machine-learning based quantification workflow. . . . .	54
2.6	Illustration of application of Tensorflow Mobilenet v2 model for image segmentation. . . . .	55
2.7	Identification of cell boundary in segmented regions. . . . .	55
2.8	Example of of mCherry and GFP signal profile plots across a single cell with low PI(3,4,5)P <sub>3</sub> levels. . . . .	56
2.9	Actual and theoretical ratio plots between mCherry and GFP average profile plots. . . . .	57
2.10	Overview of the components of the system. . . . .	58
3.1	Effect of p110 $\alpha$ expression on relative doubling time of cells. . . . .	61
3.2	Effects of p110 $\alpha_L$ expression, compared to DMSO control. . . . .	61
3.3	Effect of $\beta$ -estradiol treatment on control cells. . . . .	62
3.4	Comparing constitutive promoter strength. . . . .	63

3.5	Effect of promoter strength on detection range of GFP-2XPH(PLC $\delta$ ) construct. . . . .	64
3.6	C-terminus fusion of PH(AKT) domain diminished mCherry signal in the cell. . . . .	65
3.7	Representative plot profiles comparing PI(3,4,5)P <sub>3</sub> - binding mCherry constructs. . . . .	66
3.8	Cell boundary detection between both mCherry and GFP channels. . . . .	67
4.1	Schematic diagram illustrating membrane dynamics of different p110 $\alpha$ versions. . . . .	71
4.2	Representative profile plots of basal expression of the different versions of p110 $\alpha$ used in this study. . . . .	72
4.3	Representative plot profiles of induced expression of the different versions of p110 $\alpha$ used in this study. . . . .	73
4.4	Distribution plots of <i>PIP</i> <sub>3</sub> -Indexes across p110 $\alpha$ cells. . . . .	75
4.5	Copy number determination of PTEN <sub>C</sub> cells. . . . .	77
4.6	Effect of copy number on amount of GFP observed at plasma membrane in cells co-expressing p110 <sub>L</sub> and PTEN <sub>C</sub> . . . . .	77
4.7	Distribution plots showing effect of PTEN <sub>C</sub> copy number on <i>PIP</i> <sub>3</sub> -Index. . . . .	78
4.8	Induction of synthetic promoters showed >2- fold difference compared to basal expression. . . . .	79
5.1	Assessment of bimodality across different constructs. . . . .	86
5.2	Representative images of cells showing large differences between conditions in the one-loop construct. . . . .	87
5.3	Representative images of cells showing bimodalty in the two-loop that were induced to co-express p110 $\alpha$ <sub>L</sub> and PTEN <sub>L</sub> . . . . .	88
5.4	Representative images of cells showing little differences across all three conditions in cells containing p110 $\alpha$ <sub>L</sub> and PTEN <sub>M</sub> . . . . .	89
5.5	Experimental set-up to test memory in one- loop and two- loop constructs. . . . .	91

5.6	Immunoblot showing that that growth conditions for experienced cells did not interfere with memory test. . . . .	91
5.7	Two-loop construct showed ability to retain information about PI(3,4,5)P <sub>3</sub> history. . . . .	92
5.8	Distribution plots of two-loop cells across initial and hysteresis condition.	92
5.9	Representative images of hysteresis experiment using one-loop construct.	93
5.10	Distribution plots of cells one-loop construct across initial and hysteresis condition. . . . .	93
5.11	Effect of $\beta$ -estradiol concentration and leaky expression of PTEN <sub>C</sub> on the significance of bimodality in cell response across naïve and experienced cells. . . . .	95
5.12	Effect of $\beta$ -estradiol concentration and leaky expression of PTEN <sub>L</sub> on the significance of bimodality in cell response across naïve and experienced cells. . . . .	96
5.13	Significance of bimodality across distribution plots between experienced and naïve cell history in one-loop and two-loop constructs. . . .	97
5.14	Response to $\beta$ -estradiol concentration gradient in one-loop cells, at leaky expression of PTEN <sub>C</sub> . . . . .	98
5.15	Response to $\beta$ -estradiol concentration gradient in two-loop cells, at leaky expression of PTEN <sub>L</sub> . . . . .	99
5.16	Effect of low induction of PTEN <sub>L</sub> expression on bimodality in response to concentration gradient of $\beta$ -estradiol in naïve and experienced two-loop cells. . . . .	100
5.17	Effect of high induction of PTEN <sub>L</sub> expression on bimodality in response to concentration gradient of $\beta$ -estradiol in naïve and experienced two-loop cells. . . . .	101
5.18	Comparison of two-loop naïve and experienced cell response to $\beta$ -estradiol concentration at low PTEN <sub>L</sub> expression. . . . .	102
5.19	Comparison of two-loop naïve and experienced cell response to $\beta$ -estradiol concentration at high levels of PTEN <sub>L</sub> . . . . .	103

---

6.1	Development of the blue-light control system. . . . .	113
7.1	Schematic diagram illustrating open reading frame plasmid design. . .	124
A.1	Summary of phosphatidylinositol metabolism in <i>S. cerevisiae</i> . . . . .	150

# List of Tables

1.1	Literature review of hard pattern formation. ECM = extracellular matrix . . . . .	27
1.2	Literature review of Soft patterns . . . . .	28
1.3	Examples of Feedback by GEF activation . . . . .	32
1.4	Examples of feedback by inhibition of GAP activation . . . . .	32
2.1	Literature survey of studies that introduce p110 $\alpha$ catalytic domain to <i>S. cerevisiae</i> cells. . . . .	43
2.2	Literature survey of studies that introduce p110 $\alpha$ catalytic domain to <i>S. cerevisiae</i> cells (Continued). . . . .	44
2.3	Literature survey of studies that introduce p110 $\alpha$ catalytic domain to <i>S. cerevisiae</i> cells (Continued). . . . .	45
2.4	Literature Survey of studies that introduce p110 $\alpha$ catalytic domain to <i>S. cerevisiae</i> cells (Continued). . . . .	46
6.1	Examples of toggle-switch hypothesis for polarisation at the plasma membrane. . . . .	109
7.1	Stock Solutions used in this Study . . . . .	117
7.2	Amounts of drop- out supplement added to media (w/v) . . . . .	118
7.3	Commercial molecular biology kits used in this study . . . . .	118
7.4	Background strains used in this study . . . . .	120
7.5	Phusion primers used to amplify insert sequences for plasmid construction . . . . .	121
7.6	qPCR primers used to determine copy number of integrated plasmids	122

---

7.7	List of External Plasmids used in this study . . . . .	123
7.8	List of Plasmids constructed in this study and cloning notes. <b>V:</b> plasmid vector used and <b>I:</b> describes the insert DNA modules. For insert modules that were used for Quick-Fusion cloning kit, see section 7.13.1. . . . .	125
7.9	Concentration of agarose used to resolve DNA fragments . . . . .	127
7.10	Diploid Strains . . . . .	136
7.11	Diploid strains (Continued) . . . . .	137
7.12	Diploid strains (Continued) . . . . .	138
7.13	Growth conditions used to study maintenance of memory. . . . .	143
7.14	Conditions used for immunoblotting detection of proteins. . . . .	146

# Chapter 1

## Introduction

### 1.1 Summary

This chapter introduces the different theoretical models that describe the enrichment of molecules at the plasma membrane. Due to the complexity and diversity involved in the regulation of enrichment of molecules at cellular membranes, I find it easier to classify enrichment of molecules at the plasma membrane into two major classes: hard and soft patterns. I propose that the formation of hard patterns are those driven by physical cues that come from outside of the cell (eg: cell-to-cell interactions), where these patterns are dynamically formed throughout the lifespan of the cell. Meanwhile, soft patterns are produced as a result of physical cues from within the cell and are formed within a sub fraction of the entire cell's lifespan (<1 minute) but can persist for a significant proportion of the cell's lifespan (eg: polarisation). The distinction becomes important as the formation of hard patterns is more consistent and measurable than soft patterns.

### 1.2 Review of the molecular complexity involved at the plasma membrane

The plasma membrane is a biological membrane that spans the entire surface area of the cell and acts as an interface between the inside of the cell and its environment. Traditionally, the plasma membrane is often described as a barrier against the en-

vironment but this does not take into consideration that it is fluid and responsive to environmental and internal changes [72]. The molecular complexity involved and the high turnover of molecular reactions at the plasma membrane make it difficult to study how molecules behave at the plasma membrane. Consequently, there remain many open questions about how molecules at the plasma membrane interact with each other as well as interact with molecules within the cell. One question worth considering, is how does a highly diluted molecular species within the cell, behave at the plasma membrane to control cell fates? To determine why there is a lag in our understanding we first need to appreciate the molecular complexity of the plasma membrane, which is made up of many diverse molecules that interact with each other to maintain structural and functional integrity. Previous studies show that the diverse molecules that make up the plasma membrane can be grouped based on their function resulting in three tiers of organisation [59].

### 1.2.1 The three tiers of plasma membrane organisation

The notion that molecules at the plasma membrane are organised into three tiers is based on previous studies [59]. The structure and function appear to be highly hierarchical and can be organised based on increasing molecular complexity (as represented in Figure 1.1). The three tiers include: plasma membrane compartments (40-300nm), mesoscale raft domains (2-20nm) and dimers, oligomers and greater complexes formed by membrane-associated proteins (2-10nm). Feedback loops across the three tiers couple together to form the plasma membrane where molecules switch between diffused states in the cytosol/ plasma membrane and enriched states at the plasma membrane to control cell fates.

#### **Plasma membrane compartmentalisation**

Plasma membrane compartments describe the most basic and largest tier of organisation, that is characterised by reduced free diffusion of molecules in a compartment or region of the plasma membrane. This tier is made up of the phospholipid membrane, transmembrane proteins and the actin cytoskeleton meshwork. This level of organisation is also described as the picket fence model of the plasma membrane.

The actin membrane meshwork skeleton acts analogous to fences and transmembrane proteins act analogous to pickets, together they act as a barrier against free diffusion of plasma membrane components (phospholipids, G-coupled protein receptors, etc.) [59]. The diffusion constants of phospholipids have been shown to increase as a result of disrupting the actin cytoskeleton (eg:CK-666 or Latrunculin B treatments) [63]. The increase in diffusion constants suggests that the first tier of organisation controls the structure of the plasma membrane through cytoskeletal dynamics. Positive and negative feedback loops between the actin cytoskeleton meshwork and transmembrane proteins result in concave and convex protrusion at the plasma membrane, respectively. These protrusions result in structural changes that are required for cell growth and development [103].

### **Mesoscale rafts**

This tier is made up of membrane-associated molecules that accumulate and interact with each other in a specific region of the membrane. The enriched regions on the membrane are restricted to membrane compartments and are referred to as rafts. These rafts are stabilised by a cholesterol molecule and thus this level of organisation is closely linked to the lipid raft hypothesis. Lipid rafts are biochemically defined after extraction from the detergent resistant fraction of a gradient centrifuged sample of the plasma membrane that is treated with cold non-ionic detergents [64]. However, the variation in the composition, size and persistence times observed have resulted in controversy about the existence of lipid rafts in the first place [93]. Nevertheless, studies report quantitative data of rafts observed on the plasma membrane of cells using advanced imaging techniques [59]. Mesoscale rafts are predominantly made-up of small G-protein coupled receptors, such as Ras-GTPases or Rho-GTPases, and cholesterol to make up regions that tend to be highly organised compared to the rest of the membrane [107]. These highly organised regions are often described as the liquid-ordered phase ( $L_O$ -phase) and the disorganised regions of the membrane are known as the liquid disordered phase ( $L_D$ -phase) [93]. Mesoscale rafts are  $\approx 40$  nm in diameter but undergo coarsening, or coalescence to result in larger rafts. Depending on the cell type, larger rafts can grow to several hundred nanometers in diameter.

The dynamic formation of mesoscale rafts at the plasma membrane is the basis upon which I define soft pattern formation.

### **Dimers, oligomers and complexes**

In multicellular organisms, such as in mammalian cells, mesoscale rafts also contain single membrane pass proteins known as tyrosine kinases that initiate cell signalling after dimerisation at the plasma membrane (Section 1.3.1). This level of organisation is also referred to as the thermo-lego model, which describes that cell signalling through mesoscale rafts is stabilised after thermal stability is achieved through complex formation of the transmembrane proteins [93]. In this model, the transmembrane proteins are referred to as the pegs of a lego piece that can fit into each other and the mesoscale rafts acts as the base. The binding of the extracellular regions of transmembrane proteins is thought to reduce fluidity across the plasma membrane, reinforcing feedback loops between the cytoskeleton and increasing coalescence of mesoscale rafts resulting in large ( $\approx 100 \mu\text{m}$  in diameter) patterns on the membrane. The physical or chemical disruption results in decoupling of feedback loops across the three tiers and can result in the progression of programmed cell death. The enrichment of molecules at the plasma membrane due to binding of transmembrane proteins forms the basis of defining hard patterns.

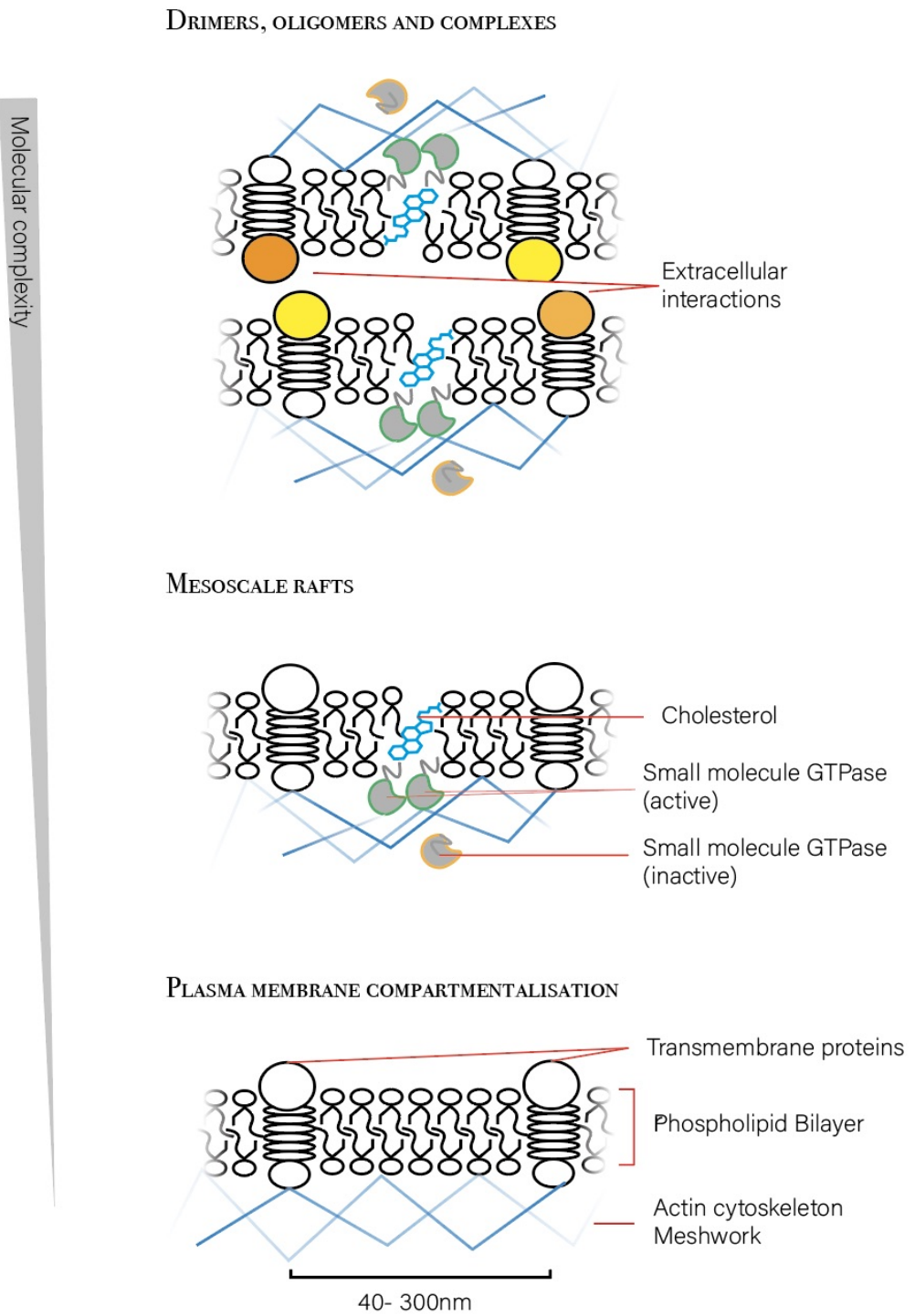


Figure 1.1: Schematic representation of the three tiers that make up the plasma membrane.

### 1.3 Distinction between hard and soft patterns at the plasma membrane

This section reviews some of the experimental evidence outlining the distinction between hard and soft patterns that can be observed at the plasma membrane along with the typical responses that they govern. As previously mentioned, the distinction is based on the physical cues that result in the formation of these patterns. Hard patterns refer to self-organising structures that are dynamically formed throughout the cell's lifespan whereas soft domains are formed from cues driven from within the cell, taking only a few seconds to form. Both hard and soft patterns are formed by diffusion and positive and negative feedback loops that theoretically describe typical patterns that can be observed.

Patterns at the plasma membrane typically include travelling waves and polarisation. Localised pulses are generated by negative feedback loops that result in an accumulation of molecules at specific regions of the cell that is close to the source (eg:  $\text{Ca}^{2+}$  pulse from inositol- triphosphate receptor at the endoplasmic reticulum [13]). When there is a positive feedback that is strong enough to overcome the negative feedback loop, allowing the formation of several local pulses that move away from the source, a travelling wave is produced [108]. Coupling of two or more positive feedback mechanisms result in the enrichment of a particular molecular species at the plasma membrane to result in polarisation. As localised pulses are almost never used to describe pattern formation at the plasma membrane it may suggest that positive feedback plays an important role at the plasma membrane.

#### 1.3.1 Hard patterns driven by extracellular cues

Hard patterns are formed through extracellular spatial cues such as binding of single pass transmembrane proteins to other receptors on the surface of the same cell, on the surface of other cells or to components of the extracellular matrix (ECM). Examples of hard patterns can be seen in extracellular interactions that are involved in cell-to-cell and cell-to-extracellular matrix (ECM) adhesion as well as in immune cell recognition (Table 1.1). In cell-to-cell and cell-to- ECM adhesion, formation of hard

patterns is driven by cell adhesion molecules (CAMs) that have charged extracellular regions, which form complexes to proteins by strong electrostatic interactions across the whole extracellular domain of the protein [18, 74]. These complexes are stabilised by  $\text{Ca}^{2+}$  ions at the plasma membrane, reinforcing feedback mechanisms between the cytoskeleton and the plasma membrane through PLC- dependent signalling. Receptors across two cells may bind to each other without the formation of any characteristic structures, which will only develop after coupling with the cytoskeleton [74]. After coupling with cytoskeleton components, these patterns persist as long as the cell is alive and are affected only by physical or chemical disruption. Disruption of hard patterns results in loss of signalling and function of the cell, which results in programmed cell death [58]. Therefore, hard patterns formation is driven through extracellular interactions of membrane-bound proteins and the accumulation of ten or more signalling molecules after binding of extracellular regions of transmembrane proteins, resulting in large micrometer-scale patterns that govern important cell fates.

### 1.3.2 Soft patterns driven by intracellular cues

The mechanism through which soft patterns form remain unclear but are thought to form as a result of physical cues from within the cell. Signalling from within the cell results in a self-perpetuating reaction that gives rise to the aggregation of highly diluted molecular species from the cytosol to the plasma membrane. Soft patterns can result in travelling waves or poles as result of the mechanism through which they are formed. These travelling waves are observed as clusters of molecules at the plasma membrane and are hereafter referred to as clusters.

A single positive feedback is suggested to govern cluster formation of Ras-GTP. Ras-GTP is a small molecule G-protein coupled receptor that is found in the cytosol in its inactive, GDP bound form and is converted to its membrane bound GTP associated form. The inactive Ras-GDP is present at very low concentration in the cytosol of the cell and differential expression of its guanadine exchange factor (GEFs), which converts the inactive version to the active form and its GTP-associated protein (GAPs), which is required to deactivate active Ras, within the cell results in different

activation responses of Ras-GTP [25]. The GEF, SOS (Sons of Sevenless) is known to activate a molecule of Ras by exchanging bound GDP for GTP. A single molecule of SOS itself has very weak guanadine nucleotide exchange activity and is known to have a second Ras binding site that is adjacent to the site of GEF activity. Binding of RasGDP to this site results in  $\approx 5$  fold increase in GEF activity but binding to Ras-GTP results in  $\approx 75$  fold increase in GEF activity [37]. In this way a positive feedback is established resulting in clusters of Ras molecules at the plasma membrane. The persistence times for such soft patterns tend to be a few seconds as they rapidly diffuse away from the structure (Table 1.2). Therefore, internal physical cues that establish positive feedback between Ras-GTP and GEF are thought to govern cluster formation whereas, rapid diffusion of membrane bound molecules result in loss of cluster formation.

The interplay between multiple positive feedback loops may result in the traveling wave becoming a pole as suggested in the case of Cdc42-GTP in *S. cerevisiae* [30]. Cdc42 molecules belong to the Rho super family of small G-protein coupled receptors. They are informally referred to as master regulators of polarisation as they switch from unpolarised to polarised states at the plasma membrane as well as between inactive and active forms. The inactive form of Cdc42, is found in the cytosol and is bound to GDP and upon activation by its GEF, Cdc24, it is activated after exchanging its GDP for GTP and binds to the plasma membrane. The individual Cdc42-GTP molecules localise to the membrane to form clusters to initiate polarisation. These active molecules recruit more active Cdc42-GTP via interactions with Cdc24 and Bem1, a scaffolding protein. The growing domain is maintained under dynamic equilibrium as there is rapid recycling from the cytosolic pool to the membrane [56]. Eventually, domains grow in size while other domains become extinct and the largest domain out competes the others. The positive feedback that is thought to drive polarisation is established between the inactive and active forms of Cdc42 [70].

Table 1.1: Literature review of hard pattern formation. ECM = extracellular matrix

<b>Function</b>	<b>Extracellular inter-action</b>	<b>Diameter of pattern</b>	<b>Process</b>	<b>Ref.</b>
Cell-to cell adhesion between neurons (Neuronal-cell adhesion molecules)	Sialylation of residues in extracellular region has been shown to affect complex formation.	100 $\mu$ m in diameter; $\approx$ 10 molecules	Recruits molecules to initiate anti-apoptotic signalling.	[109]
Cell-to-extracellular matrix adhesion through integrins (leukocyte specific Integrins, LFA-1)	Extracellular region binds through a short amino acid (RGD) sequence present in ECM components.	50-70nm; $\approx$ 6 molecules	Pattern forms after ligand binding to recruit molecules to initiate anti-apoptotic signalling from the focal adhesion complex. Cell signalling from the focal adhesion complex in turn reinforces the connection between the membrane and actin cytoskeleton.	[40]
Cell-to-cell recognition in Dendritic cells	Receptors (eg: DC-SIGN) form large patterns when bound to small pathogens (eg: viruses)	70-160nm $\approx$ 10 molecules	Domains and recruit clatherin molecules to initiate phagocytosis.	[40]

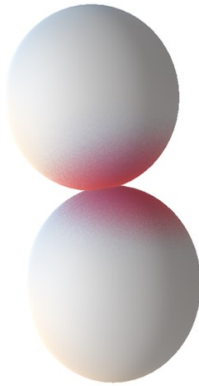
Table 1.2: Literature review of Soft patterns

Function	Soft pattern	Mechanism/ Model	Diameter and formation time	Process	Ref.
Cell-cycle progression Ras-GTPase in mammalian cells	Clusters	Positive feedback loop established by GEF, SOS and inactivation by GAPs result in patterns on the membrane.	9nm; containing 4-10 molecules per cluster; $\approx 0.1-1s$	Activates MAPK cascade for cell cycle progression	[47]
Cell-cycle progression by PKC- $\alpha$ in mammalian cells	Clusters	Allosteric regulation of PKC- $\alpha$ by $Ca^{2+}$ at the plasma membrane increases PKC- $\alpha$ cluster formation.	$\approx 25nm$ persists for $< 2s$	PKC $\alpha$ clusters at the plasma membrane result in the inactivation of p27 cyclin-dependent kinase, resulting in cell proliferation.	[94]
Cell Polarisation: Cdc42-GTP in <i>S. cerevisiae</i>	Poles	Positive feedback loop resulting in substrate-depletion forms one large cluster at the beginning of G2- Phase.	2nm; form within 2 minutes	Clusters become poles at a specific time point giving rise to new bud formation.	[44]
Cell Polarisation: PI(3,4,5)P <sub>3</sub> in <i>D. discoideum</i>	Poles	Mutual inhibition between PI(3,4,5)P <sub>3</sub> and PTEN positive feedback loops resulting in activator-inhibitor type dynamics in response to cAMP gradient.	10-20 $\mu m$ ; 30-60s	Poles result in cell growth and chemotaxis.	[65]

## Enrichment of molecules at the plasma membrane

### Hard Patterns

Formed through extracellular contact interactions resulting in large structures that dynamically form throughout the cell's lifespan.



eg: **Neuronal cadherin adhesion molecules (N-CAMs)**

>70 nm in diameter

Structure dynamically forms until contact is lost

### Soft Patterns

Formed through contact interactions from within the cell resulting in structures that form within a sub fraction of the cell's lifespan.

#### Clusters

The co-existence of many small clusters that do not coalesce to form a larger structure



eg: **Ras- GTPase**

~9nm in diameter

Forms within 20 seconds and persists for less than a 2 seconds.

#### Pole

Formed when small clusters coalesce to form a larger structure



eg: **Cdc42- GTPase**

~2nm in diameter

Forms within 40 seconds and persists for > 20hours

Figure 1.2: Distinction between two types of molecule enrichment at the plasma membrane.

## 1.4 Review of theoretical models describing pattern formation at the plasma membrane

Based on the internal cues from inside the cell, clusters may coalesce to form poles. Let,  $u$  and  $v$  represent the active-membrane bound and inactive, cytosolic version of a molecule, respectively then the rate of change of  $u$  and  $v$  with respect to time in a well-mixed system can be expressed as:

$$\frac{du}{dt} = av - bu \quad (1.1)$$

and,

$$\frac{dv}{dt} = bv - au \quad (1.2)$$

where,  $a$  and  $b$  are the activation and inactivation rates, respectively and  $u+v = w = \text{constant}$ . In the case of GTPase,  $a = a(u, \dots)$  is the rate of GEF-mediated activation and  $b = b(u, \dots)$  is GAP-mediated deactivation. In general, either  $a$  or  $b$  must be non-linear in nature such that there is bistability in the system i.e., there is a sharp transition from one stable state to the other. The non-linearity can be described by either cooperativity or zero-order ultrasensitivity. However, the well mixed system does not describe the biological situation where there is a clear spatial solution as a result of differences in the diffusion rate between the inactive and active forms of the GTPase.

Introducing diffusion to the system can give some insight on the spatial behaviour that is observed in the cell. The rates of change in  $u$  and  $v$  with respect to time can be represented as:

$$\frac{\partial u}{\partial t} = D_u \frac{\partial^2 u}{\partial x^2} + F(u, v) \quad (1.3)$$

and,

$$\frac{\partial v}{\partial t} = D_v \frac{\partial^2 v}{\partial x^2} - F(u, v) \quad (1.4)$$

where,  $F(u, v)$  describes the biochemical interconversion of  $u$  and  $v$ . As the inactive form does not participate in signalling directly, its availability only affects

activation of  $u$  such that,

$F(u,v)$  = activation rate of  $u$  - inactivation rate of  $u$

$$\Rightarrow F(u,v) = f(u)v - g(u) \quad (1.5)$$

Here, we assume that the rate of protein synthesis of  $v$  is much slower than the rate of conversion of  $v$  to  $u$  and thus, the mass is conserved and the total amount of GTPase,  $M = \int (u + v)dx$  is a constant over time. Therefore, the local depletion of  $v$  is quickly replenished because the  $D_v$  in the cytoplasm is at least two-orders greater than  $D_u$ . As mass is conserved in the system, local depletion will eventually result in global depletion of  $v$  impeding further growth of  $u$  (Equation 1.5). At this condition, the system has reached steady state where the reaction and diffusion must be balanced at all local positions of  $x$ :

$$0 = D_u \frac{\partial^2 u}{\partial x^2} + F(u,v) \quad (1.6)$$

and,

$$0 = D_v \frac{\partial^2 v}{\partial x^2} - F(u,v) \quad (1.7)$$

Equations 1.6 and 1.7, are used to describe the peak shape of  $u(x)$  and substrate level  $v(x)$  at steady-state. The model describing the peaks that are developed using these models is known as the Mass conserved Activator Substrate model (MCAS) [19]. Using these equations, we can attempt to understand why some soft patterns develop to form clusters while others form poles. To do this, we consider two situations where positive feedback is established by activation of  $u$ ,  $f(u)$  or the inhibition of the inactivation of  $u$ ,  $g(u)$  (Table 1.3 and 1.4).

#### 1.4.1 Wave-pinning model yields multiple peaks that may underpin cluster formation at the plasma membrane

Wave-pinning behaviour relies on bistable kinetics to produce membrane patterns with multiple distinct phases or clusters at the plasma membrane [70]. The model considers a GTPase molecule, where a membrane bound molecule positively feeds

Table 1.3: Examples of Feedback by GEF activation

	Function	Ref.
Simple Turing Model	$f(u) = au^2$	[19]
	$g(u) = bu$	
Goryachev's simplified model	$f(u) = au^2 + cu$	[44]
	$g(u) = bu$	
Mori's wave pinning model	$f(u) = \frac{au^2}{(1 + ku^2)}$	[70]
	$g(u) = bu$	

Table 1.4: Examples of feedback by inhibition of GAP activation

	Function	Ref.
Otsuji's Model I	$f(u) = 1$	[76]
	$g(u) = \frac{bu}{(1 + u)^2}$	

back on itself resulting in a wave-like response that abruptly stops growing (or pinned) due to the local depletion of the inactive molecule in the cytosol. Since these clusters do not readily compete with each other (under the assumption of mass conservation) they quickly disappear in the absence of any other spatial cues and this is often described as meta-stability [70]. Rapid formation of Ras-GTPase clusters as a result of random fluctuations in the cell and short persistence time is a well-studied phenomenon in mammalian cells (1.2). Hysteresis, or the ability of

the system to exist in a state depending on the history of the system has also been well characterised in mature T-cells, where Ras-signalling is particularly high after intracellular fluctuations caused by the activation of antigen-receptors [26]. Taken together, experimental and modelling results suggest that wave-pinning behaviour may underpin the mechanism through which clusters are formed.

The wave-pinning model may also describe polarisation provided that there is a very large spatial perturbation, which may be more relevant in gradient-sensing cells. Here, the two states describe unpolarised and polarised states of a molecule in the cell, where polarisation remains even after the stimulus is removed [70]. The wave-pinning equation suggests that there is saturation level ( $u_{sat}$ ) in  $F(u,v)$  due to the activation of  $u$  and depletion of  $v$  (Table 1.4). When the protein content  $u_{max}$  is less than  $u_{sat}$ , then  $F(u,v)$  becomes similar to turing-type model where multiple sharp top peaks compete with each other to eventually form a large pole. When the  $u_{max}$  approaches  $u_{sat}$ , then the multiple broad peaks form and undergo coarsening to develop fewer broader peaks that do not form a pole at the plasma membrane [70]. To form a single pole at the plasma membrane, the model requires a drastic perturbation in which 50% of the GTPase in one peak was transferred to the other [19]. In live cells, the drastic perturbation may be due to gradient-sensing that is well studied in both *Dictostelium discodium* [86] and on *Schizosaccharomyces pombe* [8]. In both organisms, several clusters develop to co-exist across the plasma membrane but eventually form a single large pole in response to an external chemical gradient, which persist for several hours even after the gradient is removed. These observations are consistent with wave-pinning based models because it implies that transient patterns that form to initiate polarisation do not compete against each other but extrinsic noise (stimuli) that governs the switch between non-polarised and polarised states [36]. The effects of extrinsic noise overlaps with the assumption of turing-type models, which start with a spatially inhomogenous system.

### 1.4.2 Turing-type models yield a single sharp peak that may underpin spontaneous pole formation at the plasma membrane

Turing-type reactions are well known for their ability to form multiple-peaks that are spatially homogeneous in a system at steady state, which can be destabilised by a spatially inhomogeneous perturbation, such as an external chemical gradient or internal flux of certain proteins. The mechanism is based on two processes having two different spatial characteristics: a slow diffusing local activator and a fast diffusing global inhibitor or substrate. The activator-inhibitor type reactions produce a pattern where the activator and inhibitor peaks coincide. The activator-substrate depletion type reactions results in a pattern where the activator and substrate are out of phase with each other. Assuming mass conservation, models that use activator-inhibitor type include Otsuji's Model I and substrate-depletion type reactions include the simple Turing-type and Goryachev's simple model (Table 1.3 and 1.4), respectively. Both types of reactions are used to describe polarisation leading to the question of whether a fast acting global inhibitor or fast diffusing global substrate underpins the mechanism of polarisation.

Similar to Mori's wave-pinning model, Otsuji's Model I shows saturation kinetics that suggests that there is some threshold level of  $u$ ,  $u_{sat}$  at which the turing-type behaviour is observed. When  $u_{max}$  is lower than  $u_{sat}$ , multiple clusters arise that co-exist and do not form a pole. On the other hand at concentrations approaching  $u_{sat}$ , the system becomes similar to a Turing type model [76]. This is supported by experimental data showing that if the amount of polarising molecule, such as Cdc42-GTP in yeast, is too low then polarisation is not observed in the cell and the loss in polarity is associated with a loss in competition between clusters that precedes polarisation [98]. Individual Cdc42-GTP molecules localise to the membrane to form clusters (or clans) to initiate polarisation. These active molecules recruit more active Cdc42-GTP via interactions with its GEF, Cdc24 and Bem1 scaffolding protein. The growing cluster is maintained under dynamic equilibrium as there is rapid recycling from the cytosolic pool to the membrane. Eventually, clusters grow in size while other clusters become extinct and the largest cluster out competes the others and

this is commonly referred to as the "winner-takes-all" mechanism [50]. When the concentration is too low, the inactivation of Cdc42-GTP is greater than any one cluster's ability to further recruit molecules which produces multiple clusters that do not form a single pole [98]. The switch to polarisation however remains difficult to prove experimentally as it is described to spontaneously occur within  $\approx 20$ s and in this way both Mori's wave-pinning model and Otsuji's Model I are limited due to the lack of experimental data showing  $u_{max} \rightarrow u_{sat}$ .

The activator-substrate depletion type reactions have been found to be highly attractive in supporting the winner-takes-all mechanism in Cdc42 polarisation as described using the simple Turing-type reactions (Table 1.4). In these models there is a characteristic size,  $L$ , of the cluster that forms due to the difference in diffusion rates between the activator and the substrate. When, the cluster size is larger than the characteristic size then, a single peak (a pole) forms as the cluster grows until no more substrate is globally available to the system [19]. Here, the Simple Turing Model becomes analogous to the Mori's wave pinning model, where the wave is pinned at some level when the substrate is depleted and the depletion of global substrate levels presents bistable characteristics in the system [19]. Therefore, it becomes apparent that both wave-pinning and Turing-type models compete to describe polarisation in the cell and that transition between the two behaviours is based on parameter choice. This is supported by the Goryachev's simplified model (Table 1.4), where Wave-pinning behaviour is observed when cluster size is much less than  $L$ . where the cluster size is dependent the concentration of  $u$  but as the concentration increases to greater than  $L$ , Turing-type behaviour is observed [44]. The latter condition may be used to describe the formation of two Cdc42-GTP poles is observed in *Ashbya gossypii* [100]. Nevertheless, strong experimental support for the transition between wave-pinning and Turing-type behaviour in polarisation remains lacking.

## 1.5 Goals of this project

Theoretical models describing the enrichment of molecules at the plasma membrane suggest the need for positive feedback between two mutually exclusive species. As described in this chapter, enrichment of molecules at the plasma membrane is not a well-understood process and consequently the competing models that describe pattern formation seem to confuse any progress that is made in this direction. The problem arises in not only the unification of these different models but also the lack of experimental data to support these models. The common motifs identified across the theoretical models is that they often describe the switch between diffused and enriched clusters of the molecule (Mori's wave-pinning model) or a switch between unpolarised and polarised states (Simple Turing-type models) in the cell. Such a system that describes a switch between two states is described as a bistable system, which requires positive feedback; however, there is no direct method to test this hypothesis in live cells and thus, the goals of this project are two-fold:

1. To develop a fully controllable and quantifiable heterologous system that can be used to investigate membrane dynamics. A prerequisite to constructing the system is that the system must not interfere with endogenous cellular processes as this increases the complexity involved in the study. For this reason, this study exploits the absence of a specific phosphatidylinositol in the membranes of *S. cerevisiae* cells.
2. To use the constructed system to test different plasma membrane dynamics in live cells. The minimal feedback loop would consist of two components that interact with each other to result in bistability and hysteresis across the population.

## Chapter 2

# Design of the synthetic system

### 2.1 Summary

This chapter describes the design of the synthetic system, which is based on the absence of PI(3,4,5)P<sub>3</sub> and the presence of its precursor, PI(4,5)P<sub>2</sub> at the plasma membrane of *S. cerevisiae* cells. Manipulating PI(3,4,5)P<sub>3</sub> levels can be a powerful tool to study membrane dynamics in live *S. cerevisiae* cells and can be achieved by introducing the expression of p110 $\alpha$  and PTEN expression into the cell. The catalytic subunit, p110 $\alpha$  is responsible for the conversion of PI(4,5)P<sub>2</sub> to PI(3,4,5)P<sub>3</sub> and its antagonist, PTEN, is known to dephosphorylate PI(3,4,5)P<sub>3</sub> to restore levels of PI(4,5)P<sub>2</sub>. The resulting system constitutes four parts that include:

1. **A component to control p110 $\alpha$  membrane bound activity:** made-up of a highly tuneable synthetic promoter, the GEV system, and different versions of p110 $\alpha$ . The different versions of p110 $\alpha$  include a cytosolic version (p110 $\alpha_C$ ), a positive feedback loop version (p110 $\alpha_L$ ) and a membrane bound version (p110 $\alpha_M$ ). The positive feedback loop version binds to the membrane in the presence of PI(3,4,5)P<sub>3</sub> to produce more PI(3,4,5)P<sub>3</sub>.
2. **A component to control PTEN membrane bound activity:** made-up of a different highly tuneable synthetic promoter, TET-ON system and different versions of PTEN. The different versions of PTEN include a cytosolic version (PTEN<sub>C</sub>), a positive feedback loop version (PTEN<sub>L</sub>) and a membrane bound

version ( $PTEN_M$ ). The positive feedback loop version binds to the membrane in the presence of  $PI(4,5)P_2$  to produce more  $PI(4,5)P_2$ .

3. **A dual-reporter system that shows observable differences between  $PI(4,5)P_2$  and  $PI(3,4,5)P_3$  at the plasma membrane:** as GFP and mCherry show different fluorescence excitation and emission properties, they were used to observe levels of  $PI(3,4,5)P_3$  and  $PI(4,5)P_2$  at the plasma membrane, respectively.
4. **A machine-learning based algorithm:** to improve quantification, a machine-learning based algorithm was developed to quantify the levels of  $PI(4,5)P_2$  and  $PI(3,4,5)P_3$  as a result of different plasma membrane dynamics associated with the different versions of p110 $\alpha$  and PTEN.

## 2.2 Introduction to phosphatidylinositols

Phosphatidylinositols are a type of glycerophospholipids that make up the lipid bilayer of cell membranes. In general, glycerophospholipids contain a hydrophobic region and a hydrophilic region. The hydrophobic region is made up of a glycerol-3-phosphate molecule, which is esterified to an unsaturated acyl chain at  $C_1$  and a saturated acyl chain at  $C_2$ . The propensity of the hydrophobic moieties to self-associate (entropically driven by water) and the hydrophilic moieties to interact with aqueous environments is the basis of spontaneous formation of membranes. Spontaneous membrane formation is the fundamental principle that separates the internal components of the cell from its environment and allows for compartmentalisation of these internal components to form cellular organelles. The hydrophilic region is made up of a stereoisomer of *D-myo*-inositol, which is attached to the  $C_3$  position of the glycerol-3-phosphate by a phosphodiester linkage. The inositol moiety can be phosphorylated at D3, D4 or D5 positions (as shown in Figure 2.1), resulting in seven derivatives of phosphatidylinositol that are found in cellular membranes.

All seven types of phosphatidylinositol phosphate derivatives have been detected in mammalian cell membranes meanwhile, only four types are present in the mem-

## Structure of Phosphatidylinositol molecule

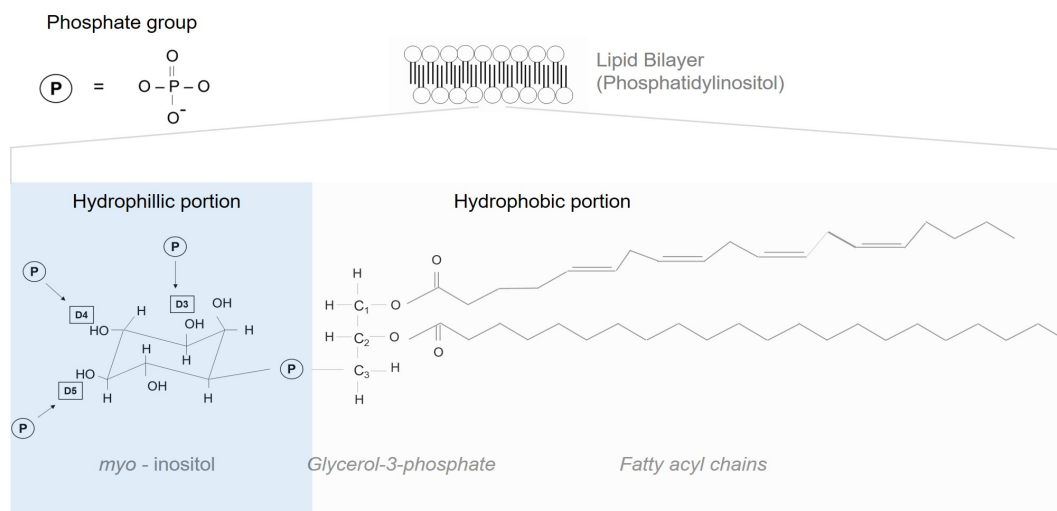


Figure 2.1: Structure of a phosphatidylinositol molecule. The amphipathic molecule is made up of a hydrophilic portion (blue) and a hydrophobic portion. The hydrophilic portion is made up of a *myo*-inositol moiety that can be phosphorylated in three positions, which gives rise to seven biologically important Phosphatidylinositol phosphates.

branes of *S. cerevisiae*. Individual phosphatidylinositol phosphate derivatives are found to provide specific functional and membrane identity to different cellular membranes in the cell. For example, PI(3,5)P<sub>2</sub>, which was the most recently discovered PIP is associated with vacuolar/ lysosomal membranes whereas, PI(4)P a more well established phosphatidylinositol phosphate has been found to be associated with several membranes involved with the endovesicular transport system [23, 33]. Mammalian cells have been found to contain all of the seven derivatives of phosphatidylinositol phosphates whereas, only four types (PI(3)P, P(4)P, PI(3,5)P<sub>2</sub> and PI(4,5)P<sub>2</sub>) are detected in the *S. cerevisiae* cellular membranes. A brief review of the current understanding of phosphatidylinositol metabolism in *Saccharomyces cerevisiae* can be found in Appendix A as the aim of this chapter is to provide an overview of the design of the synthetic system, based on the absence of PI(3,4,5)P<sub>2</sub> in the cellular membranes. PI(3,4,5)P<sub>3</sub> is produced by Class I phosphatidylinositol-3-kinases (PI3Ks) and the introduction of Class-I PI3Ks into *S. cerevisiae* is reviewed below.

## 2.3 Literature survey of heterologous expression of PI3K in *S. cerevisiae*

A literature survey was performed to determine the design for the expression of Class I PI3K in the *S. cerevisiae*. There are three classes of PI3Ks and *S. cerevisiae* cells do not possess genes encoding for Class I or Class II PI3Ks [101]. The introduction of Class I PI3Ks is thought to have no known effect on its own however, the rapid depletion of PI(4,5)P<sub>2</sub> is associated with activation of the cell wall integrity pathway, which results in G2 cell-cycle arrest [78, 2, 67]. Therefore, it is reasonable to assume that the introduction of Class I PI3K subunits in *S. cerevisiae* must take into account some design considerations to reduce toxicity.

Several studies have reported toxicity after induction of high expression levels of different subunits of Class-I PI3Ks. Class-I PI3Ks are heterodimers, constituting a catalytic sub-unit (p110 $\alpha$ / $\beta$ / $\gamma$ / $\delta$ ) and a regulatory subunit (p50-55/85/101) [55]. The severity of growth defects observed is dependent on the subunit, the expression level and plasma membrane association in the cell (Table 2.1).

### 2.3.1 Toxicity observed using p110 $\alpha$ was greater than using p110 $\beta$ subunit

The Class I PI3K subunits, p110 $\alpha$  and p110 $\beta$  have both been introduced to yeast cells (Table 2.1). From table 2.1, studies show that compared to the inactive p110 $\alpha$  mutant, the active p110 $\alpha$  subunit resulted in complete growth inhibition at high expression levels [83, 24, 67]. Table 2.1 also shows that a few studies compare the activities of membrane targetted p110 $\alpha$  and p110 $\beta$  [54, 1, 83, 75]. In these studies, induction of p110 $\beta$  expression was found to be associated with a slight decrease in growth compared to wild type cells. The  $K_M$  and  $V_{MAX}$ - values of p110 $\alpha$  for PI(4,5)P<sub>2</sub> are 25-fold higher than the values for p110 $\beta$  [6]. At high levels of PI(4,5)P<sub>2</sub>, modelling kinetic data showed that the  $V_{MAX}$  for p110 $\alpha$  activity is higher than p110 $\beta$  activity, suggesting that p110 $\alpha$  is more active in regions of the membrane where there is a higher concentration of PIP<sub>2</sub> [6]. The  $K_M$  value, describes the concentration of the substrate at half of the rate at maximal enzymatic activity

( $V_{MAX}$ ). Therefore, p110 $\alpha$  is more toxic than p110 $\beta$  as it depletes PI(4,5)P<sub>2</sub> more rapidly at the plasma membrane of *S. cerevisiae* cells.

### 2.3.2 High expression levels of p110 $\alpha$ showed more toxicity than low expression levels

The studies summarised in Table 2.1 show that thus far, expression of p110 $\alpha$  has been controlled using high copy number autonomously replicating, where the expression was driven using a weak constitutive promoter ( $P_{-CYC1}$ ) or a strong inducible promoter ( $P_{-GAL1}$ ). Studies that used the weak constitutive promoter to control p110 $\alpha$  expression did not report effects of cellular toxicity [17]. On the other hand, all other studies report severe cellular toxicity when the expression of p110 $\alpha$  was induced with 2% galactose, using high copy number plasmids ( $2\mu$  plasmids).

### 2.3.3 Membrane bound of p110 $\alpha$ was associated with more toxicity than cytosolic constructs

Some studies have compared the toxicity of membrane association of p110 $\alpha$  [84]. Membrane targeted versions (p110 $\alpha$ -CAAX) was associated with no cell growth compared to the cytosolic version, p110 $\alpha$  in *S. cerevisiae*. Expression of both the p110 $\alpha$  and p110 $\alpha$ -CAAX were driven by fully inducing  $P_{-GAL1}$  promoter. In comparison, the cytosolic form (p110 $\alpha$ ) showed reduced growth that was slower than cells that expressed the inactive mutant [84]. These studies suggest that membrane association i.e., the increased proximity to PI(4,5)P<sub>2</sub> increased the severity of the toxic effects of the p110 $\alpha$  in *S. cerevisiae*.

### 2.3.4 Design considerations of p110 $\alpha$ expression in *S. cerevisiae*

1. To overcome the effects of severe toxicity due to the rapid depletion of PI(4,5)P<sub>2</sub> at the plasma membrane, the p110 $\alpha$  constructs used in this study were integrated to the genome. Genomic integration into *S. cerevisiae* cells allows more rational design as copy number can be quantified and controlled. Integration at the genome most frequently occurs as a single copy but occasionally produces high copy number strains. Even at high copy number integration, the plasmid

load on the cell is much lower than that observed using  $2\mu$  plasmids, which can result in  $\approx 20$ - 60 copies per cell. Integration to the genome also allows more stability as plasmids will not be degraded with age in the cell.

2. Toxicity of constructs could further be controlled using the tuneable GEV inducible promoter system, which offers a high level of control over expression levels in the cell using  $\beta$ -estradiol. The tuneable control of the promoter system allows to determine viable conditions in the cell using different concentrations of  $\beta$ -estradiol [66]. The response that is typically observed using this system results in a sigmoidal dose-response curve that saturates at concentrations  $>30$  nM of  $\beta$ - estradiol induction [66].

Table 2.1: Literature survey of studies that introduce p110 $\alpha$  catalytic domain to *S. cerevisiae* cells.

Expression system	PI3K Construct	Toxicity Observed	Effect on Cells	Ref.
<i>GAL1</i> inducible promoter	110 $\beta$ -CAAX	No Toxicity observed	Targets Of PI3K Identification System expression system was made to rescue CDC25 temperature sensitive mutants in a PI(3,4,5)P <sub>3</sub> dependent manner.	[54]
<i>GAL1</i> inducible promoter	110 $\alpha$ -CAAX (active) and p110 $\alpha^{K802R}$ -CAAX (inactive mutant)	Toxicity observed as growth defects in cells expressing active catalytic domain and not in inactive mutant, which did not produced PIP <sub>3</sub> on the membrane.	Toxicity was associated with the depletion of PI(4,5)P <sub>2</sub> pools on the membrane, resulting in altered actin cytoskeleton disruption. Actin and Septin cytoskeleton disruption was studied using a rhodamine-conjugated phalloidin stain. Levels of PI(4,5)P <sub>2</sub> was observed using GFP-2XPH(PLC $\delta$ ). TepIp, a yeast PTEN homologue did not rescue cell viability.	[84]
<i>GAL1</i> inducible promoter	p110 $\alpha$ , p110 $\beta$ , p110 $\alpha$ -CAAX, p110 $\beta$ -CAAX, p110 $\alpha^{E545K}$ , p110 $\alpha^{H1047R}$	Toxicity observed in p110 $\alpha^{E545K}$ > p110 $\alpha$ -CAAX > p110 $\alpha$ $\approx$ p110 $\alpha^{H1047R}$ > p110 $\beta$ -CAAX > p110 $\beta$ due to increasing levels of PI(3,4,5)P <sub>3</sub> on the plasma membrane. p110 $\alpha^{E545K}$ and p110 $\alpha^{H1047R}$ are mutants that are commonly associated with human cancers.	Increasing levels of PI(3,4,5)P <sub>3</sub> were observed using Akt1-GFP fusion protein. Cell viability tests showed that p110 $\alpha^{E545K}$ and p110 $\alpha^{H1047R}$ were the most toxic to the cell. Co-expression of PTEN alleviated toxicity and the minimum length of truncated PTEN was found to be 1-350 aa.	[1]

Table 2.2: Literature survey of studies that introduce p110 $\alpha$  catalytic domain to *S. cerevisiae* cells (*Continued*).

Expression system	PI3K Construct	Toxicity Observed	Effect on Cells	Ref.
<i>GAL1</i> inducible promoter	p110 $\alpha$ -CAAX (active) and p110 $\alpha^{K802R}$ -CAAX (inactive mutant)	Two-fold decrease in growth rate was observed in cells expressing p110 $\alpha$ -CAAX, compared to cells expressing p110 $\alpha^{K802R}$ -CAAX. Toxicity associated with kinase activity resulting in depletion of PI(4,5)P <sub>2</sub> levels.	PI(4,5)P <sub>2</sub> depletion was observed using GFP-2XPH(PLC $\delta$ ). Fatty acid components derived from fish oil prevented PI(4,5)P <sub>2</sub> depletion due to direct inhibition of kinase activity.	[24]
<i>GAL1</i> inducible promoter	p110 $\alpha$ , p110 $\beta$ , p110 $\alpha$ -CAAX, p110 $\beta$ -CAAX, p110 $\alpha^{E545K}$ , p110 $\alpha^{H1047R}$ , p110 $\alpha$ -CAAX-Akt, myr-Akt-p110 $\alpha$ , Akt1 <sup>K179M</sup> -p110 $\alpha$	Toxicity was observed.	No growth was observed in cells expressing p110 $\alpha$ -CAAX. Akt constructs showed growth defects when PH(AKT) was present. Co-expression of PTEN but not SHIP1 (a PI(3,4,5)P <sub>3</sub> 5-phosphatase) rescued cell toxicity.	[83]
<i>CYC1</i> constitutive promoter	p110 $\alpha$ -CAAX, p110 $\alpha$ -PH(AKT)	No toxicity was observed.	Minimal circuit to study polarisation after treatment with 5 $\mu$ M Latrunculin. Poles were observed.	[17]
<i>GAL1</i> inducible promoter	p110 $\alpha$	Toxicity was observed with co-expression of Akt1, which resulted in large and ubiquitous plasma membrane invaginations.	Growth defects were observed using cell viability assays after Galactose induction. Plasma membrane invaginations were observed using microscopy.	[82]

Table 2.3: Literature survey of studies that introduce p110 $\alpha$  catalytic domain to *S. cerevisiae* cells (Continued).

Expression system	Pl3K Construct	Toxicity Observed	Effect on Cells	Ref.
<i>GAL1</i> inducible promoter	p110 $\alpha$ -CAAX (active) and p110 $\alpha^{K802R}$ -CAAX (inactive mutant)	Growth inhibition was observed in cells expressing active p110 $\alpha$ -CAAX.	<i>Rsc1<math>\Delta</math></i> , <i>Rom2<math>\Delta</math></i> and <i>bck1<math>\Delta</math></i> , mutants involved in cell wall integrity pathway did not show toxicity after induction of p110 $\alpha$ -CAAX expression.	[35]
<i>GAL1</i> inducible promoter	p110 $\alpha$ -CAAX and p110 $\alpha$ -CAAX-Akt	Toxicity was observed.	Growth curves and halo assays were performed to measure kinase inhibition of 1,4-mopholino-2-phenylquinazolines. No growth was observed in cells expressing p110 $\alpha$ -CAAX. Akt constructs showed growth defects when PH(AKT) was present.	[34]
<i>GAL1</i> inducible promoter	p110 $\alpha$ -CAAX	Growth inhibition in cells expressing p110 $\alpha$ -CAAX.	Cell viability tests were performed on induced cells. PTEN mutants were found to rescue depletion of PI(4,5)P <sub>2</sub> . Activity of PTEN mutants was observed using FACS.	[85]

Table 2.4: Literature Survey of studies that introduce p110 $\alpha$  catalytic domain to *S. cerevisiae* cells (Continued).

Expression system	PI3K Construct	Toxicity Observed	Effect on Cells	Ref.
<i>GAL1</i> inducible promoter	All PI3K- Class I constructs.	Toxicity was observed in cells expressing p110 $\alpha$ subunit.	Fusion proteins containing different combinations of the catalytic and regulatory subunits were introduced to the cell. Cell viability assays showed that p110 $\alpha$ subunit was the most toxic but toxicity was decreased when regulatory subunit p85 was also present.	[75]
<i>GAL1</i> inducible promoter	p110 $\alpha$ -CAAX	Toxicity was observed as growth inhibition in cells that expressed p110 $\alpha$ -CAAX.	No growth was in cells expressing p110 $\alpha$ -CAAX. Cells were used to test test activity of PTEN genetic variants.	[67]
<i>GAL1</i> inducible promoter	p110 $\alpha$	Toxicity was observed with co-expression of Akt1, which resulted in large and ubiquitous plasma membrane invaginations.	Growth defects were observed using cell viability assays after Galactose induction. Plasma membrane invaginations were observed using microscopy.	[82]
<i>GAL1</i> inducible promoter	p110 $\alpha$ -CAAX	Toxicity was observed as growth inhibition in cells that expressed p110 $\alpha$ -CAAX.	No growth was in cells expressing p110 $\alpha$ -CAAX. Cells were used to test test activity of PTEN genetic variants.	[67]

## 2.4 Components of the system

### 2.4.1 Controlling p110 $\alpha$ dynamics at the plasma membrane

As mentioned in the previous section, the kinase domain of Class I PI3Ks, p110 $\alpha$  can be expressed in *S. cerevisiae* cells without interfering with endogenous cell processes. Moreover, as toxicity is a concentration dependent phenomena, we can reduce the amount of toxicity by taking into consideration copy number, expression level and membrane association. This allows for a system that can be constructed to understand membrane dynamics based on the manipulation of PI(3,4,5)P<sub>3</sub> levels at the plasma membrane. To observe different membrane dynamics, the three versions of p110 $\alpha$  (p110 $\alpha_C$ , p110 $\alpha_L$  and p110 $\alpha_M$ ) were constructed to have different membrane binding activities by fusing different localisation domains to the catalytic subunit (Figure 2.10). The three constructs were integrated to the genome to reduce plasmid load on the cell and expression was driven using a highly tuneable synthetic promoter known as the GEV system.

The GEV system is commonly used in synthetic biology as it allows for highly tuneable gene expression using  $\beta$ -estradiol [66]. It is made up of a fusion protein containing the DNA binding domain of Gal4 (Gal4dbd), along with the human  $\beta$ -estradiol receptor binding domain (ER) and the C-terminus of the herpes simplex virus (VP16). The GEV protein is constitutively expressed in the cell and accumulates in the cytosol where it associates with the Hsp90 chaperon complex. In the presence of  $\beta$ -estradiol, the hormone diffuses through the cell and binds to the estradiol receptor, releasing the protein from the chaperone complex. The  $\beta$ -estradiol bound GEV localises to the nucleus where it binds to the *GAL1*UAS and strongly activates transcription of recombinant gene through the VP16 domain. VP16 is an 18 residue, highly acidic and especially powerful activation domain. Gal4dbd-VP16 is thought to induce a conformational change in TFIIB, which facilitates binding of TFIIF and DNA polymerase II. In the absence of TFIIB, N-terminal docking site for TFIIF and C-terminal docking site for DNA polymerase II are obscured. Binding of Gal4dbd-VPS16 results in conformational change and binding to DNA polymerase II. In this manner, the GEV system provides a fast-acting and dose dependent induction

of the gene of interest [66].

### 2.4.2 Controlling PTEN dynamics at the plasma membrane

The different versions of PTEN ( $PTEN_C$ ,  $PTEN_L$  and  $PTEN_M$ ) were also integrated into the genome of *S. cerevisiae* cells (Figure 2.10). In all the PTEN versions, the mutation (K13E) was introduced to PTEN to disrupt its natural membrane associative properties at the N-terminus of the catalytic domain (Figure 2.2). The C2 domain in PTEN is known to bind to  $PI(4,5)P_2$ , producing a positive feedback loop [49]. The membrane binding property that results in the allosteric activation of the enzyme would affect the general design of the system constructed in this study. The mutations K13A and K14A in the C2 region are known to significantly affect PTEN  $PI(4,5)P_2$  binding through the C2 domain in the cell [14]. For this reason, the K13E mutation was introduced in the C2 module of the PTEN protein. The missense mutation is commonly associated with hereditary cancers such as Endometrial cancer, Cowden syndrome and Glioblastomas [42]. Glutamic acid (E) is a negatively charged polar amino acid and when substituted for lysine (K), a positively charged polar amino acid the protein can no longer associate with  $PI(4,5)P_2$  at the plasma membrane and this mutation results in virtually no  $PI(3,4,5)P_3$  dephosphorylation *in vivo* [42]. The PTEN sequence used in this study contains a K13E mutation and for convenience, PTEN is always used to refer to the mutant as this study does not test wildtype PTEN.

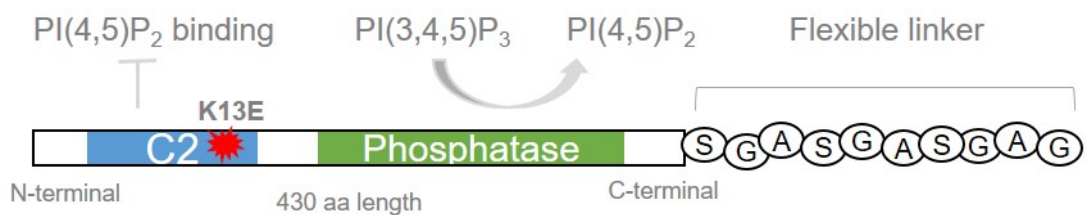


Figure 2.2: Schematic diagram of PTEN mutant cytosolic construct ( $PTEN_C$ ). The K13E mutation was introduced to the C2 domain in the PTEN sequence to disrupt  $PI(4,5)P_2$  binding ability. The cytosolic construct was fused to a linker at the C-terminus. The linker was fused to the membrane localisation domains to make the membrane binding constructs.

Expression of PTEN was controlled using the TET-ON doxycycline inducible sys-

tem as it allowed independent control over expression that is different to galactose inducible systems. The TET-ON system is tightly controlled and results in either low or high levels of expression of the gene of interest [51]. It is made up of the tetracycline response element (TRE) and a fusion protein reverse- tetracycline controlled transactivator protein (rtTA). The TRE is made up of a a minimal promoter sequence ( $P_{CLN3}$ ) and a concatamer of the minimal tet operator (*tetO*) sequence, which is a seven repeats of 19 nucleotide (TCCCTATCAGTGATAGAGA) [51]. In the presence of doxycycline, the operator sequence is recognised by the fusion protein rtTA. The rtTA protein comprises of a mutated tet- repressor (tetR) protein fused to a VP16 transactivator domain.

### 2.4.3 Dual reporter system to observe membrane dynamics

As PH domains can bind to specific phosphatidylinositol phosphates, PH(AKT) and 2XPH(PLC $\delta$ ) were also used to observe the levels of PI(3,4,5)P<sub>3</sub> and PI(4,5)P<sub>2</sub>, respectively (Figure 2.10). Fluorescent proteins are commonly used in cell localisation studies as they can be easily manipulated and conveniently detected using fluorescence microscopy. There are a wide range of fluorescent proteins commonly used in live cell imaging. The excitation and emission peaks of GFP and mCherry do not overlap therefore, making them a good choice for observing the levels of PI(4,5)P<sub>2</sub> and PI(3,4,5)P<sub>3</sub>, respectively.

The entire structure of fluorescent proteins are essential for the development and maintenance of fluorescence. Their 25KDa structure consists of an extremely rigid  $\beta$ -barrel-fold comprising of 11  $\beta$ -sheets that surround a central  $\alpha$ -helix [27]. The fluorescence property comes from a unique environment found around a few crucial amino acids (S65, Y66 and G67) found on the  $\alpha$  helix, which is located near the centre of the  $\beta$ -barrel. These polar amino acids bind to a number of water molecules that lock these crucial amino acids into an imidazole ring with extended conjugation, allowing for chromophore formation. The unique environment surrounding the chromophore is maintained by a rigid  $\beta$ -barrel structure that consists of polar molecules that trap water molecules. The conserved residues are found on an  $\alpha$ -helix that is present inside the  $\beta$ -barrel. In this environment, S65 undergoes nucleophilic attack

by G67, followed by a cyclization step and auto-oxidation of Y66. These processes result in the formation of 4-(p-hydroxybenzylidene)-imidazolidin-5-one, which contains a large  $\pi$ -conjugated system and results in green fluorescence after excitation with light at 470nm. Changing the S65  $\rightarrow$  H65, results in (5-imidazolyl)ethenyl group, the chromophore for red fluorescent proteins, namely mCherry that can be excited at 520nm.

By fusing the 2XPH(PLC $\delta$ ) domain to GFP and the PH(AKT) domain to mCherry, the dual reporter system is a sensitive tool that can be used to observe the levels of PI(4,5)P<sub>2</sub> and PI(3,4,5)P<sub>3</sub>, respectively. To quantify the relative amounts of GFP and mCherry on the plasma membrane of the cell, a machine-learning based algorithm was developed based on the dual-reporter system.

#### 2.4.4 Theory of the dual-reporter system

The relative amounts of PI(3,4,5)P<sub>3</sub> levels at the plasma membrane can be quantified as the ratio of mCherry at the plasma membrane to the cytosol. Let, mCh<sub>c</sub> and mCh<sub>M</sub> represent cytosolic and membrane bound mCherry, respectively, such that:



where,

$$[PIP_3] = \frac{1}{K_1} \frac{[mCh_M]}{[mCh_c]} \quad (2.1)$$

From Equation 2.1, the simplest method to determine relative amount of PI(3,4,5)P<sub>3</sub> at the plasma membrane could be determined by the ratio between the mCherry bound plasma membrane signal and cytosolic signal, where K<sub>1</sub> represents the equilibrium constant of the reaction. However, using this method alone presents problems that affect automating quantification.

The image that is acquired using a wide-field epifluorescence microscope is a reflected image of a three dimensional spherical cell. As the size of *S. cerevisiae* range from 4- 10 nm in diameter and they are unicellular organisms, illumination of the entire sample without interference from background fluorescence is possible using

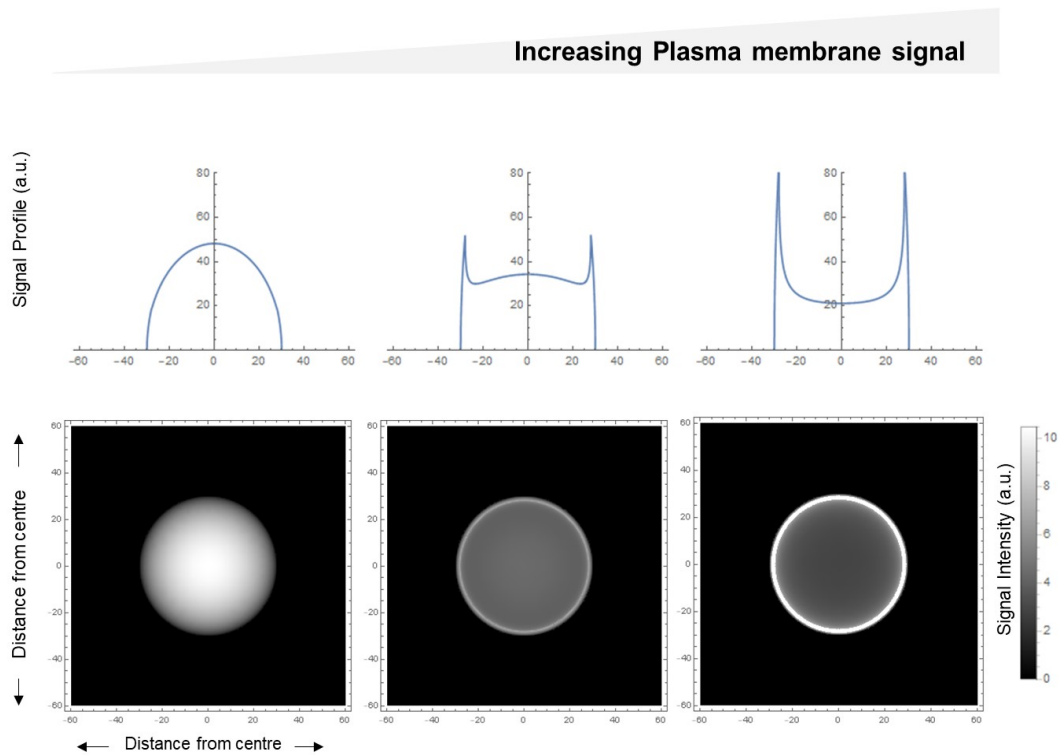


Figure 2.3: Geometric model showing changes in cell shape due to increasing plasma membrane signal.

a wide-field microscope. Additionally, compared to other microscope techniques the wide-field microscope allows better illumination of the sample, which is advantageous in small samples such as yeast cells. The image acquired results in the reflection of a three-dimensional spherical cell onto a two-dimensional fluorescence sensor, which does not accurately record the cell shape (Figure 2.3).

Geometric modelling of fluorescence behaviour at the plasma membrane showed changes in cell shape, as a result of localisation of fluorescence signal in the cell. A simple geometric model based on the Equation 2.1, showed that cell shape changes with different amounts of fluorescence at the plasma membrane (Figure 2.3). At low levels of fluorescence at the plasma membrane would result in a smaller than the actual cell to be identified, which would result in differences compared to cells with high fluorescence at the plasma membrane. Taking data from both the GFP and mCherry channel can correct for these changes in cell shape, that are found at different levels of fluorescence at the plasma membrane of the cell.

Taking data from both channels also results in a convenient way of measuring

relative changes of PI(3,4,5)P<sub>2</sub> and PI(4,5)P<sub>3</sub> at the plasma membrane of the cell. Let, GFP<sub>c</sub> and GFP<sub>M</sub> represent cytosolic and membrane bound GFP, respectively, such that:

$$\text{GFP}_c + \text{PIP}_2 \rightleftharpoons \text{GFP}_M$$

where,

$$[\text{PIP}_2] = \frac{1}{K_2} \frac{[\text{GFP}_M]}{[\text{GFP}_c]} \quad (2.2)$$

and K<sub>2</sub> represents the equilibrium constant of the reaction.

By dividing Equation 2.1 by 2.2, we can get the relative amounts of mCh<sub>M</sub> to GFP<sub>M</sub>:

$$\frac{[\text{PIP}_3]}{[\text{PIP}_2]} = \frac{K_2}{K_1} \frac{\frac{[\text{mCh}_M]}{[\text{mCh}_c]}}{\frac{[\text{GFP}_M]}{[\text{GFP}_c]}} \quad (2.3)$$

Let,  $\frac{K_2}{K_1}$  be some constant  $C$ , then

$$\frac{[\text{PIP}_3]}{[\text{PIP}_2]} = C \frac{\frac{[\text{mCh}_M]}{[\text{mCh}_c]}}{\frac{[\text{GFP}_M]}{[\text{GFP}_c]}} \quad (2.4)$$

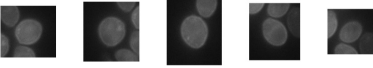
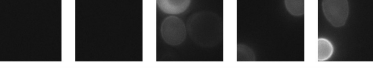
From Equation 2.4, the relative amount of PI(3,4,5)P<sub>3</sub> to PI(4,5)P<sub>2</sub> is proportional to the ratio of ratios of the plasma membrane to cytosol signal across both mCherry and GFP channels. Here, we define the  $PIP_3$ -Index as the Log<sub>2</sub> value of  $\frac{[\text{PIP}_3]}{[\text{PIP}_2]}$ . Taking the Log<sub>2</sub> of Equation 2.4,

$$'PIP_3 - Index' = \text{Log}_2 C + \text{Log}_2 \left( \frac{\frac{[\text{mCh}_M]}{[\text{mCh}_c]}}{\frac{[\text{GFP}_M]}{[\text{GFP}_c]}} \right) \quad (2.5)$$

### 2.4.5 Machine-learning based quantification method

The workflow developed for quantification of the  $PIP_3$ -Index included collecting images of cells across mCherry and GFP channels, machine-learning based identification of cells in each channel, determining average fluorescence profile in each cell and calculating  $PIP_3$ -Index (Figure 2.5). Image segmentation refers to the process by which objects can be identified in an image and in this study we retrain an existing model to increase quantification throughput and reduce user defined bias. To retrain Tensor-

flow Mobilenet v2 model, images of cells collected using fluorescence microscopy were used. In total, 5000 cells were manually identified using ImageJ package and used as training data. These cells were classified as: "good", "bad" or "not cell" (Figure 2.6). Bad cells included cells that were near other cells i.e., less than a few pixels away from each other. The bad cells classifier was defined to simplify the re-training of the machine learning algorithm and allow for faster processing times as there would be less ambiguity in cell identification. Using an automated method for image segmentation increased the number of images that were processed and analysed. Next, cell boundaries were identified in segmented regions and signal profiles for each cell was produced across mCherry and GFP channel (Figure 2.7 and 2.8). The average fluorescence profile was determined from these signal profiles for each channel and the ratio of plot profiles were determined (Figure 2.9). These profiles were used to determine the  $PIP_3$ -Index as the ratio between the average plasma membrane signal to cytosolic signal of the ratio profile from both channels. All scripts that were developed to quantify the  $PIP_3$ -Index for each cell are provided in Appendix B.

Class	Examples	Total images
Good		303
Bad		367
Not cell		2295

Training data set 6

Figure 2.4: Training data used to retrain Mobilenet v2 model. Cells were manually identified using ImageJ package and classified into three classifiers as shown here. In total, 5000 cells were used to train the model to identify cells for quantification.

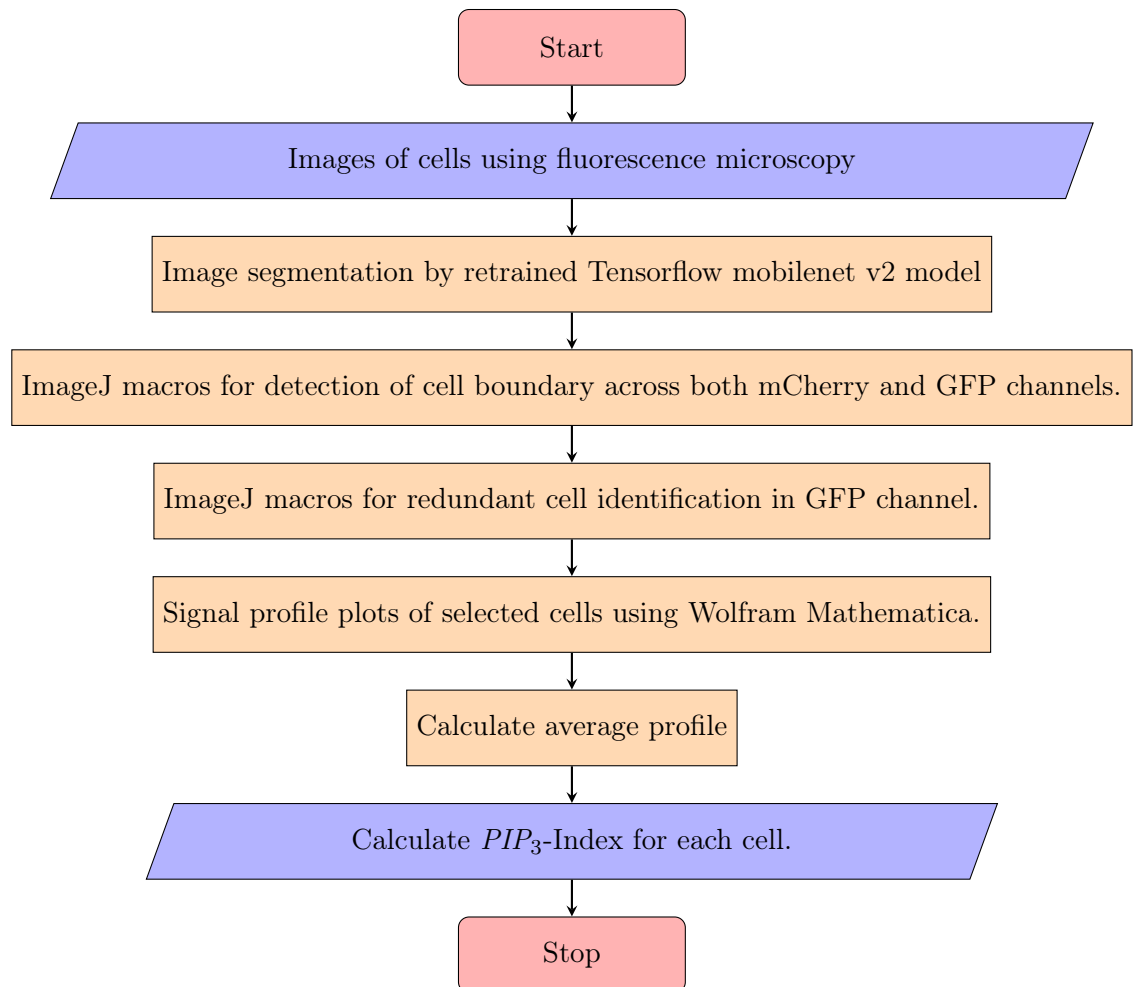
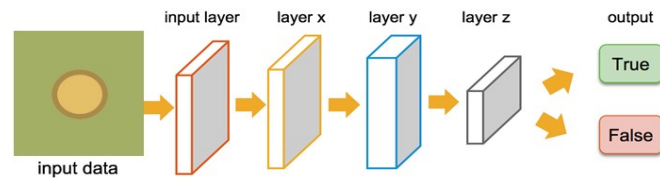


Figure 2.5: Machine-learning based quantification workflow.

## Tensorflow Mobilenetv2 model



## Process layers

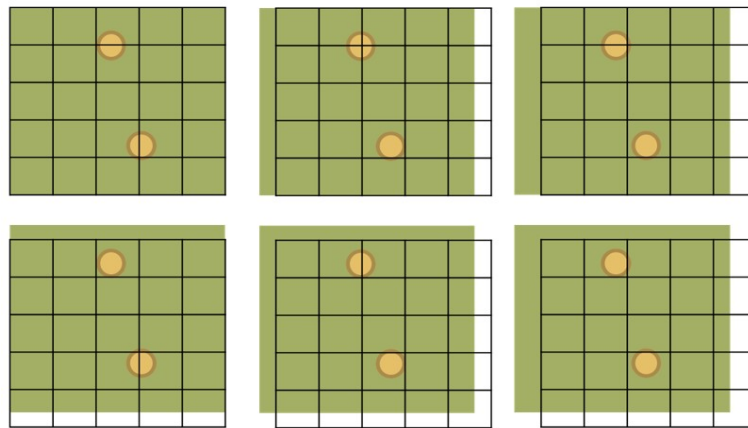
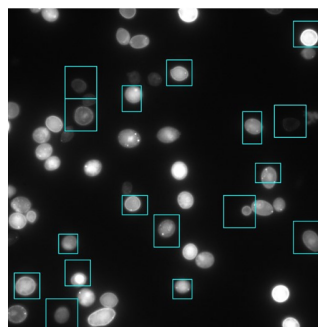


Figure 2.6: Illustration of application of Tensorflow Mobilenet v2 model for image segmentation. Top panel shows the overview of Mobilenet v2 architecture, which is made up of several convolution layers to result in image segmentation. The process layer panel shows that the input image is segmented the ways that the image is segmented to identify cells for quantification.

## Detection of Good cells



## Cell boundary Identification

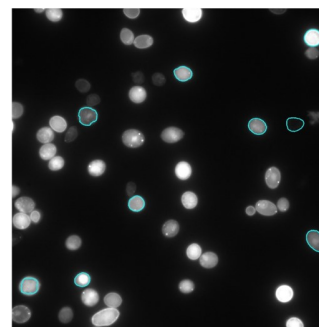


Figure 2.7: Identification of cell boundary in segmented regions. The segmented images result in the several squares that have been identified, the training model keeps the squares wherein "good" cells are detected. After cleaning up the image to produce only one square around each cell, the on the left is produced. Using ImageJ, the identification of cell boundaries was automated and the cells identified using this method are shown on the right hand side.

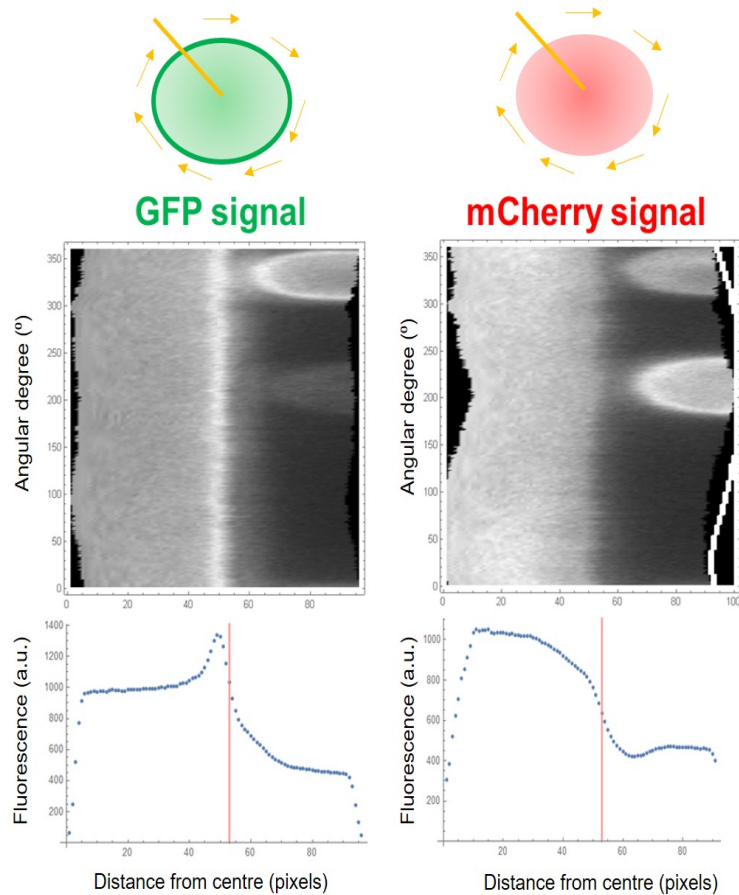


Figure 2.8: Example of of mCherry and GFP signal profile plots across a single cell with low  $\text{PI}(3,4,5)\text{P}_3$  levels. At the top, a schematic diagram of how the data for the signal profile plots were collected as a line-selection (yellow line) was drawn to measure the signal across all  $360^\circ$  of the cell (yellow arrows). Using this a plot was generated as shown in the middle panel. At low  $\text{PI}(3,4,5)\text{P}_3$ -levels, the GFP is present at the plasma membrane and mCherry is distributed across the cytosol and thus plotting the average signal profile results in a peak in the GFP plot and a trough in the mCherry plot that is present at the boundary of the cell (red line).

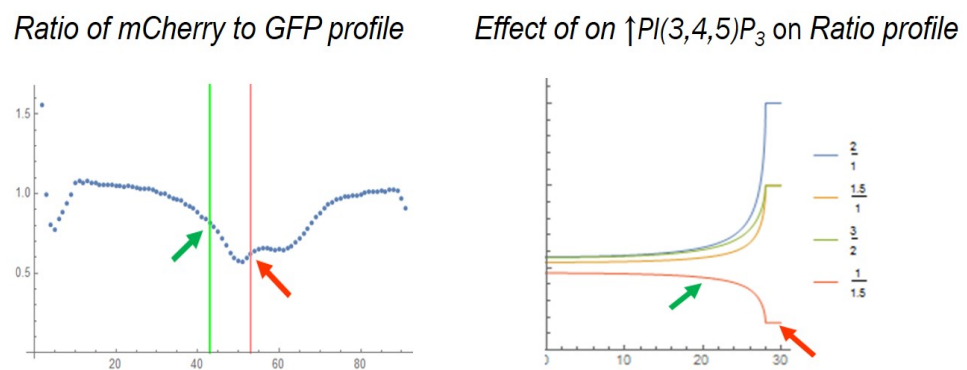


Figure 2.9: Actual and theoretical ratio plots between mCherry and GFP average profile plots. To calculate  $PIP_3$ -Index, the ratio of the average profile plots determined by the signal profiles were determined. The resulting profile plot shows a trough when GFP is present on the membrane (left). Increasing amounts of mCherry due to increased  $PI(3,4,5)P_3$  levels at the plasma membrane would result in a peak in the ratio plot as shown in the theoretical plots (right). The  $PIP_3$ -Index is determined by calculating ratio of the average signal at the plasma membrane (between the red and green lines) to the average signal in the cytosol (within the green line). The arrows indicate the effect of plasma membrane bound GFP and cytosolic mCherry in the ratio plot.



## Chapter 3

# Building the synthetic system in *S. cerevisiae*

### 3.1 Summary

In this chapter, the construction of the p110 $\alpha$  control, the dual reporter and the machine learning components that make up the system are described. The design considerations to make expression of p110 $\alpha$  less toxic in the cell showed that toxicity observed was greater in p110 $\alpha_L$  > p110 $\alpha_M$   $\approx$  p110 $\alpha_C$   $\approx$  control cells. The dual reporter system was optimised to show increased detection range so that plot profiles looked similar to the theoretical design to show bigger differences due to increased signal to noise in the image. The advantages offered by the dual reporter system were used to develop a machine-learning based algorithm, which was found to detect cells in both channels and quantification of the relative amounts of PI(3,4,5)P<sub>3</sub> at the plasma membrane.

### 3.2 Investigating p110 $\alpha$ toxicity using the GEV system

To determine the toxic effects of expressing the different versions of p110 $\alpha$  that were used in this study, the doubling time at different concentrations of  $\beta$ -estradiol was determined across all the constructs. The GEV system induces expression in the presence of  $\beta$ -estradiol and the level of expression in the cell is thought to be pro-

portional to the amount of  $\beta$ -estradiol available to the cell. All the p110 $\alpha$  versions (Control, p110 $\alpha_C$ , p110 $\alpha_L$  and p110 $\alpha_M$ ) were tested at concentration ranges between 0.12-250nM. No growth was observed at concentrations higher than 62.5nM of  $\beta$ -estradiol (Figure 3.1). Compared to the other constructs, the p110 $\alpha_L$  construct showed the most amount of toxicity between as 7.8nM and 62.5nM of  $\beta$ -estradiol treatment (Figure 3.1 and 3.2). To compare differences due to the effects of p110 $\alpha_L$  expression, a DMSO control was also used. The maximum difference was observed at 62.5nM  $\beta$ -estradiol treatment, where the difference between the DMSO control and p110 $\alpha_L$  expression was 20%. Less difference was observed at lower concentrations (Figure 3.2). Other constructs showed no differences between the DMSO control and the p110 $\alpha$  expression (Figure 3.3). To represent the relative doubling time at each concentration, the doubling time of p110 $\alpha$  expression was normalised to the DMSO control (Figure 3.1). A sharp increase in the relative doubling time was observed in the p110 $\alpha_L$  constructs at concentrations, higher than 7.5nM (Figure 3.3). To test if the differences between the p110 $\alpha_L$  and the other constructs were significant, a one-way ANOVA test was performed (p-value<0.05). The differences observed between p110 $\alpha_L$  and the other constructs were not significant.

In conclusion, a viable expression level of p110 $\alpha$  was determined using the GEV system. To achieve the maximum expression level of the p110 $\alpha$  constructs in the cell as well as to minimise possible toxicity, a concentration of 25nM  $\beta$ -estradiol was chosen to be used for further experiments in this thesis. In this study, I also show that viable expression of p110 $\alpha_M$  (or the p110 $\alpha$ -CAAX) construct was achieved using the GEV system. As discussed in Chapter 2, the expression of this construct has almost always resulted in reduced cell growth (Table 2.1). The relative doubling time of p110 $\alpha_M$  was found to be comparable to the control and the cytosolic, p110 $\alpha_C$  constructs.

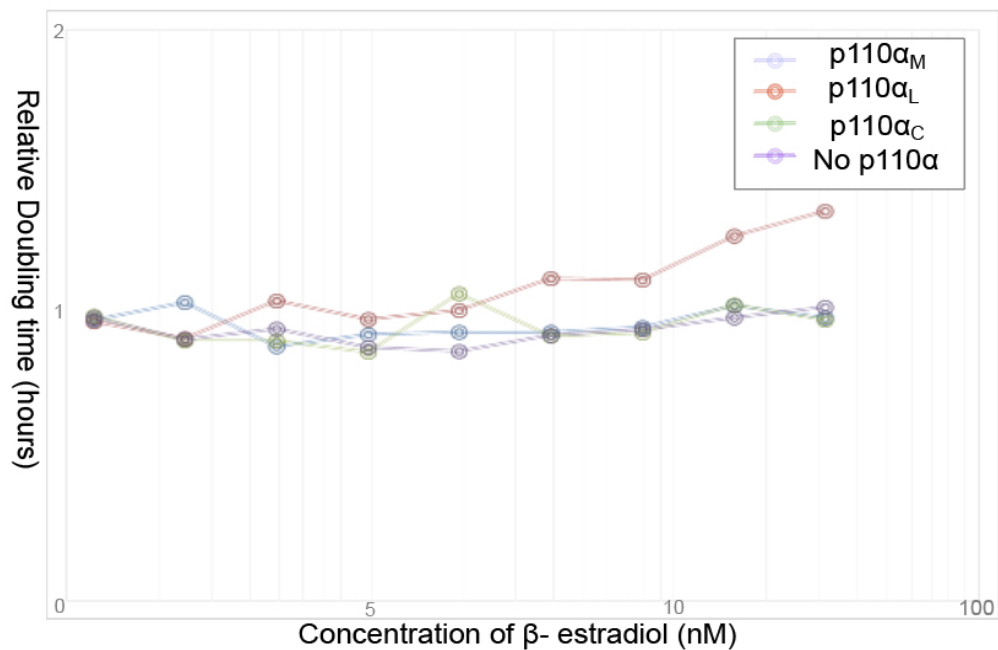


Figure 3.1: Effect of p110 $\alpha$  expression on relative doubling time of cells. The different versions of p110 $\alpha$  were induced using concentrations ranging from 0.12- 62.5nM of  $\beta$ - estradiol. The relative doubling time was determined by fitting the log-phase data to an exponential growth model and normalised to doubling time of the DMSO control. The values were determined from from three experimental repeats and the differences observed in the doubling times across all three constructs were not significantly different to the control. A one-way ANOVA test was performed to test statistical significance ( $p < 0.05$ ).

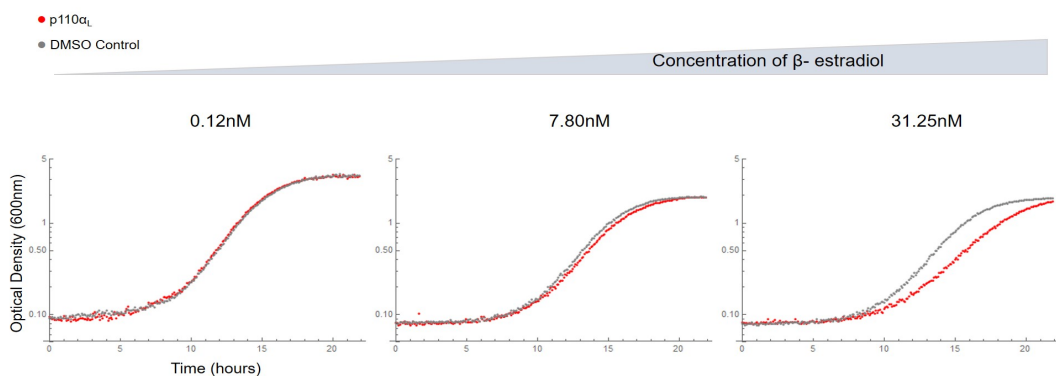


Figure 3.2: Effects of p110 $\alpha_L$  expression, compared to DMSO control. Representative growth curve data showing effects of p110 $\alpha_L$  expression induced at 0.12nM, 7.8nM and 31.25nM of  $\beta$ -estradiol treatment, compared to DMSO control.

### 3.3 Constructing a robust dual reporter system

To develop a tuneable system that could be easily manipulated for the purpose of studying membrane dynamics, it was essential to build a robust dual reporter system

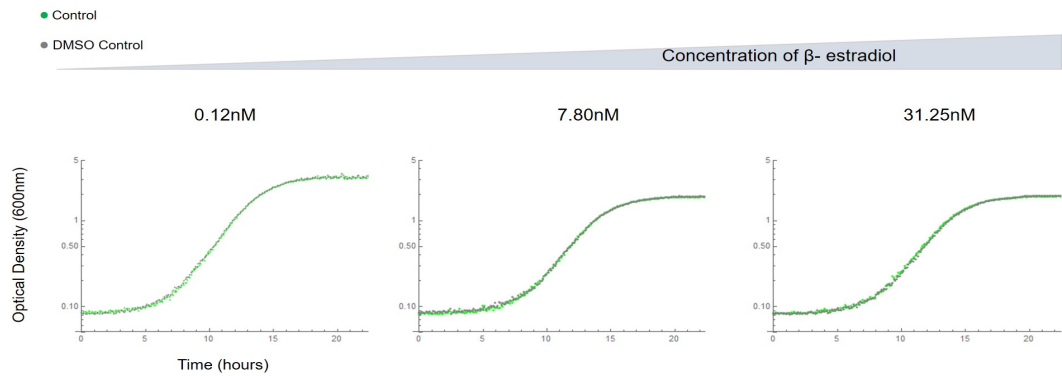


Figure 3.3: Effect of  $\beta$ -estradiol treatment on control cells. Representative growth curve data showing effects of no expression of p110 $\alpha$  in control cells treated with 0.12nM, 7.8nM and 31.25nM of  $\beta$ -estradiol, compared to DMSO control.

that could reliably reflect the changes of phosphatidylinositol phosphate levels at the plasma membrane of cells. As these molecules only constitute <1% of the entire dry weight of the cell, the ideal dual reporter system should show strong differences across small changes in the levels of phosphatidylinositol phosphates at the plasma membrane of the cell. The reporter constructs are made up of three parts: a strong constitutive promoter, a reporter protein and a PH domain. To detect PI(3,4,5)P<sub>3</sub> levels at the plasma membrane, mCherry was fused to PI(3,4,5)P<sub>3</sub> binding PH(AKT) and to detect PI(4,5)P<sub>2</sub>, GFP was fused to a tandem repeat of 2XPH(PLC $\delta$ ). To increase dynamic range of detection, the dual reporter system needs to be robust against two types of noise: background-to-signal noise and internal noise detected across the signal profile. By replacing or changing the orientation of the promoter, reporter and phosphatidylinositol phosphate binding domains, the dynamic range of detection by the dual reporter system was optimised for the purposes of this study.

### 3.3.1 Increased promoter strength resulted in increased detection range of PI(4,5)P<sub>2</sub> binding GFP reporter

*P*<sub>TEF1</sub> was selected after comparing fluorescence strength across four different constitutive promoters (Figure 3.4). The sequences of these promoters were obtained from the genomic DNA extracted from wildtype W303-A cells. Plasmids were constructed to express yEGFP and integrated into the genome of the yeast cells. Strains containing a single copy of each plasmid were selected and their fluorescence strength

was measured, using flow cytometry. A positive control was used to compare the strength of GFP, which controlled the GFP expression using the TET-ON system. The positive control showed 40 times more fluorescence than the weakest constitutive promoter,  $P\_CLN3$ .  $P\_TEF1$  was found to be the strongest constitutive promoter, which showed almost 4 times stronger fluorescence than  $P\_CLN3$  (Figure 3.4).

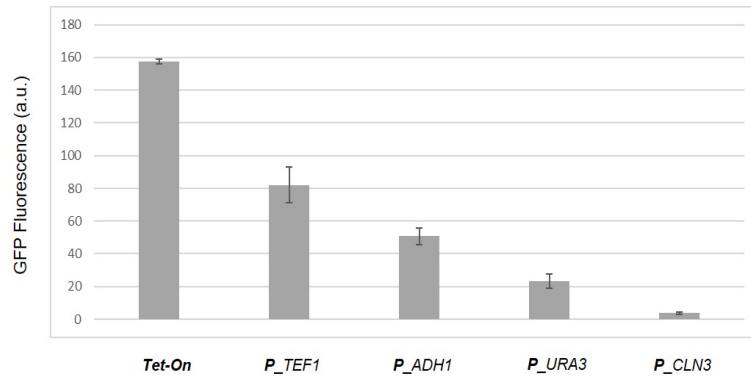


Figure 3.4: Comparing constitutive promoter strength. The mean GFP fluorescence of the constitutive promoters was measured across at least two trials, using flow cytometry, are shown here and compared to the expression in fully induced TET-ON system at  $50\mu\text{M}$  Doxycyclin. Error bars represent the standard deviation from the mean across all samples.

Compared to  $P\_RC1$ ,  $P\_TEF1$  was found to increase detection range as it was less affected by noise (Figure 3.5). Although  $P\_RC1$  was not tested in this study, it has been previously shown to have similar promoter strength as  $P\_CLN3$  [28]. Using  $P\_TEF1$  to drive PI(4,5)P<sub>2</sub> binding GFP was found to show a stronger fluorescence signal compared to expression by  $P\_RC1$  (Figure 3.5). The stronger fluorescence due to  $P\_TEF1$  resulted in large differences between the background fluorescence and average fluorescence at the plasma membrane, which was not observed in using  $P\_RC1$  (Figure 3.5). Using  $P\_TEF1$  to drive expression of PI(4,5)P<sub>2</sub> binding GFP was found to also increase sensitivity in detecting differences between the plasma membrane and cytosol signal in the cell (Figure 3.5). Using a strong promoter to drive expression of PI(4,5)P<sub>2</sub> binding GFP was not only found to be less affected by noise but was also able to produce differences between plasma membrane and cytosolic bound signal, which was not observed in expression patterns using  $P\_RC1$ . A local maximum at the plasma membrane was observed in the plot profiles of cells that drove expression using  $P\_TEF1$ , whereas the plot profile from cells driving

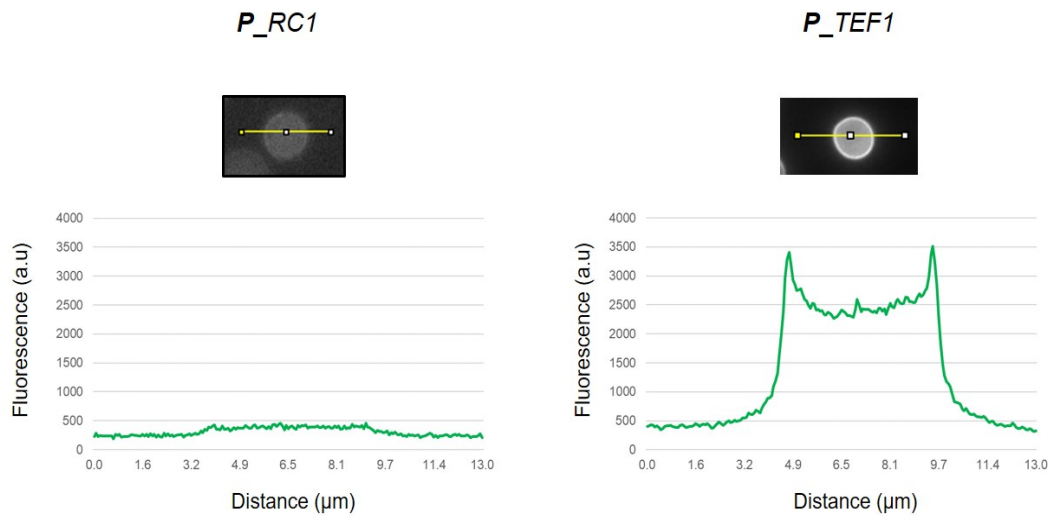


Figure 3.5: Effect of promoter strength on detection range of GFP-2XPH(PLC $\delta$ ) construct. Representative plot profiles of cells expressing  $P\_TEF1$  and  $P\_RC1$  driven GFP-2XPH(PLC $\delta$ ). Inset shows original image of cell and yellow line shows the line drawn to determine profile plot.

expression using  $P\_RC1$  did not show differences between plasma membrane or cytosolic signal. The difference observed between the plasma membrane and cytosolic signal, using  $P\_TEF1$ , became the basis of the quantification method that was developed in this study. The quantification method is based on determining the relative proportion of signal at the plasma membrane to the cytosol and this requires a good range of fluorescence in the cell.

### 3.3.2 Orientation of PI(3,4,5)P<sub>3</sub>- binding mCherry reporter affected fluorescence signal

The PH(AKT)-mCherry construct showed at least 5 times stronger signal compared to the mCherry-PH(AKT) construct, which showed a much weaker signal (Figure 3.6). As fluorescence is dependent on the rigid  $\beta$ -barrel structure that forms as a result of the way the fusion protein folds, the orientation of the protein can affect the fluorescence properties. Unlike the PI(4,5)P<sub>2</sub>- binding GFP construct, the construction of the PI(3,4,5)P<sub>3</sub>- binding PH(AKT)-mCherry construct proved to be a little more cumbersome. The fusion of PH(AKT) at the C-terminus and the N-terminus of the mCherry protein was compared and the C-terminus construct was found to diminish mCherry signal (Figure 3.7).

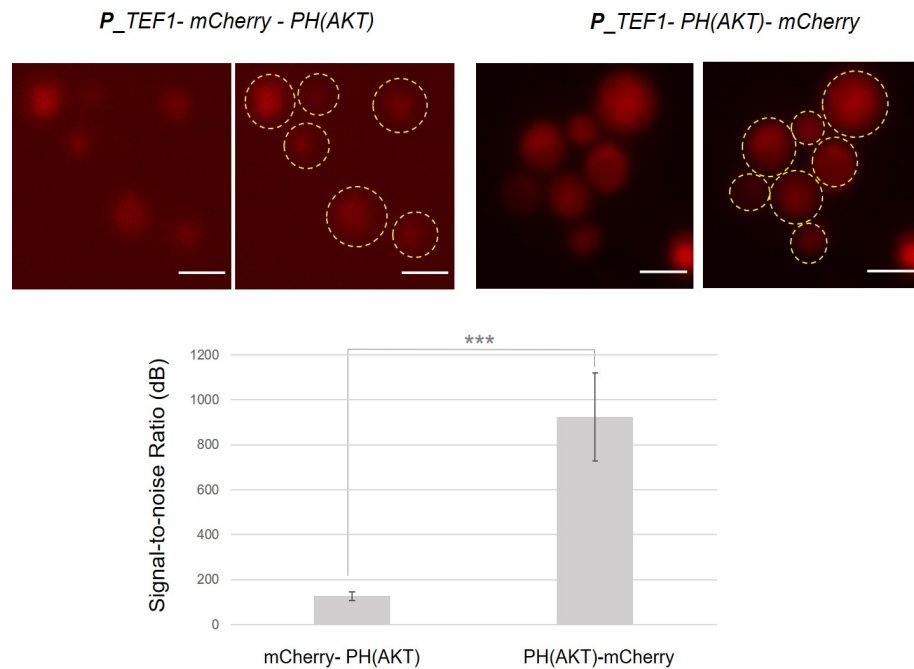


Figure 3.6: C-terminus fusion of PH(AKT) domain diminished mCherry signal in the cell. The signal-to-noise ratio was calculated from mCherry expressing cells across three images. The error bars represent the standard deviation and t-test was performed to determine significance ( $p < 0.05$ ). Scale bars represent  $5\mu\text{m}$ . Inset shows representative images of cells, which are outlined with the yellow line.

### 3.3.3 Illustrating $P\_TEF1$ , codon optimised $\text{PI}(3,4,5)\text{P}_3$ - binding mCherry construct showed increased detection range compared to $P\_CLN3$ , non-codon optimised mCherry construct

Under the same image acquisition settings, the  $P\_TEF1$ - PH(AKT)-mCherry (codon optimised) construct and the  $P\_CLN3$ - PH(AKT)-mCherry (non codon optimised) construct were compared (Figure 3.7). The development of a sensitive mCherry construct to reliably reflect quantifiable changes between plasma membrane and cytosolic signal was required for the construction of a functional dual reporter system. In addition to increasing promoter strength, changing mCherry signal to a codon optimised version also increased detection range in the  $\text{PI}(3,4,5)\text{P}_3$ - binding mCherry construct. The resulting  $P\_TEF1$ -PH(AKT)-mCherry codon optimised construct showed quantifiable differences between low and high  $\text{PI}(3,4,5)\text{P}_3$  states in the cell as well as differences between plasma membrane and cytosolic signal across cells. Quantifiable differences were not as clearly observed in cells expressing  $P\_CLN3$ -

*PH(AKT)*-*mCherry* construct.

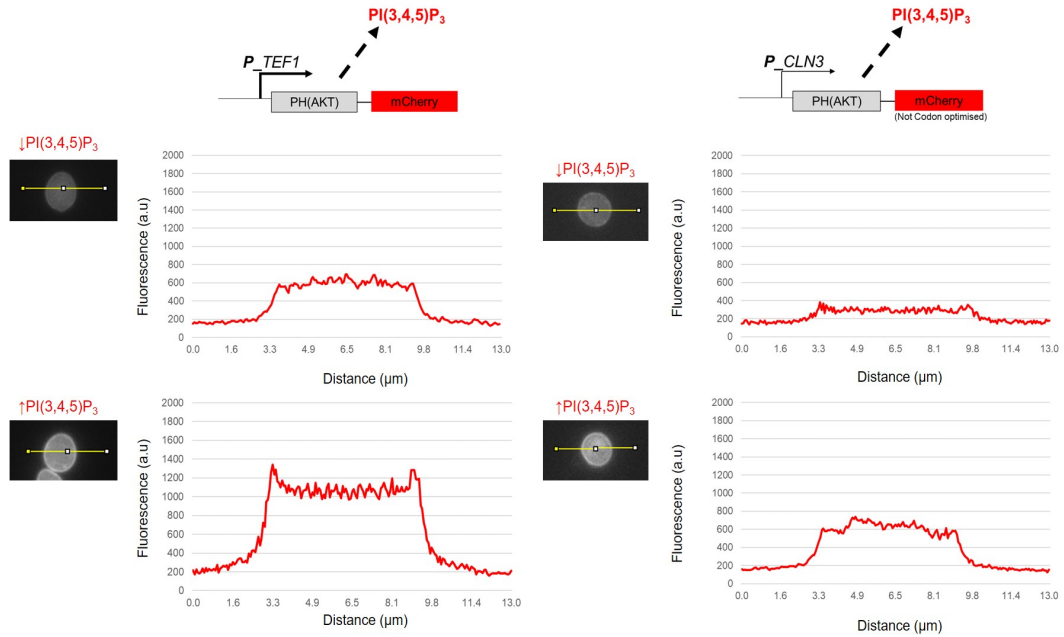


Figure 3.7: Representative plot profiles comparing PI(3,4,5)P<sub>3</sub>- binding mCherry constructs. Cells containing *P\_TEF1-PH(AKT)-mCherry* yeast codon optimised construct and *P\_CLN3-PH(AKT)-mCherry* non-yeast codon optimised construct were uninduced and induced to express p110 $\alpha_L$  in the cell. Localisation of mCherry was detected using fluorescence microscopy (inset). The profile plot across the cell (yellow line) was determined for each cell.

### 3.4 Automated measurement

As discussed in Chapter 2, a machine-learning image segmentation algorithm was developed to increase the number of images that can be quantified. The algorithm was developed using the TensorFlow Application Programming Interface (or API). The TensorFlow API is an open source machine-learning platform that can be used to develop and retrain machine-learning models. In this study, we retrain the MobileNetV2 model to detect circular cells within the image. MobileNet models use depthwise separable convolution as efficient building blocks to extract useful information from the input image. Due to the increased efficiency in the convolution method, the model is useful in increasing processing speed and reducing the amount of memory required for image processing. In addition to the depthwise separable convolution, the MobileNetV2 model also performs a shortcut connection between

processing layers. The two processing blocks allow to further increase efficiency of image detection.

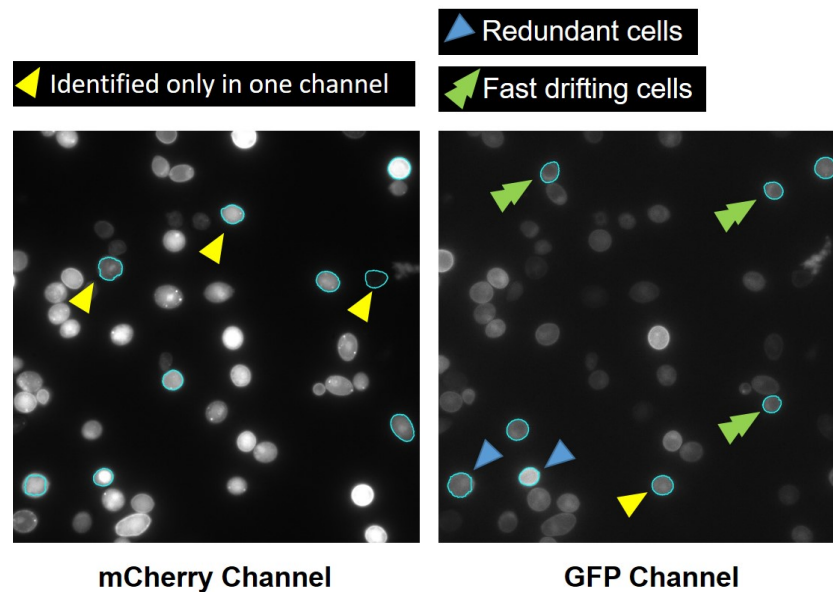


Figure 3.8: Cell boundary detection between both mCherry and GFP channels. Different cells are shown to be detected between the two channels and cells that were used for measurement included unique boundaries across both channels.

## 3.5 Discussion of building the synthetic system

### 3.5.1 Expression of p110 $\alpha$ was tolerated in the cell

Using the design considerations of introducing p110 $\alpha$  expression in the cell, p110 $\alpha_M$  did not result in complete growth inhibition, which was reported in previously published studies (Figure 3.1). Chapter 2 introduces the design considerations that maybe required to reduce cell toxicity caused by the p110 $\alpha$ -CAAX (or p110 $\alpha_M$ ) construct (Table 2.1). Here, I show that by reducing the number of copies of p110 $\alpha_M$  in the cell and controlling expression using an inducible synthetic promoter we can reduce the toxic effects of p110 $\alpha_M$ , which was previously thought to result in total inhibition of cell growth.

The loop version, p110 $\alpha_L$  was found to have the most effect on the doubling time, which was  $\approx 20\%$  more than the other constructs at the 62.5nM of  $\beta$ -estradiol (Figure 3.1). As per the design of the three versions, the membrane version, p110 $\alpha_M$  was

expected to have higher toxicity than the loop and cytosolic versions but this was not observed suggesting that, direct binding of p110 $\alpha_L$  is faster than the membrane targeting of low copy number p110 $\alpha_M$ .

### 3.5.2 Increased detection range of dual reporter is due to larger amount of reporter available in the cell

To observe the membrane dynamics using changes in the levels of PI(3,4,5)P<sub>2</sub> to PI(3,4,5)P<sub>3</sub>, a robust dual reporter system was constructed to allow detection. PH domains are  $\approx$ 100–120 amino acids in length and are known to bind to phosphatidylinositol phosphate derivatives in eukaryotic cell membranes. The PH domain of PLC $\delta$  is known to bind to PI(4,5)P<sub>2</sub> with high selectivity and specificity [39]. The PH domains from AKT, in mammalian cells is known to bind to PI(3,4)P<sub>2</sub> and PI(3,4,5)P<sub>3</sub> at the plasma membrane; however, PH(AKT) is known to bind to PI(3,4,5)P<sub>3</sub> with high specificity in *S. cerevisiae* [17]. The resulting dual reporter system constituted PH(AKT)-mCherry and GFP-2XPH(PLC $\delta$ ) to detect levels of PI(3,4,5)P<sub>2</sub> and PI(4,5)P<sub>2</sub> levels, respectively. The N-terminal PH(AKT)-mCherry construct was compared to the C-terminal mCherry-PH(AKT) construct and mCherry signal was not affected in the cell. The GFP-2XPH(PLC $\delta$ ) construct was based on previous studies that showed high specificity to PI(4,5)P<sub>2</sub> (Table 2.1). Localisation patterns of the dual reporter were consistent with expected increase of p110 $\alpha$  expression in the cell as GFP and mCherry were detected at the plasma membrane in low and high PI(3,4,5)P<sub>3</sub> states, respectively.

The expression of both the reporter proteins were controlled by the a strong constitutive promoter ( $P_{TEF1}$ ). Using a strong constitutive promoter resulted in an increase in the detection range, which allowed a reliable basis for the quantification method. Both mCherry and GFP constructs showed quantifiable differences between plasma membrane and cytosol signal within a single cell and between basal and induced expression. The increase in detection range might be attributed to the increase in the reporter protein available as a result of the strong constitutive promoter in the cell. The increase in the amount of protein available in the cell ensures that the fluorescence detected at the plasma membrane is not limited by the reporter

protein level but by the growth rate of the cell i.e, the availability of RNA polymerase and other transcription factors. The effect of p110 $\alpha$  on growth rate could be used to explain the difference between the maximum GFP fluorescence observed at the plasma membrane in control and p110 $\alpha$  cells. The amount of fluorescence itself does not affect the machine-learning based quantification method as the relative amounts of fluorescence are calculated but, the increase in the detection range allows a more accurate calculation of the relative amounts of PI(3,4,5)P<sub>3</sub>. There are two types of noise that were found to affect the reliability of the dual reporter system and included noise due to image detection from the camera and intrinsic noise within each image (also described as the signal-to-noise). The increased dynamic range of the optimised dual reporter system shown here reduces the effects of noise in the image.

### 3.5.3 Advantages and limitations of using machine-learning based algorithm

The major advantage that was found using the developed machine-learning based algorithm was that cells were detected across both channels, which reduced user-defined bias. The automated machine learning algorithm was able to detect cells across both mCherry and GFP channels, which was not performed manually. Manual segmentation resulted in cells defined in either mCherry or GFP channel depending on predicted behaviours of the system, which introduced user-defined bias. The automation of image segmentation was able to overcome such user define bias as well as increasing the number of images that were processed.

The major drawback was that selection of cells was not perfect in spite of long processing times. Compared to manual segmentation, the number of cells detected in one channel were fairly large compared to manually defined cells, where the user could avoid fast drifting cells and irregular shaped cells as well as identify cells that are different from a group of cells however, training from scratch requires larger data sets for learning as well as hundreds of hours. Retraining models on the other hand, allows the user to take a piece of the existing model that has already been trained to perform a similar task, saving several hours that is required for training from scratch using neural networks.

## Chapter 4

# Testing functionality of the components of the system

### 4.1 Summary

This chapter tests the functionality of the components expressing p110 $\alpha$  and PTEN constructs, using the dual reporter system and the quantification method that were described in the previous chapters. Differences between membrane dynamics of the different versions of p110 $\alpha$  were confirmed and as the dual-reporter showed clear differences between these constructs, which were quantified using the machine-learning based algorithm. The quantification method showed that basal expression was present in the component expressing p110 $\alpha$  as there was an increase in the *PIP*<sub>3</sub>-Index across uninduced cells. Functionality of the PTEN component was also confirmed using the cytosolic PTEN as the *PIP*<sub>3</sub>- Index was reduced in cells containing high copy of PTEN<sub>C</sub>, where basal expression was also detected. The difference between basal and induced expression was compared using immunoblotting. All the components in the system were thus confirmed to be functional according to the design rationale for the synthetic system (Chapter 2).

## 4.2 Quantification of p110 $\alpha$ dynamics at the plasma membrane

The three versions of p110 $\alpha$  (p110 $\alpha_C$ , p110 $\alpha_L$  and p110 $\alpha_M$ ) were integrated to the genome of *S. cerevisiae* cells along with the dual reporter system. A control with no p110 $\alpha$  was maintained and cells were induced to express the p110 $\alpha$  versions, using the GEV system. The different versions, p110 $\alpha_C$ , p110 $\alpha_L$  and p110 $\alpha_M$  were expected to have increasing effects at the plasma membrane and the control was expected to have no effect at the plasma membrane (Figure 4.1).

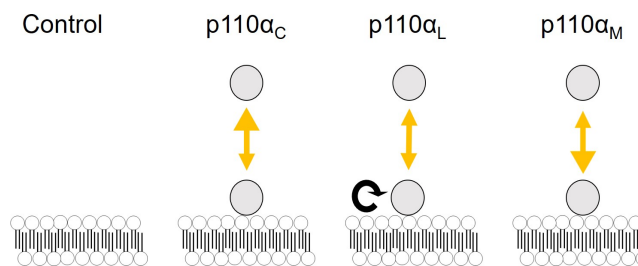


Figure 4.1: Schematic diagram illustrating membrane dynamics of different p110 $\alpha$  versions. The plasma membrane is represented as the bilipid layer and the theoretical behaviour of the three different p110 $\alpha$  versions is shown here. The control describes cells with no p110 $\alpha$  present in the cells.

### 4.2.1 p110 $\alpha_M$ showed highest plasma membrane activity due to basal expression

Some basal expression was expected using the GEV system and activity due to basal expression in the cell was detected by the dual reporter system. In the untreated condition, p110 $\alpha_M$  showed an increased amount of mCherry at the plasma membrane compared to the other constructs (Figure 4.2). The increase in mCherry signal due to basal expression confirmed as the plot profile showed that both mCherry and GFP were present at the plasma membrane, which was not observed in the other versions of p110 $\alpha$ . The increase in mCherry at the plasma membrane confirmed that p110 $\alpha_M$  activity was stronger than the other versions used in this study. This confirmed that the plasma membrane targeting through the CAAX domain was functional and consistent with the design of the construct (see Chapter 2).

### 4.2.2 Activity due to basal expression of p110 $\alpha_C$ and p110 $\alpha_L$ are comparable

Cells with p110 $\alpha$  versions showed decreased GFP signal at the plasma membrane, compared to the control (Figure 4.2). In cells with p110 $\alpha$  versions, the GFP signal at basal expression was found to be almost 1000 units less than in the control cells. As the dual reporter strains are genetically identical across all the versions and the image acquisition settings were kept the same throughout this study, the decrease in the GFP signal at the plasma membrane suggested that activity due to basal expression of the p110 $\alpha$  versions was detected by the dual reporter system. In the p110 $\alpha_C$  and p110 $\alpha_L$  versions, the amount of PI(3,4,5)P<sub>3</sub> due to basal expression did not result in an increase in the mCherry signal observed at the plasma membrane.

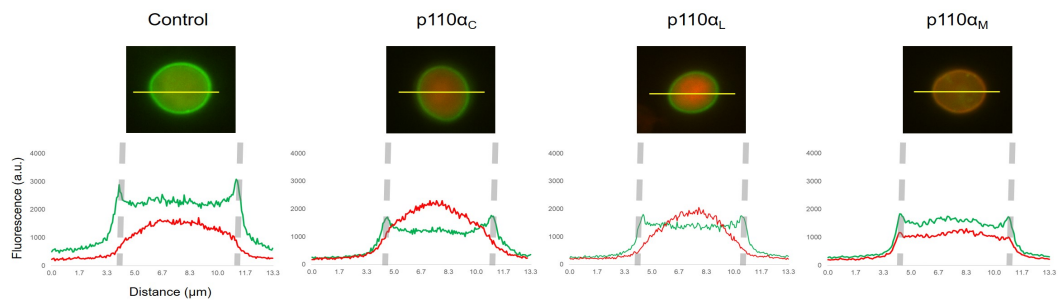


Figure 4.2: Representative profile plots of basal expression of the different versions of p110 $\alpha$  used in this study. Uninduced cells were observed using fluorescence microscopy (inset). A line was drawn across the cell to determine the fluorescence profile plot in both mCherry (red) and GFP (green) channels. Dotted line in profile plots represents the plasma membrane as detected by the dual reporter system.

### 4.2.3 Induced activity of p110 $\alpha_C$ did not have a significant increase in mCherry at the plasma membrane

Although the difference between GFP signal was observed between control cells and p110 $\alpha_C$  expression, no significant difference was observed at the plasma membrane due to induction of p110 $\alpha_C$  (Figure 4.3). The amount of mCherry at the plasma membrane was expected to increase due to induction of p110 $\alpha_C$  expression in the cell; however, this was not observed as the amount of mCherry fluorescence decreased across the cell.

#### 4.2.4 Induced activity of p110 $\alpha_L$ and p110 $\alpha_M$ resulted in high levels of mCherry at the plasma membrane

Compared to basal expression, induced expression of p110 $\alpha_L$  and p110 $\alpha_M$  showed an increase in the amount of mCherry observed at the plasma membrane (Figure 4.3). Full expression of p110 $\alpha_M$  was found to increase the amount of mCherry observed at the plasma membrane and resulted in mCherry at the plasma membrane and a shift of GFP signal detected in the cytosol (high PI(3,4,5)P<sub>3</sub> state). The p110 $\alpha_M$  version showed a greater increase in mCherry fluorescence at the plasma membrane, which was not observed in the other p110 $\alpha$  versions. The pattern observed in the p110 $\alpha_L$  cells showed that there was an increase in the mCherry signal that was similar to the GFP signal in the cell. The GFP signal was found to be similar between basal and induced expression of p110 $\alpha_L$  conditions.

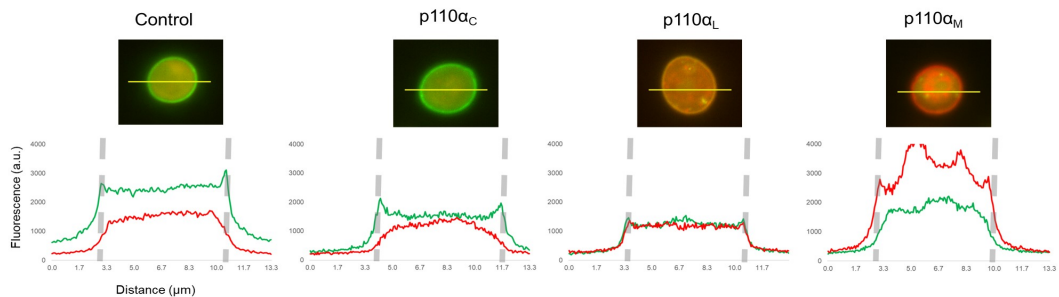


Figure 4.3: Representative plot profiles of induced expression of the different versions of p110 $\alpha$  used in this study. Cells induced to express p110 $\alpha$  at 25nM  $\beta$ -estradiol were observed using fluorescence microscopy and a line was drawn across the cell to determine profile plots in both mCherry (red) and GFP (green) channels (inset). Dotted line represents the plasma membrane as detected by the dual reporter system.

### 4.3 Quantification across the cell population reflected differences observed across the different versions of p110 $\alpha$

Quantification of the different versions of p110 $\alpha$ , reflected membrane dynamics as mean PIP<sub>3</sub>- Indexes across the population reflected changes observed using the dual reporter system (Figure 4.4). Significant differences observed between basal expression and induced expression across all p110 $\alpha$  versions. Statistical significance was determined using Mann-Whitney Test as data did not always fit normal distribution.

Negative mean PIP<sub>3</sub>-Indexes were associated with low PI(3,4,5)P<sub>3</sub>- states and positive PIP<sub>3</sub>-Indexes were associated with high PI(3,4,5)P<sub>3</sub> states (Figure 4.4). The mean PIP<sub>3</sub>-Indexes showed that the activity at the plasma membrane was highest in  $p110\alpha_M > p110\alpha_L > p110\alpha_C$ .

High plasma membrane activity was associated with  $p110\alpha_M$  as both basal and induced expression resulted in positive mean PIP<sub>3</sub>-Indexes, which were significantly greater than the other versions of  $p110\alpha$  (Table ??). In the induced condition, the  $p110\alpha_M$  version showed a more positive distribution across the cell population and the mean PIP<sub>3</sub>-Index was found to be higher than the other versions. Even at basal expression,  $p110\alpha_M$  resulted in a more positive mean than the other versions. Taken together, the plasma membrane associated activity of  $p110\alpha_M$  version produced more PI(3,4,5)P<sub>3</sub> compared to the other versions.

Low plasma membrane activity was associated with  $p110\alpha_C$  as little difference was observed between the mean PIP<sub>3</sub>-Indexes between basal and induced expression (Table ??). In both expression conditions,  $p110\alpha_C$  showed the least amount of mCherry at the plasma membrane. The low mCherry and high GFP was reflected in quantification across the cell population as majority of the quantified cells had negative PIP<sub>3</sub>-Indexes. The distribution at basal expression was found to be more positive than the distribution of cells at induced expression; however, this difference was smaller than the differences observed between basal and induced expression in the other  $p110\alpha$  versions. The difference between basal and induced expression in the membrane bound  $p110\alpha_L$  and  $p110\alpha_M$  was > 20% whereas, the difference was found to be 17% and 18% in  $p110\alpha_C$  and control cells, respectively.

Bimodal distribution, or the presence of two subpopulations within a single population, was observed across the induced  $p110L$  cells (Figure 4.4). Although, high mCherry signal was observed in cells expressing  $p110\alpha_L$ , the mean PIP<sub>3</sub>-Index was found to be negative across the cell population. The bimodal distribution observed across the cell population suggests that induction of  $p110\alpha_L$  resulted in the maintenance of two subpopulations, one with low and the other with high PIP<sub>3</sub>-Indexes.

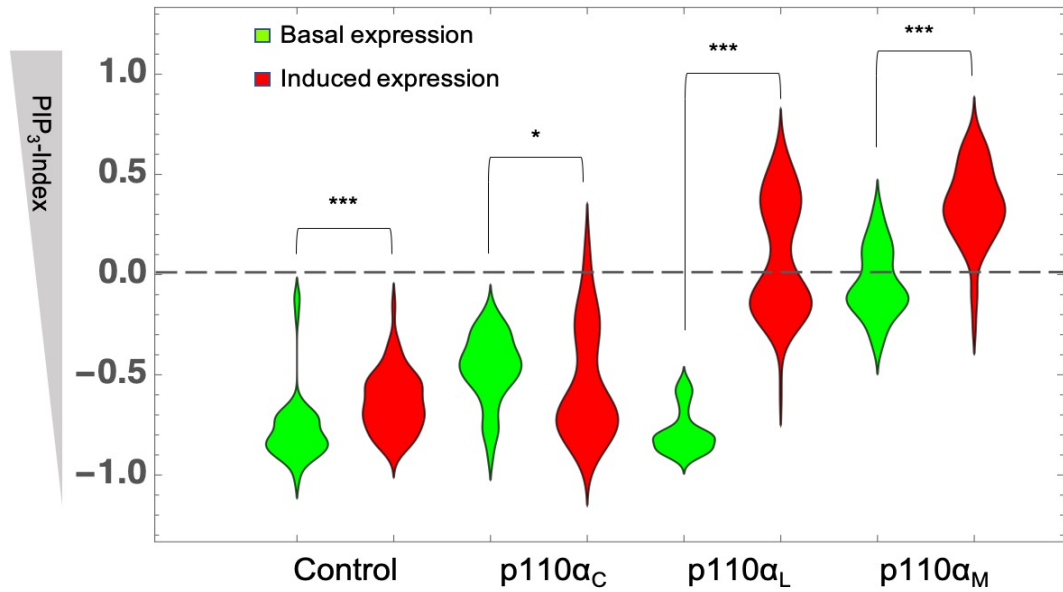


Figure 4.4: Distribution plots of  $PIP_3$ -Indexes across p110 $\alpha$  cells. The relative amounts of PI(3,4,5) $P_3$  production across the different p110 $\alpha$  versions were quantified across uninduced and induced cell populations. In total, 50-80 cells were quantified in uninduced and in fully induced p110 $\alpha$  expression conditions across the different versions of p110 $\alpha$ . Here, changes in the distribution of  $PIP_3$ - Index in uninduced condition are referred to as basal expression. Mann-whitney test was performed between samples to show that the distributions between the two treatments differed significantly (\* $p < 0.05$ , \*\*\* $p < 0.0001$ ).

#### 4.4 PTEN functionality test

Next, I tested the functionality of the PTEN components, which included expression control with the TET-ON system and the dephosphorylation activity of PTEN. Using the cytosolic version of PTEN, PTEN<sub>C</sub>, the functionality of the component was tested because the sequence was used to construct the other versions of PTEN, PTEN<sub>L</sub> and PTEN<sub>M</sub>. By fusing the 2XPH(PLC $\delta$ ) and CAAX domain to the C-terminus of the PTEN<sub>C</sub>, PTEN<sub>L</sub> and PTEN<sub>M</sub> were constructed, respectively. The sequence also contained a K13E mutation, which was introduced to disrupt the natural PI(4,5) $P_2$ -binding activity of the wildtype human protein that was used in this study. Expression was controlled using the TET-ON system, which is induced using doxycycline. To test the functionality of PTEN<sub>C</sub> cells were induced to co-express p110 $\alpha_L$  and PTEN<sub>C</sub>, as the activity of the latter requires production of PI(3,4,5) $P_3$ .

Using the dual reporter system, dephosphorylation activity was observed in high copy number  $PTEN_C$ , which was induced to co-express  $p110\alpha_L$  and  $PTEN_C$ . The copy number of genome integrated  $PTEN_C$  was quantified across transformants and three strains bearing three different copy numbers were selected to confirm functionality of  $PTEN_C$  (Figure 4.5). Co-expression of high copy number  $PTEN_C$  and  $p110\alpha$  showed that there was more GFP detected at the plasma membrane compared to the low and intermediate copy number cells (Figure 4.6). The GFP distribution at the plasma membrane confirms levels of dephosphorylation of  $PI(3,4,5)P_3$ , resulting in  $PI(4,5)P_2$  at the plasma membrane. The levels of GFP observed at the plasma membrane in low and intermediate copy number strains was found to be comparable to the control strain which did not contain  $PTEN_C$  in the genome of the cell (Figure 4.6). The amount of mCherry that was detected at the plasma membrane was also found to be less in the high copy number strains, which confirmed dephosphorylation activity in the high copy number strain.

Quantification of the effects of copy number on the dephosphorylation activity of  $PTEN_C$  confirmed functionality of the component at high copy number. To observe differences between low, intermediate and high copy number of  $PTEN_C$ , cells were quantified across uninduced,  $p110\alpha_L$  expression and co-expression of  $p110\alpha_L$  and  $PTEN_C$  conditions. There was no significant difference observed between uninduced conditions across all strains that were tested. Significant difference was observed between cells with no  $PTEN_C$  and high copy number  $PTEN_C$  in the condition of  $p110\alpha_L$  expression as well as between cells with no  $PTEN_C$  and high copy number  $PTEN_C$  in the co-expression condition. These results suggested that high copy number  $PTEN_C$  effectively reduced the  $PI(3,4,5)P_3$  levels in the cell at basal and induced expression.

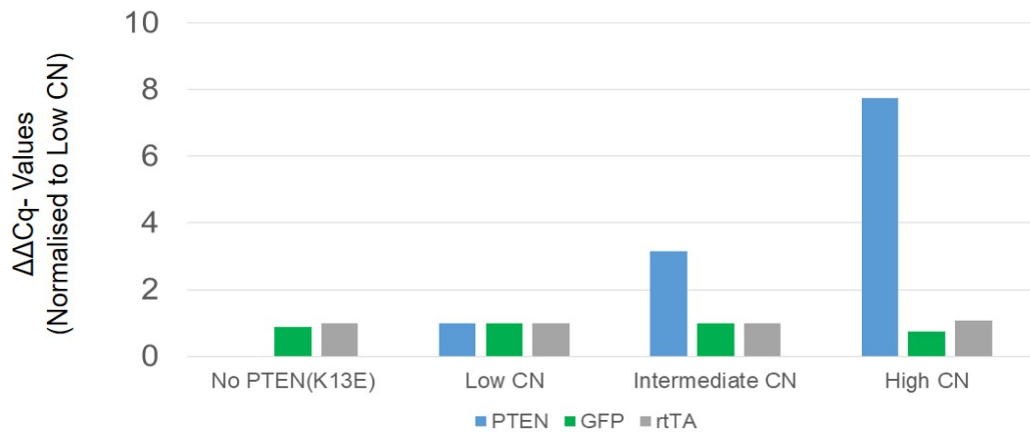


Figure 4.5: Copy number determination of PTEN<sub>C</sub> cells. Copy number of PTEN<sub>C</sub> cells was determined from a single qPCR trial. The  $\Delta C_q$ - value represents the change in the relative amounts of copy number across the samples. The values were normalised to the low copy number strain (Low CN). As PTEN<sub>C</sub> was introduced to cells that were made up of identical genetic background, GFP and rtTA, from the TET-ON system, were used as internal controls.

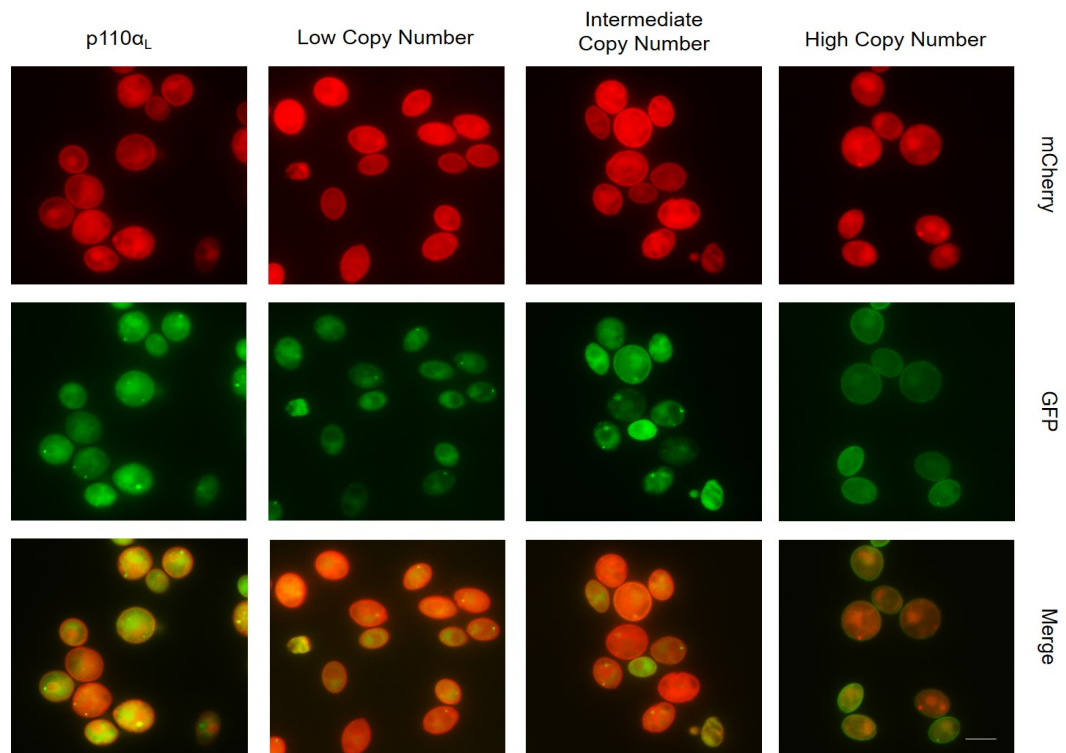


Figure 4.6: Effect of Copy number on amount of GFP observed at plasma membrane in cells co-expressing p110<sub>L</sub> and PTEN<sub>C</sub>. Cells containing different copy number of PTEN<sub>C</sub> were induced to co-express p110<sub>αL</sub> and PTEN<sub>C</sub>. Images of cells were compared across both mCherry and GFP channels. No PTEN<sub>C</sub> cells only contained p110<sub>αL</sub> in the genome. Scale bar represent 5 $\mu$ m.

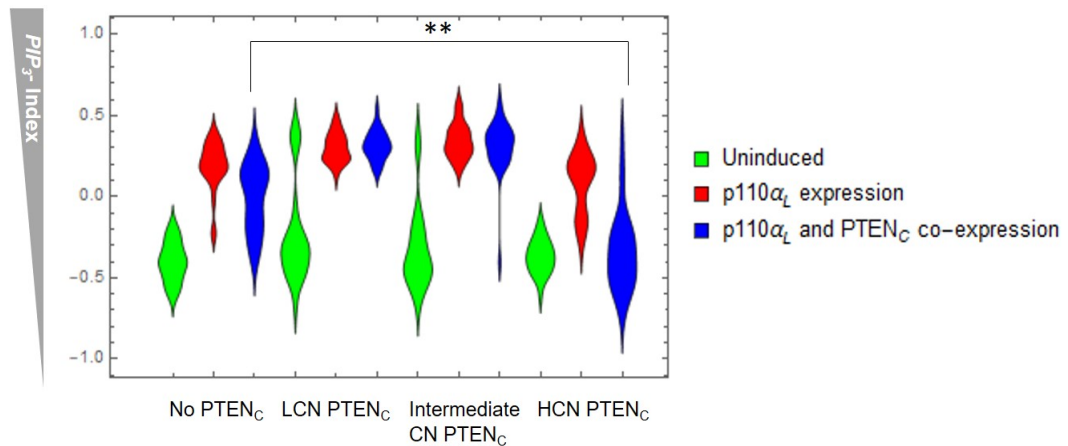


Figure 4.7: Distribution plots showing effect of  $PTEN_C$  copy number on  $PIP_3$ -Index. In total, 50-80 cells were quantified across three conditions: uninduced,  $p110\alpha_L$  expression and  $p110\alpha_L$  and  $PTEN_C$  co-expression. No  $PTEN_C$  cells were constructed as a control, without  $PTEN_C$  in the genome. LCN  $PTEN_C$  and HCN  $PTEN_C$  represent cells bearing low and high copy number of  $PTEN_C$  in the genome, respectively. Intermediate CN represents cells having intermediate levels of  $PTEN_C$ . Statistical significance between distributions were compared using Mann-whitney test (\*\* $p < 0.01$ ) are shown here.

#### 4.5 Quantification of basal expression levels of $p110\alpha_C$ and $PTEN_C$

The quantification of cells in the uninduced  $p110\alpha$  versions and  $p110\alpha_L$  expression in high copy number  $PTEN_C$  cells suggested that both components had basal expression in the cell. In the uninduced condition, cells containing different versions of  $p110\alpha$  showed significant differences in mean  $PIP_3$ -Indexes in a way that corresponded to their design (Table ??). For example,  $p110\alpha_M$  showed a more positive mean compared to  $p110\alpha_L$ , suggesting that more  $PI(3,4,5)P_3$  was present at the plasma membrane of the cell even in the absence of inducer. Similarly, significant difference was observed cells without  $PTEN_C$  and cells with high copy number  $PTEN_C$  that were induced to express only  $p110\alpha_L$  (Figure 4.7). These differences suggested that the dual reporter system was able to detect differences in the amount of  $PI(3,4,5)P_3$  at the plasma membrane of cells due to basal expression in the uninduced  $p110\alpha$  and  $PTEN_C$  cells.

basal expression in both GEV and TET-ON systems was confirmed by comparing induced and uninduced cells, expressing  $p110\alpha_C$  and  $PTEN_C$  (Figure 4.8).

Uninduced and induced cells containing cytosolic versions of p110 $\alpha$  and PTEN were subjected to immunoblotting and a difference of > 2- fold was observed between expression in uninduced and induced condition, across both GEV and TET-ON inducible systems (Figure 4.8). Compared to cells expressing PTEN<sub>C</sub> by full induction of TET-ON system, a stronger signal was detected in cells expressing p110 $\alpha$ <sub>C</sub> by full induction of expression by the GEV system. No signal was detected in cells that were fully induced but did not contain p110 $\alpha$ <sub>C</sub> or PTEN<sub>C</sub>, which confirmed that basal expression of the synthetic promoters resulted in basal levels of p110 $\alpha$  or PTEN in the cells even in the absence of inducer.

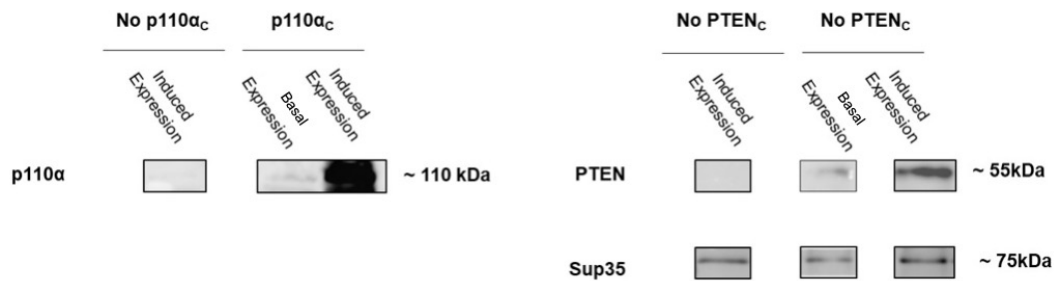


Figure 4.8: Induction of synthetic promoters showed >2- fold difference compared to basal expression. Immunoblotting was performed on induced and uninduced cells that were designed to express p110 $\alpha$ <sub>C</sub> or PTEN<sub>C</sub> using the GEV or TET-ON system, respectively. Induction of the GEV and TET-ON systems were done by treating cells with 25nM  $\beta$ -estradiol and 50mM doxycycline, respectively. No signal was observed in cells fully induced with GEV and TET-ON systems, but without p110 $\alpha$ <sub>C</sub> and PTEN<sub>C</sub>. Sup35 was used as a loading control in cells expressing PTEN<sub>C</sub>.

## 4.6 Discussion for testing functionality of the components of the system

### 4.6.1 Quantification method showed differences in p110 $\alpha$ membrane dynamics.

Using the machine-learning based quantification method, plasma membrane dynamics of p110 $\alpha$  across cell populations were found to be consistent with their theoretical design. Three constructs of p110 $\alpha$  were compared to show different membrane dynamics and resulted in corresponding differences in calculated *PIP*<sub>3</sub>-Indexes for basal and induced expression. The mean *PIP*<sub>3</sub>-Indexes showed that membrane ac-

tivity across the p110 $\alpha$  versions were found to be highest in p110 $\alpha_M$  > p110 $\alpha_L$  > p110 $\alpha_C$  in both basal and induced expression.

The cytosolic version, p110 $\alpha_C$  was fused to a poly-glycine flexible linker and was designed to have no membrane association properties. Activity at the plasma membrane associated with this construct was attributed to diffusion of the catalytic subunit from the cytoplasm to the membrane. Quantification of p110 $\alpha_C$  cells showed low negative PIP<sub>3</sub>-Indexes in both basal expression and induced expression, suggesting that activity at the plasma membrane was low as PI(4,5)P<sub>2</sub> levels were high even after induced expression (Figure 4.4).

On the other hand, p110 $\alpha_M$  showed the highest PIP<sub>3</sub>-Indexes at basal expression and induced expression suggesting that this version had the strongest membrane-bound activity. The increase in membrane-bound activity in the p110 $\alpha_M$  was attributed to fusion to the CAAX domain. The CAAX domain, is found at the C-terminus of a class of proteins known as CAAX proteins (eg: RasGTPase). This motif consists of a cysteine (C), any aliphatic amino acid (AA) and X for any amino acid. The mechanism through which the CAAX containing protein is targeted to the plasma membrane is well studied in yeast as it undergoes a series of post-translational modifications. These post-translational modifications include polyisoprenylation, endoproteolysis and carboxyl methylation [15]. Prenylation refers to the covalent modification of a molecule by the attachment of a lipophilic isoprenoid group. Isoprenoids are a family of lipophilic molecules based on repeating a C<sub>5</sub> structure that are synthesized from mevalonate, which is synthesized from the HMG-CoA pathway in the cell. During polyisoprenylation, a soluble protein prenyl-transferase (PPT) recognises the motif through the X residue [87]. After the sequence is recognised, the enzyme attaches either a farnesyl (C<sub>15</sub> chain) or a geranylgeranyl (C<sub>20</sub> chain) moiety to the cysteine via a thioester bond. The prenylated protein does not directly diffuse to the plasma membrane but has been shown to transiently localise to the endomembrane system, where they are recognised and cleaved by a membrane specific endopeptidase, known as prenyl-CAAX protease [20]. These proteases recognise the prenylated motif and cleave the -AAX residues, leaving behind the prenylated cysteine as the new C-terminus. The prenylated C-terminus then under-

goes methylesterification to cap the protein, making it even more hydrophobic in nature. Therefore, using the CAAX domain the p110 $\alpha_M$  version was expected to show activity at the plasma membrane even at basal expression and this was also reflected in quantification of the cells at basal expression.

The positive feedback loop version, p110 $\alpha_L$  was constructed so that the production of PI(3,4,5)P<sub>3</sub> would result in more PI(3,4,5)P<sub>3</sub> and was found to be functional because basal expression and induced expression resulted in low and high *PIP*<sub>3</sub>-Indexes, respectively. By fusing the PH(AKT) to the N-terminus of the p110 $\alpha$  catalytic subunit, a positive feedback loop was designed such that at low PI(3,4,5)P<sub>3</sub> levels cells would maintain low PI(3,4,5)P<sub>3</sub> levels but after reaching an unknown concentration of PI(3,4,5)P<sub>3</sub> more PI(3,4,5)P<sub>3</sub> is produced. Most studies use N-terminus fusion of the PH(AKT) domain that are based on the study by *Varnai et al* [96]. Only one study that was found to use the PH(AKT) domain at the C-terminus to construct a similar positive feedback loop in *S. cerevisiae* cells [17]. Here, we use the N-terminus construct because it did not appear to affect the loop behaviour of the p110 $\alpha_L$ . At basal expression, a low mean *PIP*<sub>3</sub>-Index, which was comparable to control cells was determined across the cell population. At induced expression, the mean *PIP*<sub>3</sub>-Index increased and showed a more positive distribution. The N-terminus PH(AKT)-p110 $\alpha$  construct was also used in this study because it had a similar orientation to the reporter PH(AKT)-mCherry protein, which was shown to be functional at the plasma membrane of *S. cerevisiae*.

#### 4.6.2 PTEN component was found to be functional and was used to study plasma membrane dynamics

The PTEN component used in this study included a K13E mutant and was found to be functional only when integrated at high copy number to the genome of the cell. The mammalian PTEN sequence is made up of a C2 domain, a phosphatase domain and C-tail [49]. The phosphatase region of PTEN is responsible for dephosphorylation of PI(3,4,5)P<sub>3</sub> to produce PI(4,5)P<sub>2</sub> and the C-tail is thought to block the phosphatase region preventing the dephosphorylation of PI(3,4,5)P<sub>3</sub>. Upon binding of C2-domain to PI(4,5)P<sub>2</sub> the conformation is thought to change and allow dephos-

phorylation of PI(3,4,5)P<sub>3</sub> thereby, establishing a positive feedback loop as PTEN preferentially acts on membranes enriched with PI(4,5)P<sub>2</sub> and PI(3,4,5)P<sub>3</sub> at the plasma membrane of cells. The K13E mutation is found as a hallmark mutation in several human cancers [1]. The mutation is associated with a loss of function of dephosphorylation of PI(3,4,5)P<sub>3</sub> by PTEN [14] In this study, the K13E mutation was introduced to disrupt the PI(4,5)P<sub>2</sub> binding ability of the human sequence that was used in this study to prevent localisation to the membrane by the C2- domain. No dephosphorylation activity was observed in the cells when PTEN was integrated to the genome at low or intermediate copy number but dephosphorylation activity was observed at high copy number. This result suggests that at low copy number, binding through the C2- domain was disrupted as there was not sufficient diffusion to the membrane to increase the amount of GFP detected at the system. At high copy number, the diffusion to the membrane was increased by virtue of increased concentration in the cell and this was found to increase the amount of GFP that was detected at the plasma membrane. Therefore, the membrane binding of PTEN plays an important role in dephosphorylation activity at the plasma membrane.

### 4.6.3 PTEN basal activity in cells increases with p110 $\alpha_C$ induction

basal expression of PTEN<sub>C</sub> was found to have no effect in uninduced cells but reduced *PIP*<sub>3</sub>-Index in cells expressing p110 $\alpha_C$ . Compared to cells without PTEN<sub>C</sub>, cells expressing p110 $\alpha_L$  were found to have significant difference between distributions of *PIP*<sub>3</sub>- Indexes. In the previous chapter, I show that expression of p110 $\alpha_L$  increases doubling time in the cell and thus, the difference between the *PIP*<sub>3</sub>- Index is thought to be due to the accumulation of basal PTEN<sub>C</sub>.

If the amount of PI(3,4,5)P<sub>3</sub> that is detected at the membrane by mCherry (M) is dependent on the amounts of p110 $\alpha_L$  (M<sub>P</sub>) and PTEN<sub>C</sub> (M<sub>D</sub>) available in the cell as well as the dilution due to cell division (C <sub>$\mu$</sub> ), then the change in PI(3,4,5)P<sub>3</sub> can be expressed as:

$$dM = M_P - M_D - MC_\mu \quad (4.1)$$

at steady-state, dM = 0 and solving for M gives:

$$M = \frac{M_P}{C_\mu} - \frac{M_D}{C_\mu} \quad (4.2)$$

At low PI(3,4,5)P<sub>3</sub> levels, p110 $\alpha_L$  has a greater effect than PTEN<sub>C</sub> in the cell. Basal expression of PTEN<sub>C</sub>,  $M_D < C_\mu$ , or the dilution due to cell division, the signal detected at the plasma membrane is dependent on the basal expression of p110 $\alpha_C$  ( $M_P$ ). At high levels of PI(3,4,5)P<sub>2</sub>,  $C_\mu$  is reduced and the mCherry signal observed at the plasma membrane is affected by the accumulation of both PTEN<sub>C</sub> and p110 $\alpha_L$  basal expression, suggesting that basal expression of PTEN constructs should have an increased effect in cells that have slower growth rate caused by elevated levels of PI(3,4,5)P<sub>3</sub> at the plasma membrane of the cell.

## Chapter 5

# Understanding bistability at the plasma membrane

### 5.1 Summary

This chapter describes the application of the synthetic system to study membrane dynamics in live cells. Using all four functional components of the system, the conditions for bistability across the population were examined. Bistability is the characteristic of a system to exist in two stable steady states and the system can be forced into any one stable state based on its history. Bistability is closely related to bimodality, which describes the presence of two populations in a single population and to test the stability of these two populations within a single genetically identical population, hysteresis experiments were designed. The results show that the conditions for bistability that were identified in this study required a two component positive feedback system.

### 5.2 Assessment of conditions for bimodality across cell populations

Three constructs showed significant bimodal distribution across cell populations (Figure 5.1). To test changes in plasma membrane dynamics, the different combinations of p110 $\alpha$  and PTEN versions were tested across three conditions: (i) basal expres-

sion of p110 $\alpha$  and PTEN (no inducer); (ii) induced expression of p110 $\alpha$  and (iii) co-expression of p110 $\alpha$  and PTEN (Figure 5.1). In general, all loop and membrane versions contained low copy number of PTEN and p110 $\alpha$ ; whereas, high copy number cells were selected for the cytosolic constructs. The distributions across all conditions were significantly different across the different combinations as well as across the different conditions. The significance of bimodal distribution was determined using Hartigan diptest, which indicates that p-values closer to zero show significant bimodal distribution [48]. Significant bimodality was observed in cells that co-expressed PTEN<sub>C</sub> and p110 $\alpha$ <sub>L</sub> (p<0.01); co-expressed PTEN<sub>L</sub> and p110 $\alpha$ <sub>L</sub> (p<0.01) and in uninduced cells containing PTEN<sub>C</sub> and p110 $\alpha$ <sub>M</sub> (p < 0.01). All three combinations showing bimodality contained cells that either showed high GFP or high mCherry at the plasma membrane (Figure 5.2 and 5.3). For simplicity, cells containing PTEN<sub>C</sub> and p110 $\alpha$ <sub>L</sub> will be referred to as the "one-loop" construct, cells containing PTEN<sub>L</sub> and p110 $\alpha$ <sub>L</sub>, the "two-loop" construct.

Intermediate levels of bimodality were also detected across constructs in which conditions caused small differences between PTEN and p110 $\alpha$  activity at the plasma membrane (Figure 5.4). For example, in cells containing PTEN<sub>M</sub> and p110 $\alpha$ <sub>L</sub>, the mean PIP<sub>3</sub> Index across the three conditions was found to be -0.14, -0.08 and -0.13 for uninduced, p110 $\alpha$ <sub>L</sub> expression and co-expression of PTEN<sub>L</sub> and p110 $\alpha$ <sub>L</sub> cells, respectively. The uninduced condition were associated with a low significance of bimodality (p-value = 0.88) and cells in this construct showed high-GFP and no mCherry signal at the plasma membrane (Figure 5.1 and 5.4). When p110 $\alpha$ <sub>L</sub> expression was induced, the bimodality in the population was more significant (p-value = 0.79) as cells showed some mCherry signal at the plasma membrane but predominantly showed GFP at the plasma membrane. Co-expression of p110 $\alpha$ <sub>L</sub> and PTEN<sub>M</sub> further increased significance of bimodality (p=0.47) and cells showed very strong GFP- no mCherry signal at the plasma membrane or strong-GFP- weak mCherry signal at the plasma membrane.

In summary, different versions of p110 $\alpha$  and PTEN resulted in different significance in bimodality. Across all constructs, except for p110 $\alpha$ <sub>M</sub> + PTEN<sub>C</sub>, uninduced cells showed low significance of bimodality. On the other hand, cells co-expressing

p110 $\alpha$  and PTEN showed higher significance of the bimodality, compared to the other conditions. Expression of p110 $\alpha_L$  also showed high significance of bimodality, which was not observed in cells containing the PTEN $_M$  version in the cell. The co-expression of p110 $\alpha$  and PTEN in the one-loop and two-loop constructs was found to result in the most significant bimodal distribution.

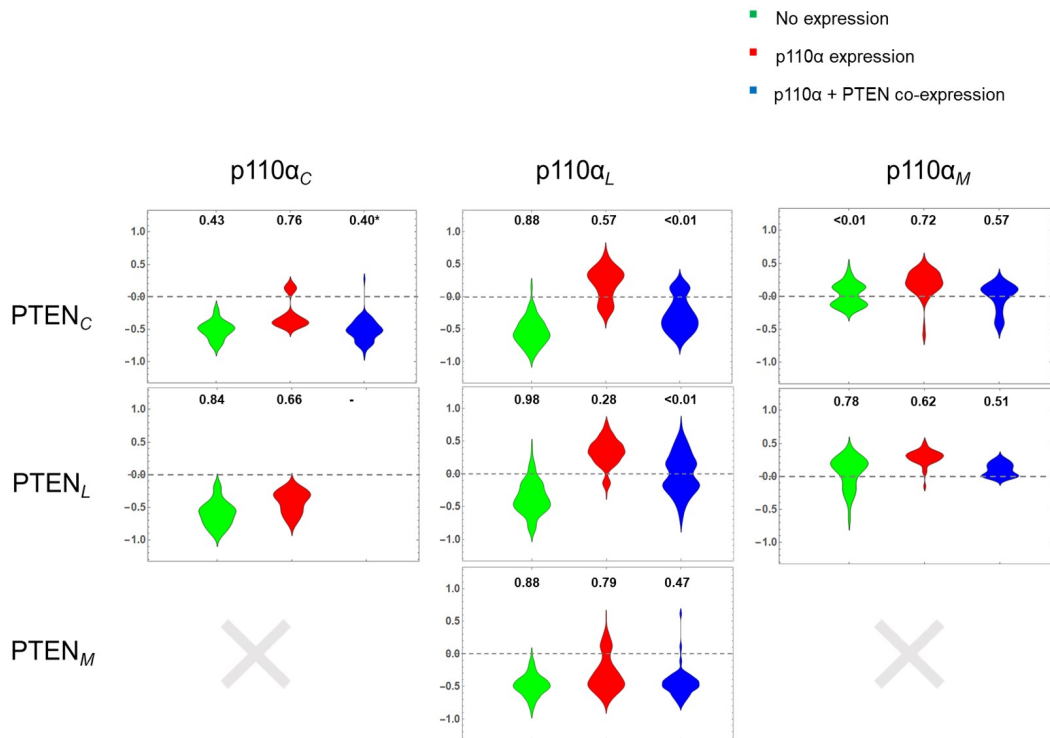


Figure 5.1: Assessment of bimodality across different constructs. Significance of bimodality was determined using Hartigan diptest and p-values are represented here. Quantification was performed on 50-100 cells that were identified in each condition, across all the constructs. \*Quantification performed using user defined cells. Dotted line represents PIP $_3$  index equal to zero.

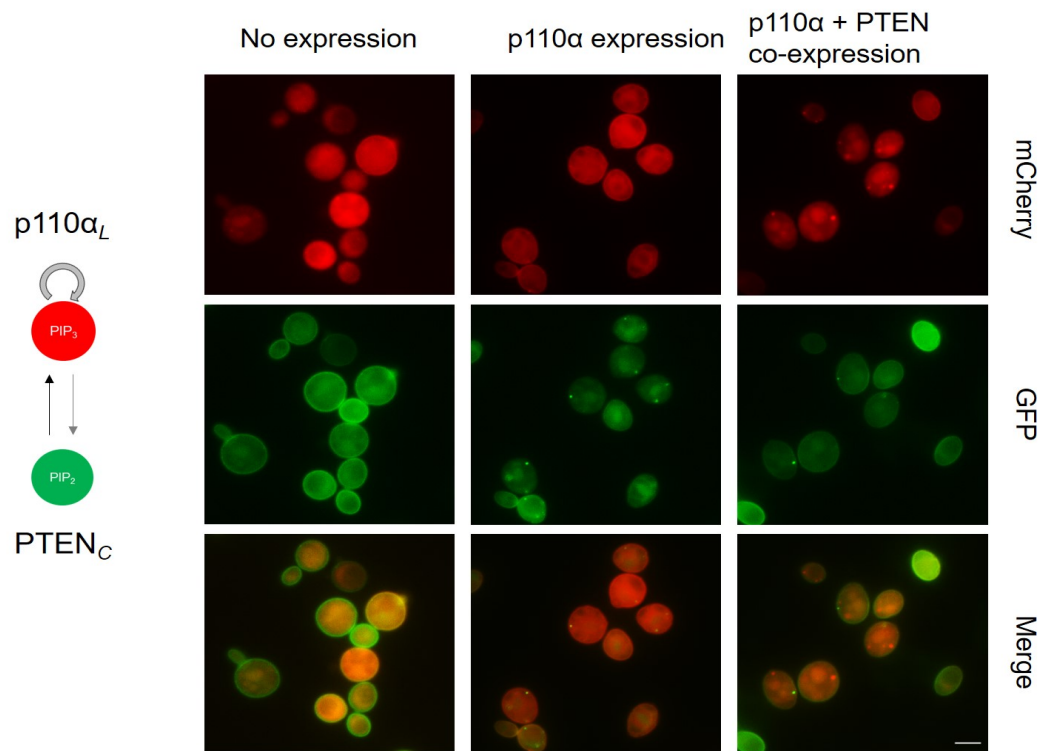


Figure 5.2: Representative images of cells showing large differences between conditions in the one-loop construct. Images of cells containing the one-loop construct (inset) were collected in both mCherry and GFP channels across uninduced, p110 $\alpha_L$  expression and p110 $\alpha_L$  and PTEN $_C$  co-expression. Scale bar = 5 $\mu$ m.

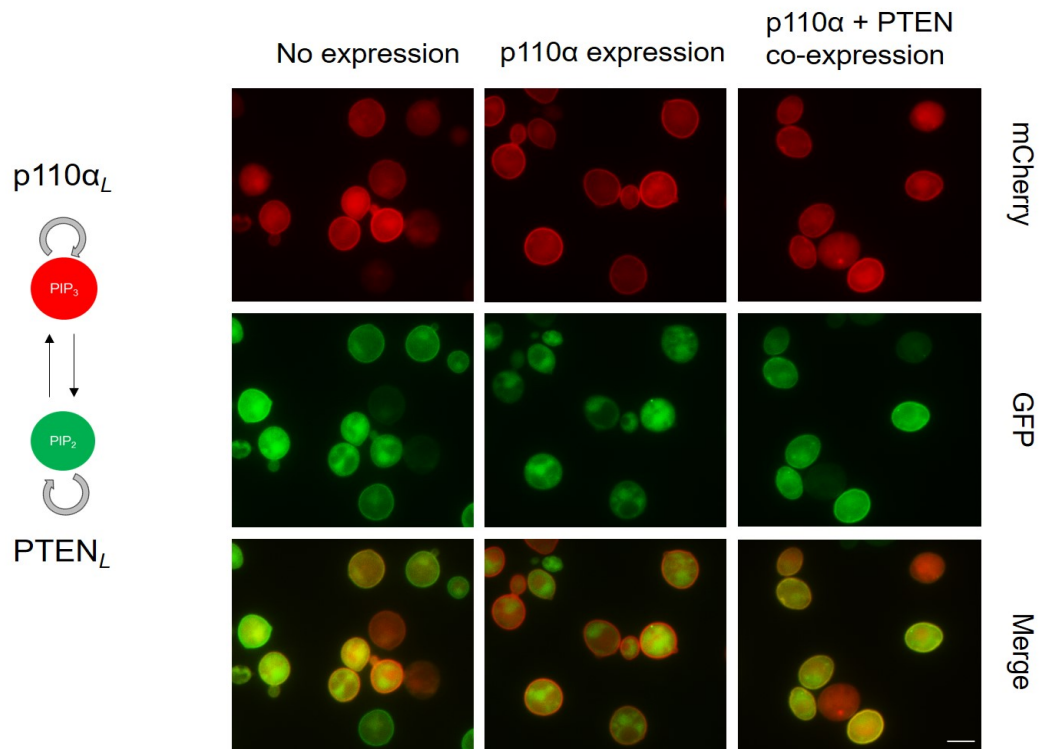


Figure 5.3: Representative images of cells showing bimodality in the two-loop that were induced to coexpress p110 $\alpha_L$  and PTEN $_L$ . Images of cells containing the two-loop construct (inset) were collected in both mCherry and GFP channels across uninduced, p110 $\alpha_L$  expression and p110 $\alpha_L$  and PTEN $_C$  co-expression. Scale bar = 5 $\mu$ m.

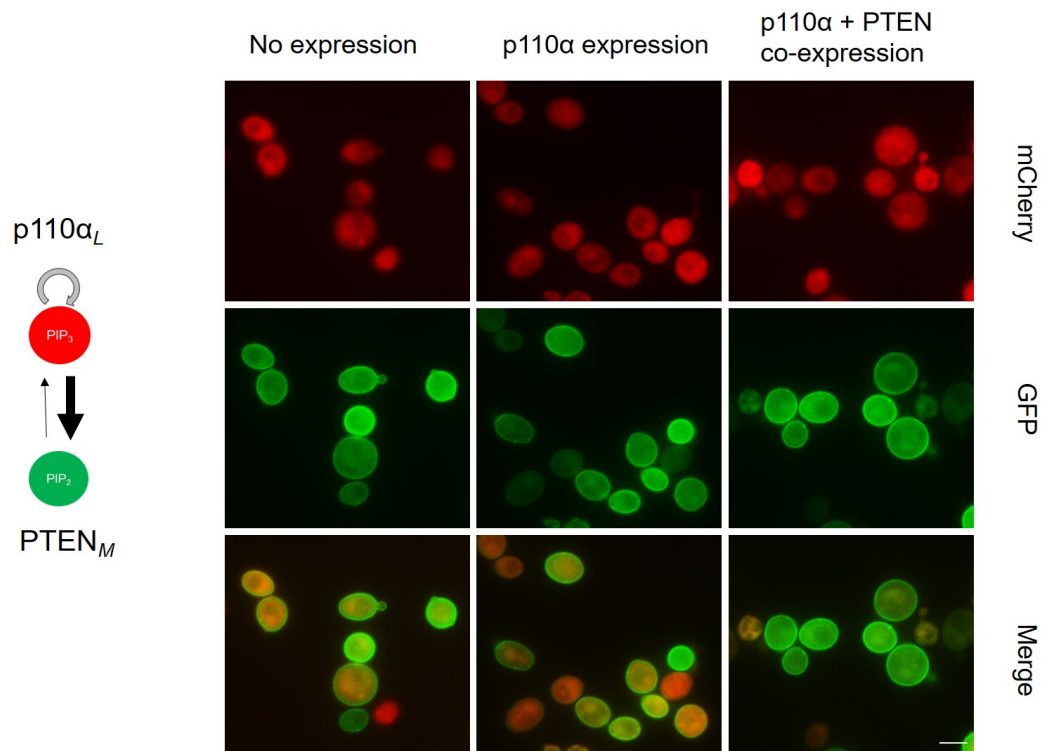


Figure 5.4: Representative images of cells showing little differences across all three conditions in cells containing p110 $\alpha_L$  and PTEN $_M$ . Images of cells containing the op110 $\alpha_L$  and PTEN $_M$  (inset) were collected in both mCherry and GFP channels across uninduced, p110 $\alpha_L$  expression and p110 $\alpha_L$  and PTEN $_C$  co-expression. Scale bar = 5 $\mu$ m.

### 5.3 The two-loop construct showed ability to behave based on PI(3,4,5)P<sub>3</sub> history

Next, to test the stability of the two populations in the bimodal distribution of the one-loop and two-loop constructs, hysteresis experiments were designed (Figure 5.5). Cells co-expressing p110 $\alpha$  and PTEN in the one-loop and two-loop constructs resulted in two peaks that were separated by *PIP*<sub>3</sub>- Index of zero. To test the stability of these populations, low and high levels of PI(3,4,5)P<sub>3</sub> was created, termed as initial conditions (Figure 5.5). Cells with high levels of PI(3,4,5)<sub>3</sub> were created by inducing p110 $\alpha_L$  expression and cells with low PI(3,4,5)P<sub>3</sub> were created without treatment with any inducer. The cells were then washed and induced to co-express p110 $\alpha_L$  and PTEN and the wash steps were found to remove any residual inducer that could affect PI(3,4,5)P<sub>3</sub> levels in the cell thus, confirming that the levels of PI(3,4,5)P<sub>3</sub> after perturbation were dependent on cell history (Figure 5.6). No signal was detected in cells that were not induced to co-express p110 $\alpha$  and PTEN. Cells that started at high levels of PI(3,4,5)P<sub>3</sub> in the cell are referred to as experienced cells, as these cells have previously experienced PI(3,4,5)P<sub>3</sub> at the plasma membrane and cells that started at low levels of PI(3,4,5)P<sub>3</sub> are referred to as naïve cells, as these cells have no experience of PI(3,4,5)P<sub>3</sub> at the plasma membrane.

The two-loop construct showed the ability to store information on cellular history as experienced cells maintained high levels of PI(3,4,5)P<sub>3</sub> after co-expression of p110 $\alpha_L$  and PTEN<sub>L</sub>. In the two-loop construct, naïve cells showed a mixture of cells, which showed strong mCherry or GFP signal at the plasma membrane in the population (Figure 5.7). In contrast, experienced cells showed strong mCherry signal at the plasma membrane across all cells in the population (Figure 5.7). Quantification of the two-loop construct confirmed that the naïve cells were bimodal after co-expression of p110 $\alpha_L$  and PTEN<sub>L</sub> in the ED- condition whereas, experienced cells maintained high levels of PI(3,4,5)P<sub>3</sub> and showed a more unimodal distribution (Figure 5.8). The one- loop construct did not show the ability to retain information at the plasma membrane as both experienced and naïve cells showed a mixture of cells, which showed strong mCherry or GFP signal at the plasma membrane in the

population (Figure 5.10). Quantification of cells also showed bimodal distribution across both naïve and experienced cells.

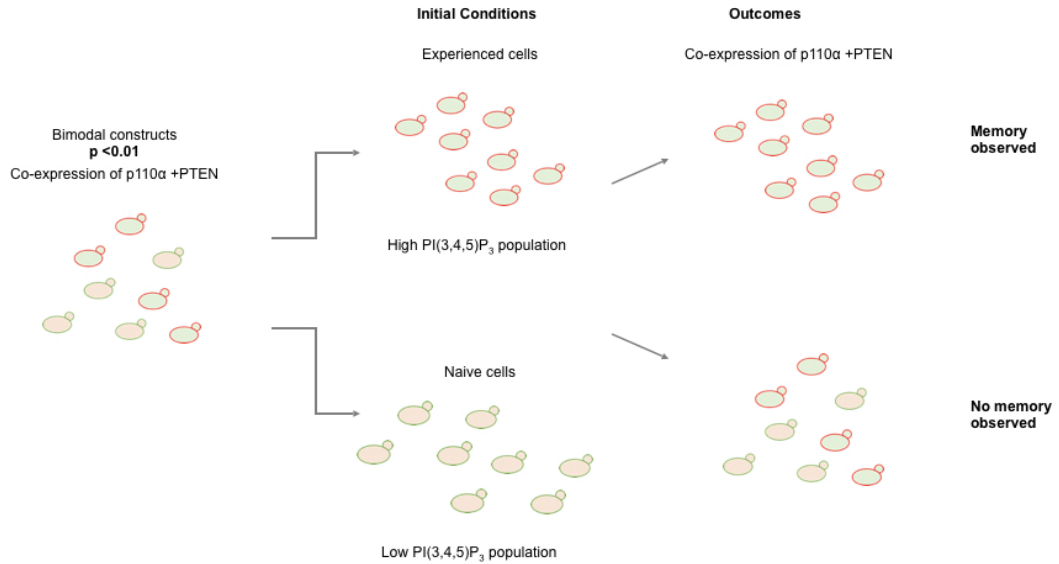


Figure 5.5: Experimental set-up to test memory in one-loop and two-loop constructs. Cells were grown in high-PI(3,4,5)P<sub>3</sub> (experienced cells) and low PI(3,4,5)P<sub>3</sub> (naïve cells) conditions and inoculated in fresh media for induction of p110α and PTEN coexpression (ED- condition). The outcomes of co-expression was measured as experienced cells that showed memory displayed high levels of PI(3,4,5)P<sub>3</sub> at the plasma membrane and naïve cells maintained bimodality.

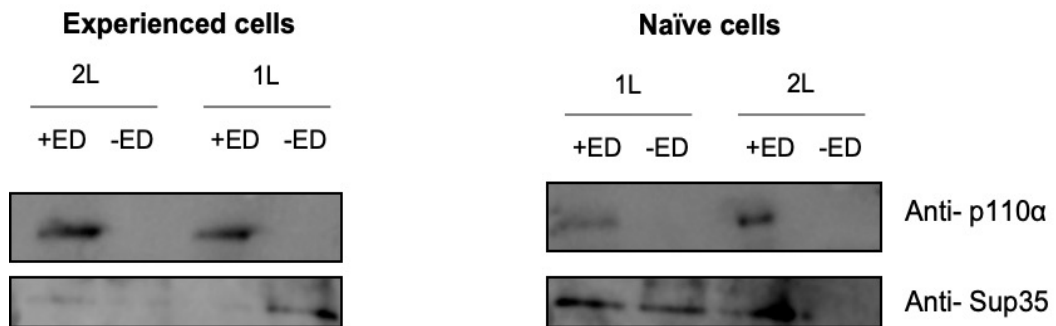


Figure 5.6: Immunoblot showing that that growth conditions for experienced cells did not interfere with memory test. Expression of p110α was only detected in cells induced to co-express p110α<sub>L</sub> and PTEN<sub>C</sub> (1L) or p110α<sub>L</sub> and PTEN<sub>L</sub> (2L), which confirmed that induction from initial conditions was removed to test, which was used to co-express p110α<sub>L</sub> and PTEN versions, for the presence of memory. Immunoblotting for Sup35 was used as a loading control. As the amount of protein loaded was adjusted to 20μg, the faint signal observed in experienced cells were associated to low antibody concentration used.

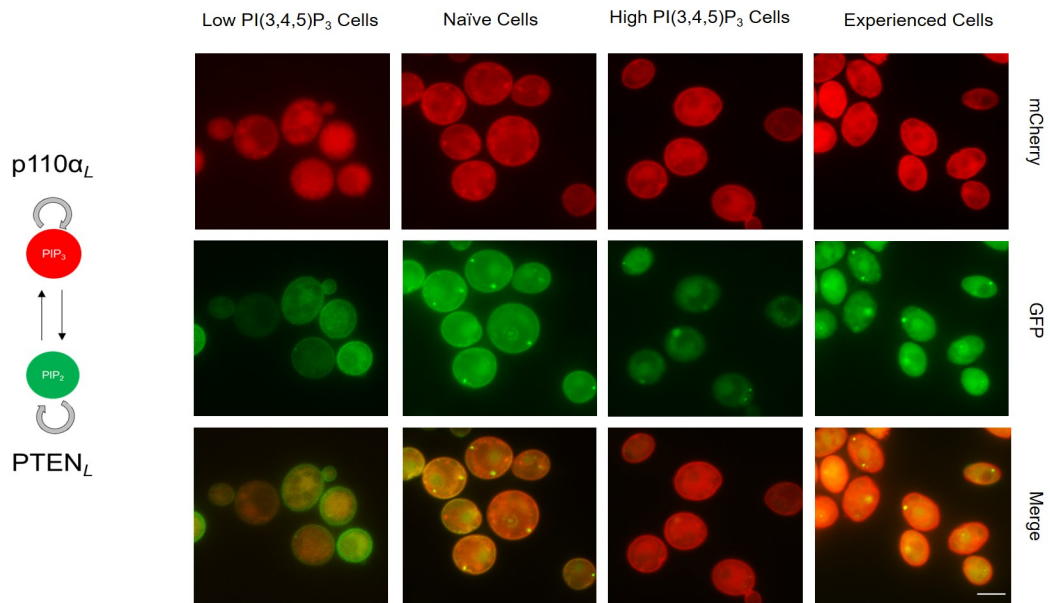


Figure 5.7: Two-loop construct showed ability to retain information about PI(3,4,5)P<sub>3</sub> history. Initial conditions of low and high levels of PI(3,4,5)P<sub>3</sub> were created in cells by treating cells with no inducer and fully induced expression of p110α<sub>L</sub>. High PI(3,4,5)P<sub>3</sub> cell populations that were induced to co-express p110α<sub>L</sub> and PTEN<sub>L</sub> are called experienced cells and low (3,4,5)P<sub>3</sub> cells the co-expressed p110α<sub>L</sub> and PTEN<sub>L</sub> are called naïve cells. Scale bar = 5μm.

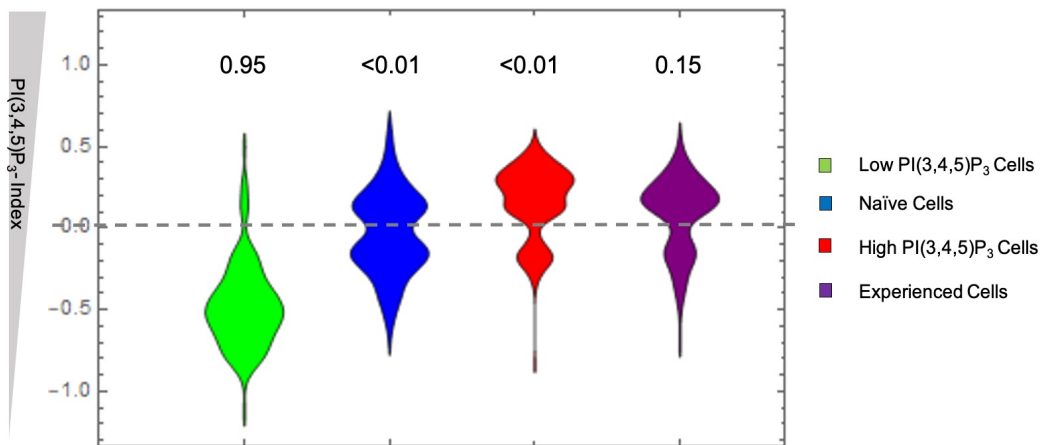


Figure 5.8: Distribution plots of two-loop cells across initial and hysteresis conditions. Quantification of 200- 300 cells across each condition of the two-loop cells was performed. Dotted line separates distributions associated with low and high PIP<sub>3</sub>-Indexes as it marks PIP<sub>3</sub>-Index = zero. Values at the top represent significance of bimodality as calculated by Hartigan diptest.

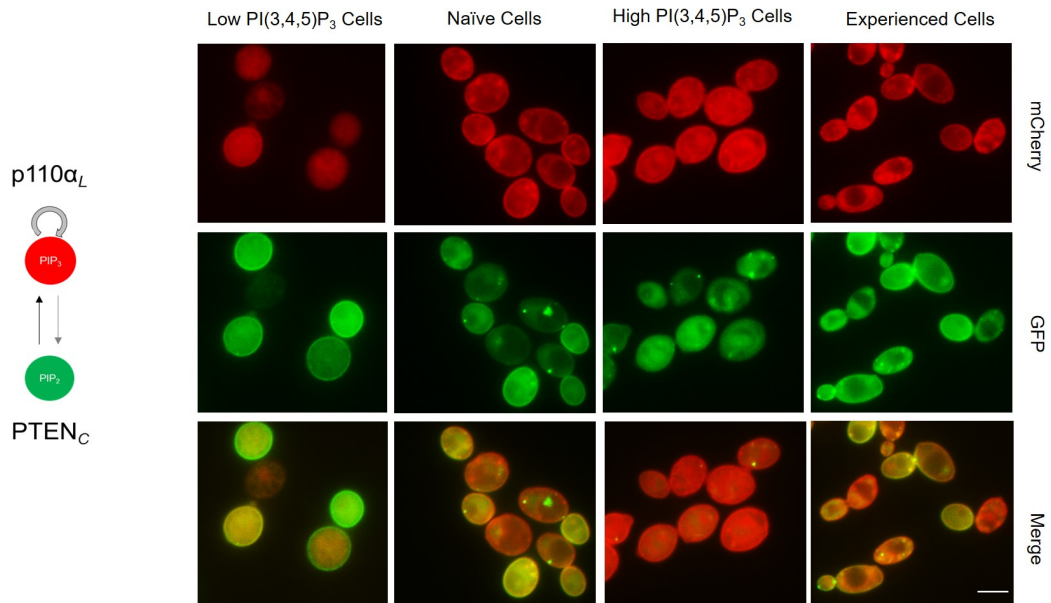


Figure 5.9: Representative images of hysteresis experiment using one-loop construct. Cells were observed at initial conditions of low and high  $PI(3,4,5)P_3$  levels. Cells that had low and high  $PI(3,4,5)P_3$  levels were induced to co-express  $p110\alpha_L$  and  $PTEN_C$  and are referred to as Naïve and experienced cells, respectively. Scale bar =  $5\mu m$ .

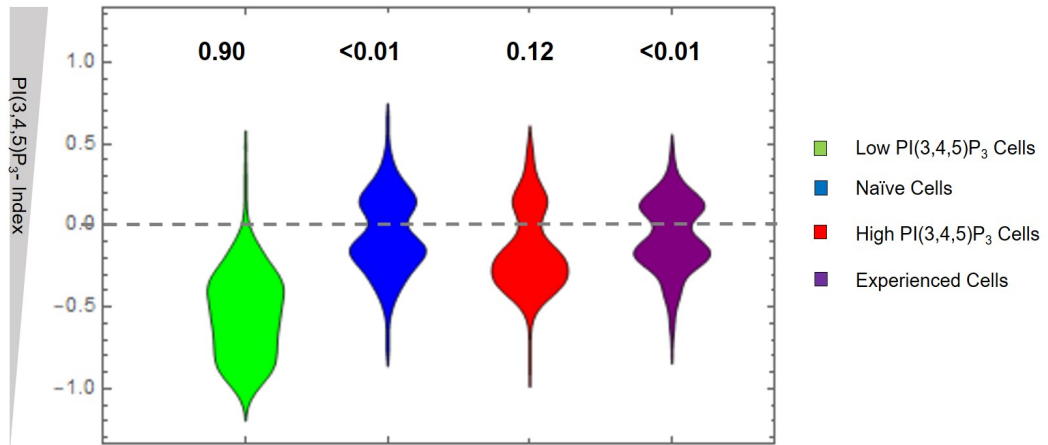


Figure 5.10: Distribution plots of one-loop construct across initial and hysteresis condition. Initial conditions of cells were generated by inducing cells to possess low and high levels of  $PI(3,4,5)P_3$ . Low and high levels of  $PI(3,4,5)P_3$  cells were induced to co-express  $p110\alpha_L$  and  $PTEN_C$  and were referred to as naïve and experienced cells. The quantification across each condition was performed on 200- 300 cells that were identified using the machine-learning based algorithm. Dotted line separates distributions associated with low and high  $PIP_3$ - Indexes as it marks  $PIP_3$ -Index = zero and values represented at the top show significance of bimodality.

## 5.4 Bimodality was observed across a larger concentration range in the two-loop construct

As the two-loop construct resulted in the cells that behaved based on the previous history of the cell population, which was not observed in the one-loop construct, low and high PI(3,4,5)P<sub>3</sub> levels were generated and induced with a concentration gradient of  $\beta$ -estradiol. There were significant differences observed between the response in experienced and naïve cells, in both the one-loop and the two-loop constructs. In the one-loop construct, significant bimodal distribution was observed at higher concentrations ranges of  $\beta$ -estradiol, which was not observed in experienced cells (Figure 5.13). Quantification of differences between naïve and experienced cells in the two-loop construct showed that bimodality was more significant across both responses to  $\beta$ -estradiol, at leaky expression of PTEN<sub>L</sub>. Moreover, naïve cells in the two-loop construct showed significant bimodality at concentrations between 0.75nM and 25nM of  $\beta$ -estradiol; whereas, experienced cells showed significant bimodality between 1.5nM and 6.25nM of  $\beta$ -estradiol. Therefore, bimodal distribution in the two-loop construct was more significant in naïve cells than in experienced cells, which was also observed in the one-loop construct.

## 5.5 The two-loop construct shows robust response even under leaky expression of PTEN<sub>L</sub>

The two-loop construct showed a higher maximum response than the one-loop construct. To further understand the differences between responses to  $\beta$ -estradiol gradient, the percentage of cells with *PIP*<sub>3</sub>-Index > zero was determined across each concentration. Across both one-loop and two-loop constructs, naïve cells showed greater response than experienced cells. In the one-loop construct, 50% response was observed in naïve cells induced with 12.5nM  $\beta$ -estradiol and at this concentration experienced cells showed 20% response (Figure 5.14). At concentrations higher than 12.5nM, the response observed of the naïve cells was found to plateau at 52%, which was also the maximum response observed in these cells. The response observed in

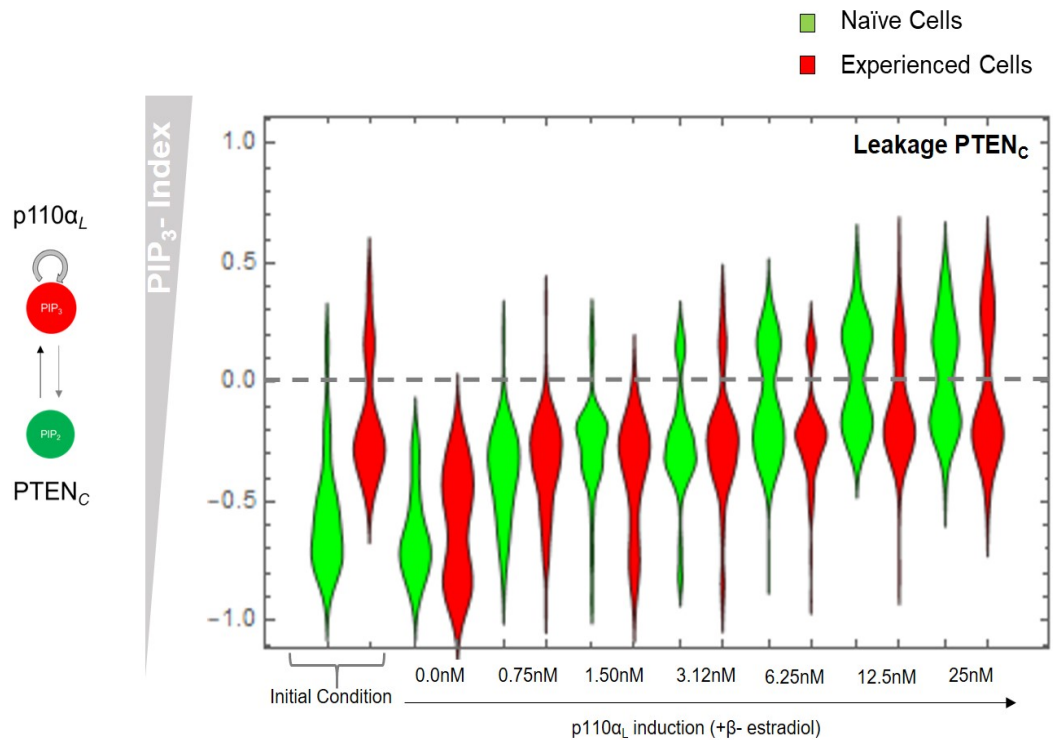


Figure 5.11: Effect of  $\beta$ -estradiol concentration and leaky expression of  $PTEN_C$  on the significance of bimodality in cell response across naïve and experienced cells. Quantification of initial conditions (low and high  $PI(3,4,5)P_3$  containing cells) and response to  $\beta$ -estradiol concentration gradient was performed across 150-200 cells in each condition. The dotted line represents distributions with  $PIP_3$ - Index at zero, which is the result of equal amounts of mCherry and GFP at the plasma membrane.

experienced cells showed a maximum response at 35%, which was significantly lower than the maximum response reached in the naïve cells. In comparison, the two-loop construct reached 50% response at lower concentrations across both naïve and experienced cell (Figure 5.7). Naïve and experienced cells reached 50% response at 3nM and 4nM of  $\beta$ -estradiol treatment, respectively. At concentrations higher than 5nM of  $\beta$ -estradiol, cells continued to increase in response as experienced cells reached a maximum response of 80% at 25nM of  $\beta$ -estradiol and naïve cells reached a maximum response of 80% at 12.5nM of  $\beta$ -estradiol. In naïve cells a 5% decrease in response was observed at 25nM of  $\beta$ -estradiol. Therefore, the response in the two-loop system showed less difference between responses in naïve and experienced cells compared to the one-loop system, as well as showing higher responses across both conditions compared to the one-loop construct.

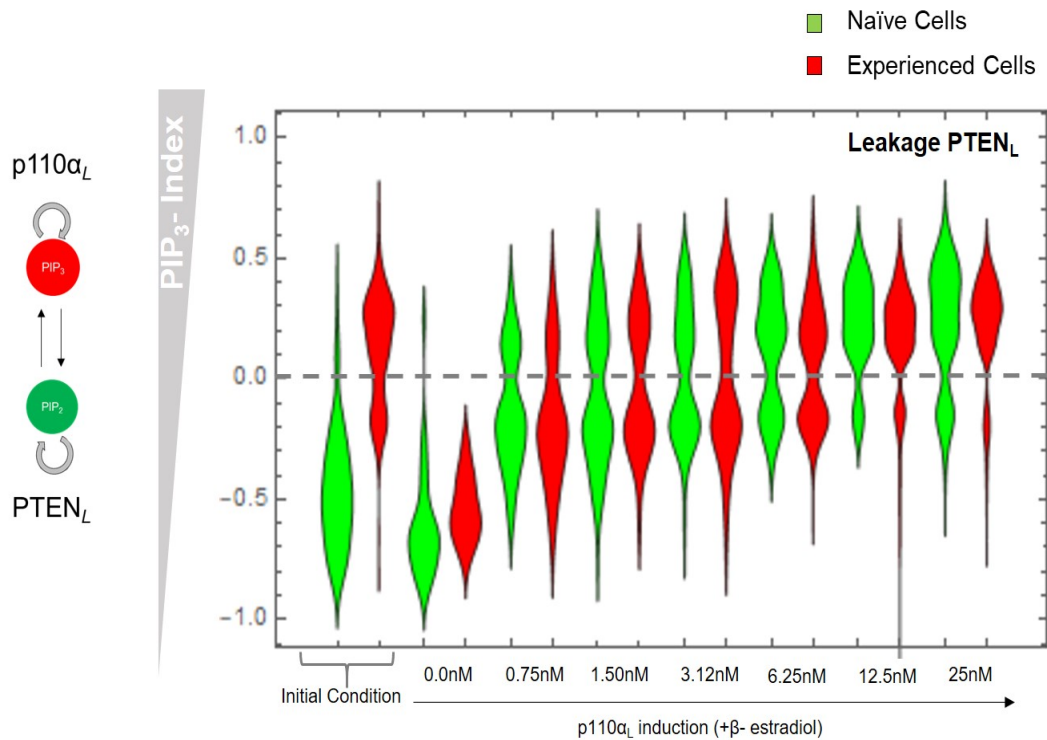


Figure 5.12: Effect of  $\beta$ -estradiol concentration and leaky expression of PTEN<sub>L</sub> on the significance of bimodality in cell response across naïve and experienced cells. Quantification of initial conditions (low and high PI(3,4,5)P<sub>3</sub> containing cells) and response to  $\beta$ -estradiol concentration gradient was performed across 150-200 cells in each condition. The dotted line represents distributions with PIP<sub>3</sub>- Index at zero, which is the result of equal amounts of mCherry and GFP at the plasma membrane.

## 5.6 Expression of PTEN<sub>L</sub> is required for bistable response in two-loop construct

Co-expression of PTEN<sub>L</sub> at high levels resulted in bimodality across response to concentration gradient of p110 $\alpha_L$  induction. Bimodality was not observed across response to  $\beta$ -estradiol in naïve and experienced cells that expressed high levels of PTEN<sub>L</sub> in the cell (Figure 5.17). Here, the response was found to be associated with low PIP<sub>3</sub>- Indexes between the concentration ranges of 0- 3.12nM and high at concentration ranges between 6.25-12.5nM. In contrast, at low levels of PTEN<sub>L</sub> expression, bimodality was observed across all of the experienced cells and at 6.25-12.5nM concentration range of  $\beta$ -estradiol in naïve cells (Figure 5.16). These results suggest that expression of PTEN<sub>L</sub> at high levels results in the transition of the bimodal population to become unimodal, which describes bistability.

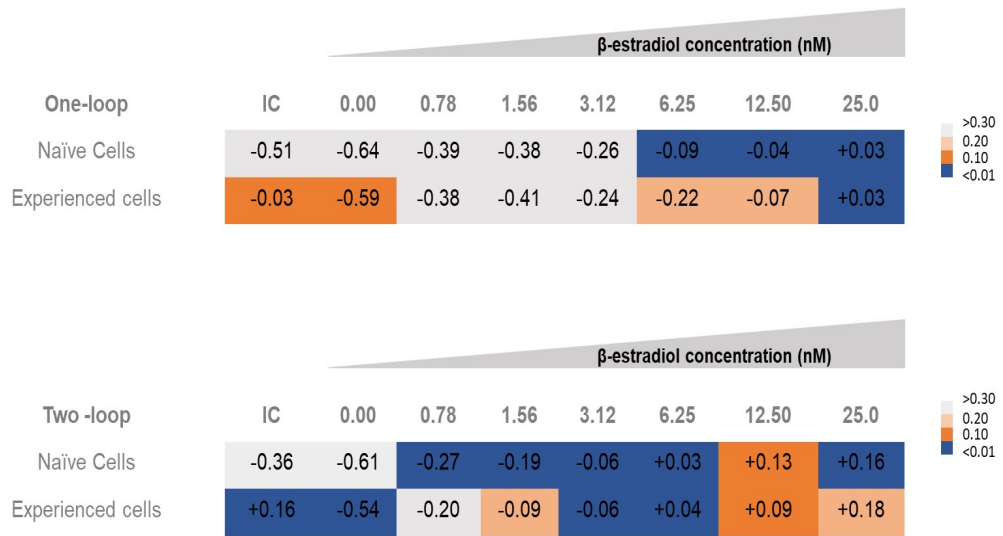


Figure 5.13: Significance of bimodality across distribution plots between experienced and naïve cell history in one-loop and two-loop constructs. IC represents the initial conditions at low and high  $PI(3,4,5)P_3$  of the cells and the mean across the cell population is represented here along with significance of bimodality as calculated by Hartigan diptest ( $p < 0.3$ ). Distributions with high and low significance are represented in blue and grey, respectively.

## 5.7 Expression of $PTEN_L$ at high levels resulted in hysteresis in the two-loop construct

The expression of  $PTEN_L$  at high levels was able to force the system into low or high  $PI(3,4,5)P_3$  states based on the history of the cell. The response to  $\beta$ -estradiol induction was compared between naïve and experienced cells at low and high expression levels of  $PTEN_L$ . The response i.e., percentage of cells  $PIP_3$ -Indexes  $> 0$  in response to  $\beta$ -estradiol concentration, was plotted across both naïve and experienced cells at low and high levels of  $PTEN_L$  induction (Figure 5.18 and 5.19). At low  $PTEN_L$  induction, naïve cells showed a higher response than experienced cells. Naïve cells showed 50% response at 2nM induction and experienced cells showed response at 4nM of  $\beta$ -estradiol induction (Figure 5.18). These results were similar to the response observed at leaky  $PTEN_L$  expression, where naïve cells and experienced cells respectively showed 50% response at 3 and 4nM  $\beta$ -estradiol induction (Figure 5.15), suggested that low expression levels of  $PTEN_L$  was unable to switch cells into low or high  $PI(3,4,5)P_3$  levels based on initial conditions in the cell. On the other hand, high expression levels of  $PTEN_L$  showed increased  $PIP_3$ -Indexes associated with

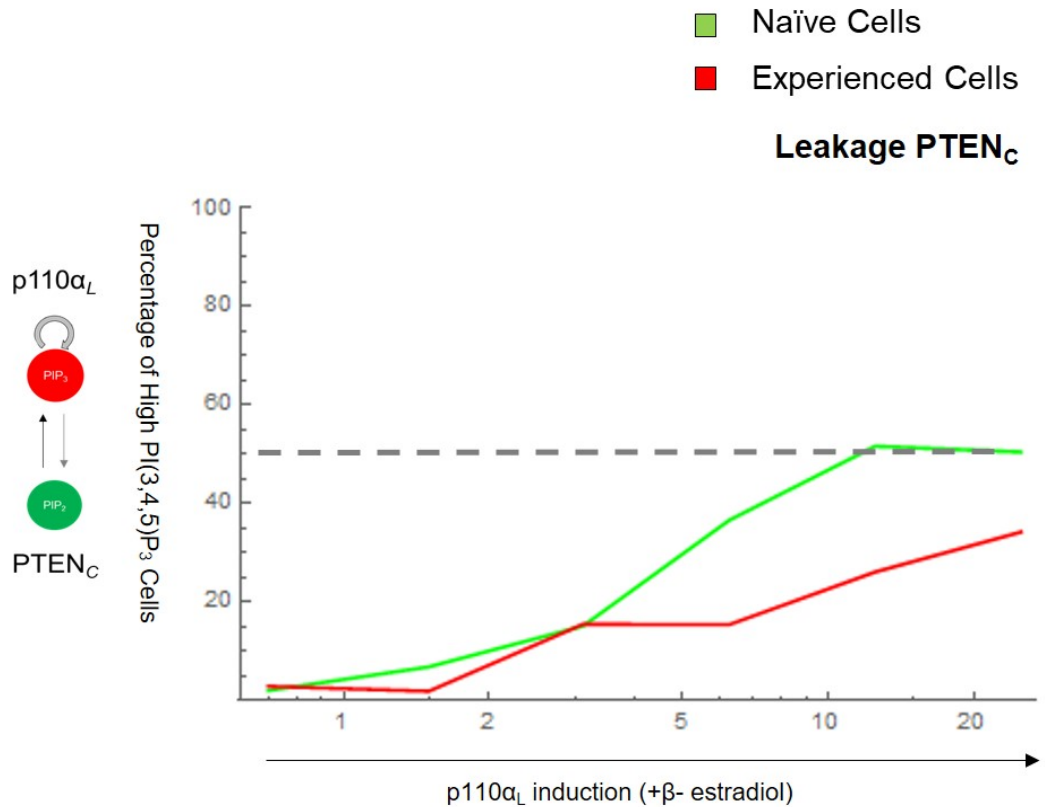


Figure 5.14: Response to  $\beta$ -estradiol concentration gradient in one-loop cells, at leaky expression of PTEN<sub>C</sub>. Cells with low (naïve) and high (experienced) levels of PI(3,4,5)P<sub>3</sub> were treated with a concentration range of 0-25nM of  $\beta$ -estradiol. The response shown here is defined as the percentage of cells with  $PIP_3$ -Index > 0 in the quantified population. Dotted line represents response of 50% across the quantified population.

cells experienced cells compared to naïve cells as cells reached 50% response at 3.5 and 4.5nM of  $\beta$ -estradiol induction, respectively. The difference in  $PIP_3$ -Index was greater at higher levels of p110 $\alpha_L$  induction as the maximum difference between response in experienced and naïve cells was found to be 25% at 6.25nM of  $\beta$ -estradiol induction. Therefore, higher levels of PTEN<sub>L</sub> expression were required for switching the system between low and high levels of PI(3,4,5)P<sub>3</sub> based on the initial conditions of the cells, which was consistent with the memory that was observed in the two-loop cells that were induced to fully express p110 $\alpha_L$  and PTEN<sub>L</sub>.

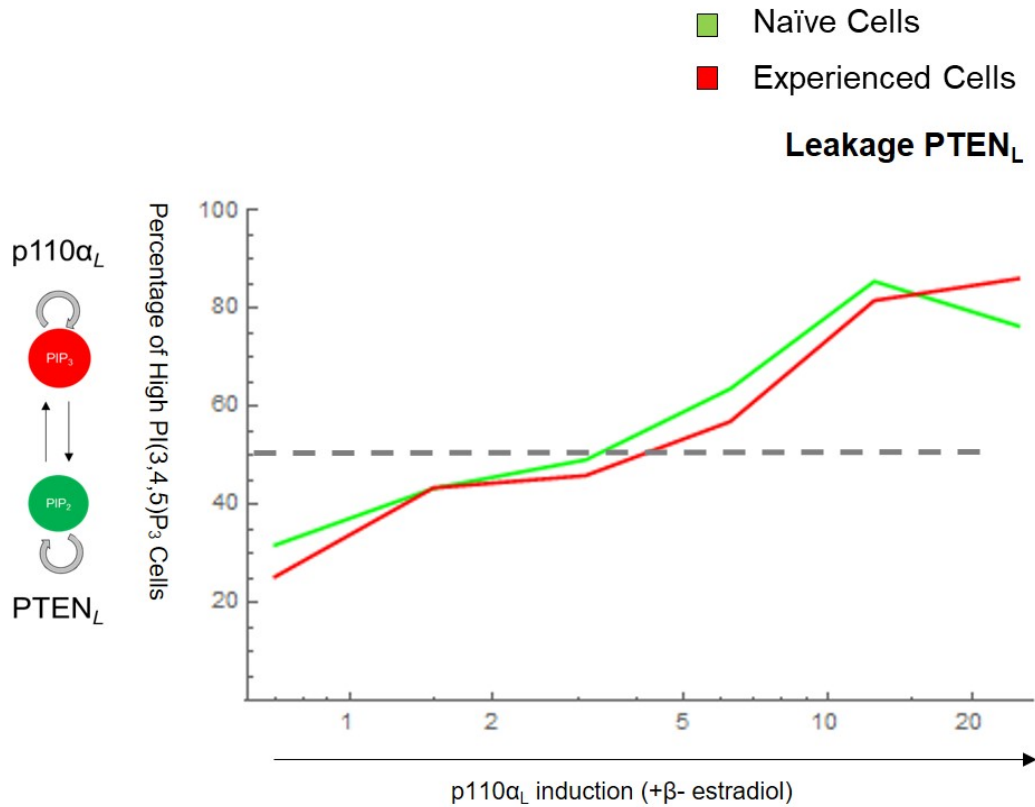


Figure 5.15: Response to  $\beta$ -estradiol concentration gradient in two-loop cells, at leaky expression of  $PTEN_L$ . Cells with low (naïve) and high (experienced) levels of  $PI(3,4,5)P_3$  were treated with a concentration range of 0-25nM of  $\beta$ -estradiol. The response shown here is defined as the percentage of cells with  $PIP_3$ -Index > 0 in the quantified population. Dotted line represents response of 50% across the quantified population.

## 5.8 Discussion for understanding bistability at the plasma membrane

In this chapter, bimodality was observed in cells that expressed  $p110\alpha_L$  and  $PTEN_{C/L}$  in the two-loop and one-loop constructs (Figure 5.1). The significance of bimodality was measured using Hartigan diptest, which tests whether the distribution is unimodal against a multimodal alternative [48]. Other tests that are available to study significance of bimodality include bimodality co-efficient and Akaike's information criterion. However, Hartigan diptest has been shown to be more robust in measuring of bimodality as it is not affected by skewness of the data and also shows highest sensitivity in distinguishing bimodality from unimodality [38]. For these reasons,

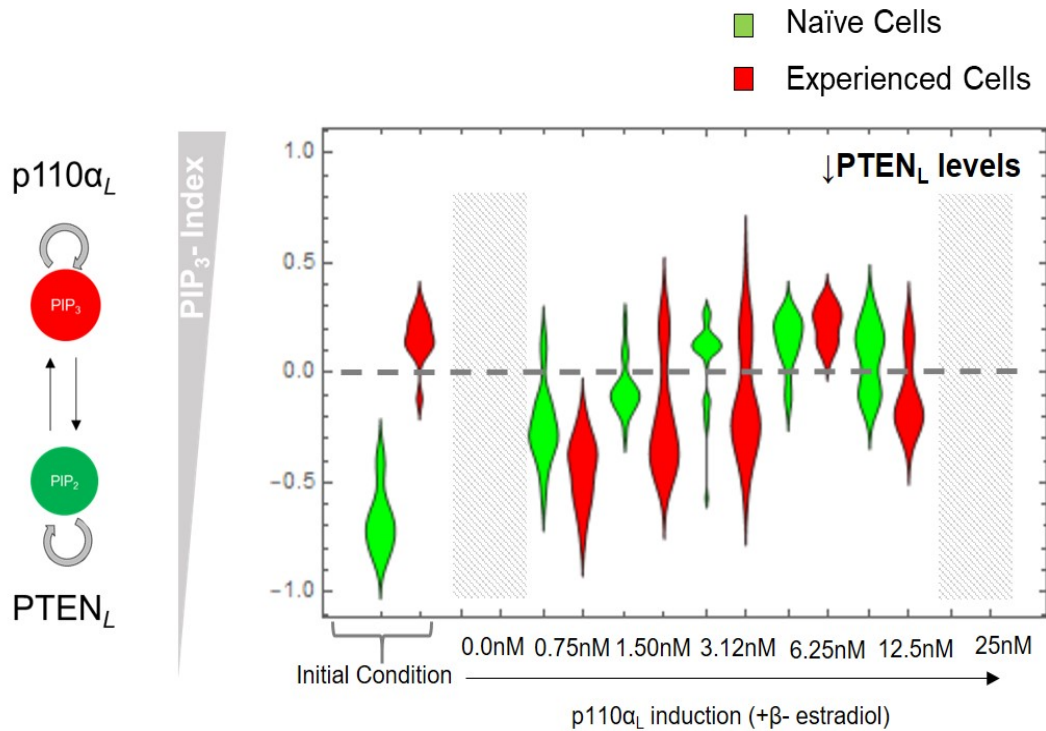


Figure 5.16: Effect of low induction of  $PTEN_L$  expression on bimodality in response to concentration gradient of  $\beta$ -estradiol in naïve and experienced two-loop cells. Low expression of  $PTEN_L$  was fixed across the cells using  $5\mu M$  of doxycyclin. The distribution plots of  $PIP_3$ - Index of 30-50 cells in each condition are shown here. Data for concentrations at 0nM and 25nM were not collected (grey boxes) and the dotted like represents  $PIP_3$ - Index = 0.

the Hartigan diptest has been used to test significance of bimodality to describe cell-to-cell variability between populations [80, 9]. Some studies argue that since the Hartigan diptest does not fit a Gaussian distribution, it does not contain the statistical power to accurately detect peaks in the distribution that maybe observed in typical biological situations [32]. However, since peaks observed in the bimodal  $PIP_3$  -Index distribution in this study were separated by zero, Hartigan diptest was a convenient way to measure significance of bimodality in this study.

Comparison between the one-loop and two-loop constructs confirm that an outcome of bistability is bimodality but the reverse does not hold true in this system. The one-loop construct is made up of  $p110\alpha_L$  and  $PTEN_C$ , where the co-expression of both enzymes resulted in bimodal distribution in the cell (Figure 5.1). To test the stability of the two populations in the cell, hysteresis experiments were performed as described above (Figure 5.5). Full induction of  $p110\alpha_L$  and  $PTEN_C$

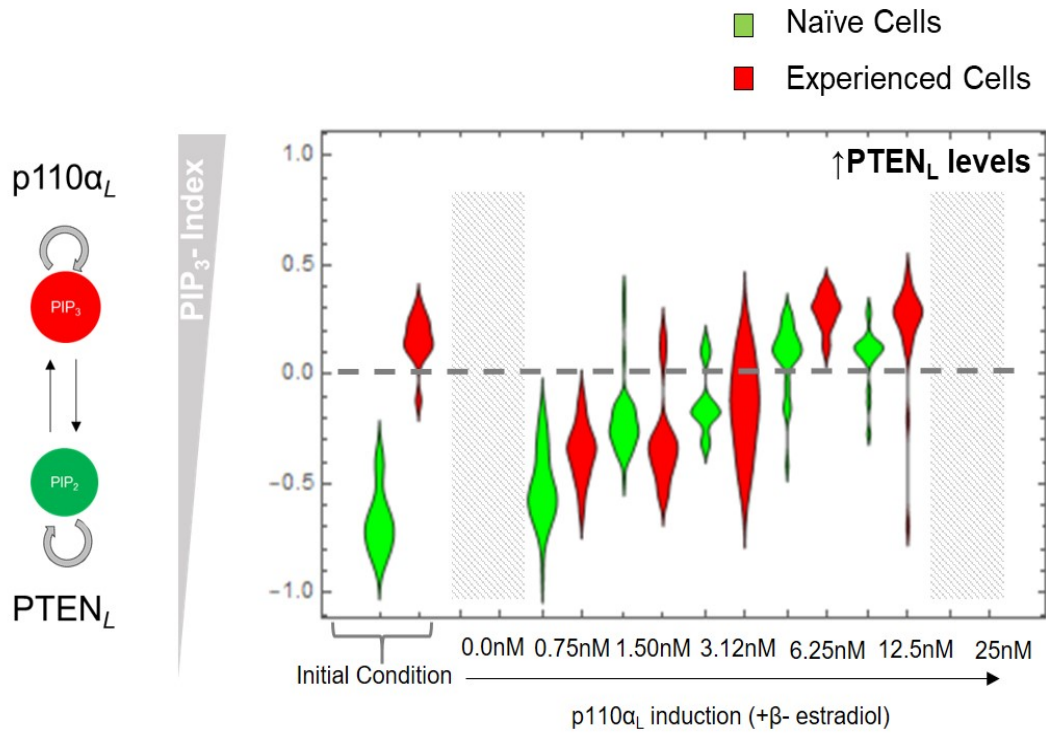


Figure 5.17: Effect of high induction of PTEN<sub>L</sub> expression on bimodality in response to concentration gradient of  $\beta$ -estradiol in naïve and experienced two-loop cells. High expression of PTEN<sub>L</sub> was fixed across the cells using 55 $\mu$ M of doxycyclin. The distribution plots of PIP<sub>3</sub>-Index of 30-50 cells in each condition are shown here. Data for concentrations at 0nM and 25nM were not collected (grey boxes) and the dotted like represents PIP<sub>3</sub>-Index = 0.

resulted in bimodal distribution across both naïve and experienced cells, suggesting that although the cell population was bimodal, there was no bistability in this construct. Other studies also suggest that bimodality is not sufficient for bistability as non-uniformity in inhibitor concentration can result in cells can result in bimodal distribution across the population [89]. This may well be the case as to why bistability was not observed in the one-loop construct as diffusion of PTEN<sub>C</sub> may have resulted in a heterogeneous distribution within the cell resulting in low PIP<sub>3</sub>-Indexes which was observed even in cells that were induced to maintain high levels of PI(3,4,5)P<sub>3</sub>. The heterogeneous distribution within population is thought to be due to the high copy number PTEN<sub>C</sub> that is high in concentration and is able to dephosphorylate PI(3,4,5)P<sub>3</sub> faster than the low copy number p110 $\alpha_L$  in the cell.

Cells with the two-loop construct were found to show bistability and hysteresis

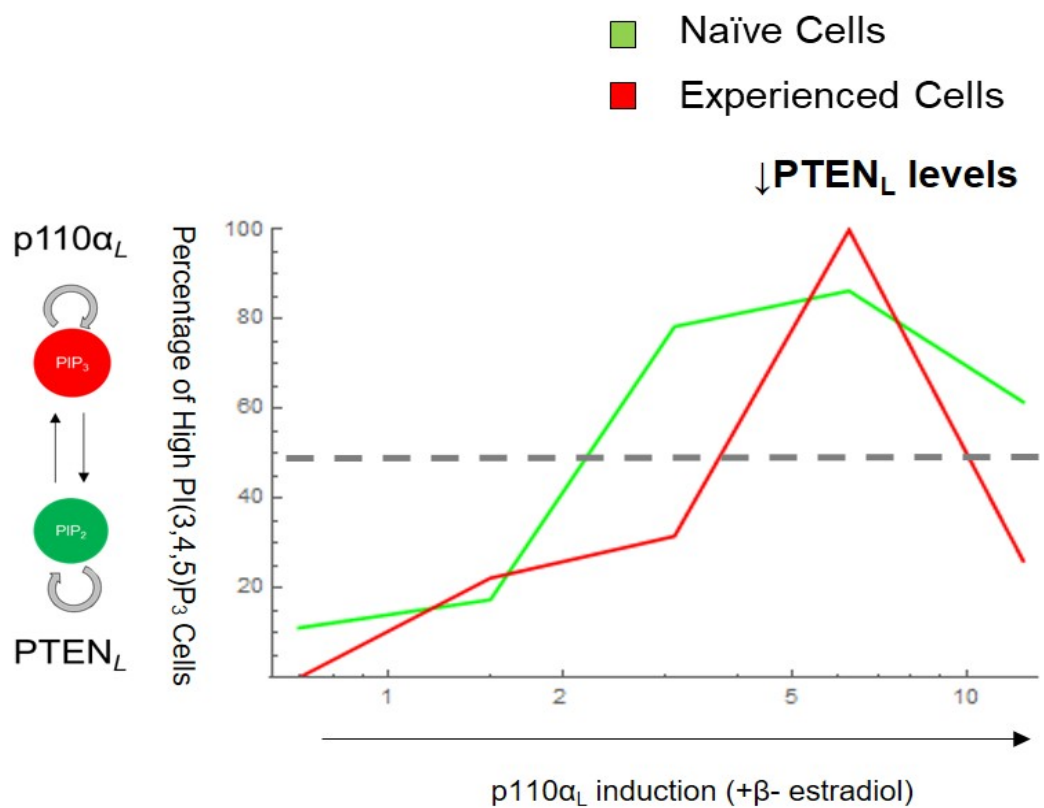


Figure 5.18: Comparison of two-loop naïve and experienced cell response to  $\beta$ -estradiol concentration at low PTEN<sub>L</sub> expression. Cells at initial conditions of low and high levels of PI(3,4,5)P<sub>2</sub> with fixed expression at low PTEN<sub>L</sub> were subjected to a concentration gradient of  $\beta$ -estradiol. Response of naïve and experienced cells is shown here. The dotted line indicates 50% cell response as a result of bimodal distribution.

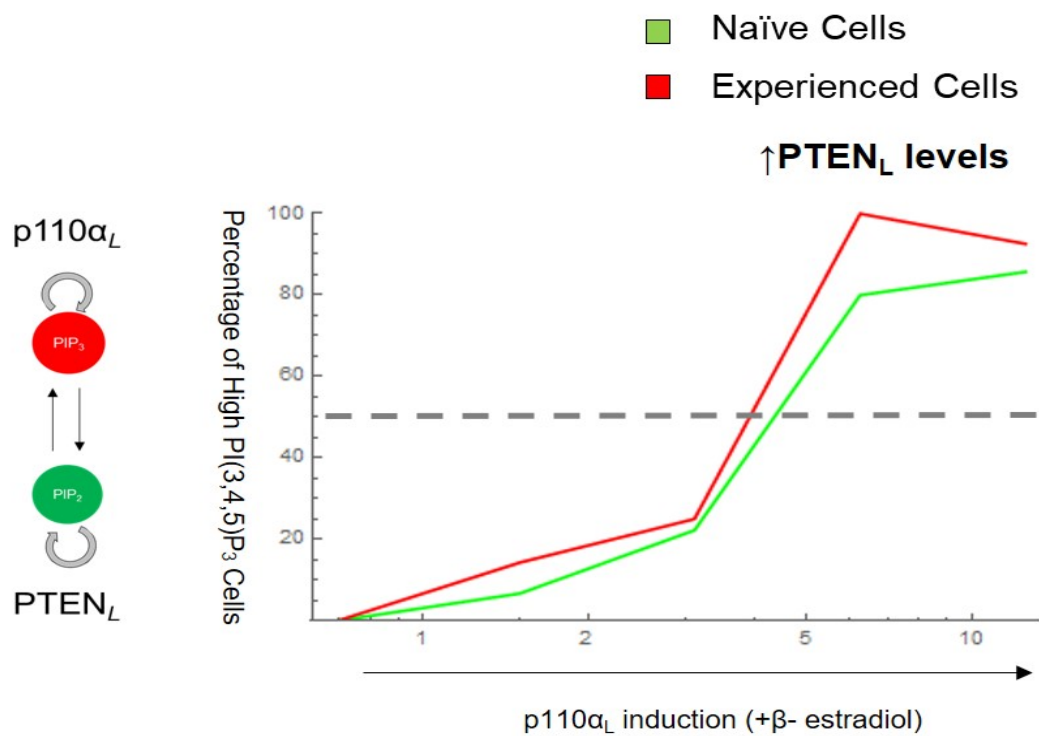


Figure 5.19: Comparison of two-loop naïve and experienced cell response to  $\beta$ -estradiol concentration at high levels of  $PTEN_L$ . Memory observed in cells expressing high levels of  $PTEN_L$ . Cells at initial conditions of low and high levels of  $PI(3,4,5)P_2$  with fixed expression at high  $PTEN_L$  were subjected to a concentration gradient of  $\beta$ -estradiol. Response of naïve and experienced cells is shown here. The dotted line indicates 50% cell response as a result of bimodal distribution.

based on previous PI(3,4,5)P<sub>3</sub> history in the cell, which was not observed in one-loop construct. Naïve cells showed low PI(3,4,5)P<sub>3</sub> levels after co-expression of PTEN<sub>L</sub> and p110α<sub>L</sub> whereas, experienced cells showed high PI(3,4,5)P<sub>3</sub> levels even after co-expression of PTEN<sub>L</sub> and p110α<sub>L</sub>. These results were consistent with previously published results of bistability [69]. Hysteresis was observed across the two-loop construct between naïve and experienced cells in response to β-estradiol concentration gradient at a high PTEN<sub>L</sub> levels, which was not observed at low or leaky expression of PTEN<sub>L</sub>. These results suggest that the increase in PTEN<sub>L</sub> expression beyond some unknown concentration increases the non-linearity in the system which forces the system to exist in either high or low levels of PI(3,4,5)P<sub>3</sub> in the cell. This is consistent with previously published studies that suggest the source of bistability arises from positive feedback and coupling of multiple feedback mechanisms result in an increase in non-linearity, which increases irreversibility of the switch once forced into the high response steady state [16]. Experimentally up to five feedback components have been linked in understanding bistability and decision making in maturation of *Xenopus* oocyte maturation [104]. The minimum chemical feedback mechanism with observable bistability has been shown to consist of two components with positive feedback that interact either by mutual inhibition or mutual activation [102]. A single positive feedback loop is also capable of producing a bistable response provided that the rate of activation is faster than rate of degradation/ dilution in the cell, which is often observed in gene transcription regulators [5, 52]. In the synthetic system constructed in this study, the rate of activation is inherently slower than rate of dilution due to diffusion of the components to the membrane and thus, I show that bistability across the cell population can be generated by mutual inhibition between two positive feedback components at the plasma membrane of the cell.

## Chapter 6

# Discussion

### 6.1 Thesis summary

The role of positive feedback at cellular membranes has long been postulated to regulate several processes, ranging from cell-to-cell variability to enrichment of molecules at membranes that can result in cell division or cell death [107, 57]. The important relationship between positive feedback and bistability is well studied in transcription regulation of genes as bistability can result in switching behaviour in cells. Conditions for ultrasensitivity and hysteresis are relatively well understood in gene regulation, as regulators of natural or synthetic genes interact in the nucleus where diffusion distances are short and diffusion occurs in a homogenous system. Meanwhile, experimental evidence in understanding the role of positive feedback at cellular membranes remains elusive due to complexity involved and due to changes in the diffusion rates of molecules within the cell and at the membrane. The construction of a synthetic system that was used to test the role of a simple positive feedback and bistability at the plasma membrane.

### 6.2 The two-loop synthetic system is analogous to the toggle-switch hypothesis

In this study, there was no clear evidence of population bistability leading to the spatial bistability at the plasma membrane to result in polarisation. Spatial bista-

bility is used to describe the presence of two states across the cellular membrane, where one state is enriched with a specific molecular species and the other is not. The switch between the two states in the deterministic system is determined by some stimulus and can result in either cluster formation or polarisation at the membrane. One of the most well-studied examples of population bistability resulting in spatial bistability at the plasma membrane of cells includes positive feedback between MinCD/MinE system in *Escherichia coli*, which results in clear population bistability that can be observed as concentric circles across a lawn of cells grown in semi-solid media and polarisation of MinD at the plasma membrane [79]. Theoretical models, known as the MinDE-toggle-switch, suggest that a mutual inhibition between self-promoting MinD and MinE result in polarisation at the plasma membrane and the concentric patterns across the population [97]. In fact, emerging experimental evidence appears to hypothesise that the model that describes the mutual inhibition between two components that are regulated by positive feedback, known as the toggle-switch hypothesis, may underpin the switch between unpolarised and polarised states in the cell (Table 6.1). The hypothesis is based on the evidence that in the well-mixed systems, such as in gene transcription regulation, the toggle switch mechanism shows bistability and hysteresis [41]. Other well studied examples include the Lactose-metabolism switching in *E.coli* [60] and lysis-lysogeny switching in lambda bacteriophage [88].

One of the first attempts to use a synthetic system to indirectly study Cdc42-GTP polarisation showed that mutual inhibition between two positive feedback loops was required for polarisation [17]. In this study a toolkit was developed using the CRIB domain, which specifically binds to Cdc42-GTP. Using coarse-grain modelling, the study concluded that the mutual inhibition between the polarising molecule and an inhibitor, which themselves are regulated by positive feedback loops were able to produce pole-like structures in cells treated with Latrunculin A. The results reported were consistent with previously published data; mainly, that polarisation requires local activation of the polarising molecule and global inhibition on the molecule. The study also showed that if the concentration was too high, then polarisation was lost as the activating was found everywhere on the plasma

membrane. This suggests that maybe there was some bistability in the synthetic system but this was not further studied. It also remains unclear whether the probable bistability is due to the behaviour of endogenous polarising behaviour of Cdc42 that was used in the system, or the treatment of Latrunculin A, which is used to disrupt actin polymerisation in the cell. Therefore, the synthetic system constructed in this thesis allows studying polarisation in live cells in a manner that is independent of Latrunculin A treatment and endogenous Cdc42-GTP activity.

More recently, using pharmacological and genetic manipulation confirms that the mutual inhibition between two positive feedback loops is required for PI(3,4,5)P<sub>3</sub> polarisation in *Dictyostelium discoideum* [65]. In response to cAMP gradient, individual cells develop pseudopodium for directional movement against the gradient. During pseudopod formation, PI(3,4,5)P<sub>3</sub> is produced to recruit Ras-GTP which in turn recruits PI3K to increase levels of PI(3,4,5)P<sub>3</sub> at the plasma membrane. PTEN dephosphorylates PI(3,4,5)P<sub>3</sub> to restore levels of PI(4,5)P<sub>2</sub> at the plasma membrane since, PTEN binds to PI(4,5)P<sub>2</sub> it produces more PI(4,5)P<sub>2</sub> at the plasma membrane. In this study, endogenous PTEN was found to be inhibited by PI(3,4,5)P<sub>3</sub> production and cAMP which resulted in polarisation. Replacing the endogenous PTEN with human PTEN resulted in loss of bistability and no polarisation was observed at the plasma membrane. The loss of polarisation was hypothesised to be due to the absence of cognate binding site for PI(3,4,5)P<sub>3</sub> or cAMP. The study suggests that physical inhibition of PTEN in *D. discoideum* cells is required for polarisation of PI(3,4,5)P<sub>3</sub> in response to cAMP gradient. The synthetic system that was constructed in this thesis maybe used to validate the need for direct inhibition between PTEN and PI(3,4,5)P<sub>3</sub> molecules to give rise to polarisation. Compared, to the system constructed in this thesis, which is dependent on the indirect mutual inhibition between PI(3,4,5)P<sub>3</sub> and PTEN, the synthetic system can also be used to test the hypothesis that the direct mutual inhibition between the two species can result in polarisation.

The co-expression of p110 $\alpha_L$  and PTEN $_L$  in the two- loop construct is similar to the hypothetical toggle-switch, where the self-activating p110 $\alpha_L$  and PTEN $_L$  mutually inhibit each other through substrate depletion. The mathematical description

of such a system should include a nonlinear equation with saturation kinetics, cooperative repression of the two species,  $u$  and  $v$  as well as the depletion of both species. In a well-mixed system, this can be expressed as:

$$\frac{du}{dt} = \frac{av}{1+v^\beta} - bu \quad (6.1)$$

and

$$\frac{dv}{dt} = \frac{bu}{1+u^\gamma} - av \quad (6.2)$$

where,  $\frac{av}{1+v^\beta}$  and  $\frac{bu}{1+u^\gamma}$  is similar to hill's function with  $\beta$  and  $\gamma$  describing the cooperativity of repression of  $u$  and  $v$ , respectively. In polarisation models,  $u$  represents the active membrane bound polarising molecule (eg: Cdc42-GTP) and  $v$  represents the inactive cytosolic molecule (eg: Cdc42-GDP) whereas,  $a$  and  $b$  describe the effective rates of synthesis of each of these species, respectively. This description of the system allows for bistability and hysteresis when  $\beta$  and  $\gamma > 1$  and can be used to describe bistability and hysteresis that is observed in the two-loop system, when  $p110\alpha_L$  and  $PTEN_L$  are co-expressed in the cell.

### 6.3 The two-loop construct results in all-or-nothing responses at the membrane

Using the system that was constructed in this study, we show that a mechanism similar to the toggle-switch hypothesis can result in population bistability when  $p110\alpha_L$  and  $PTEN_L$  are co-expressed in the cell. The difference between histories between cells that had previously experienced high levels of  $PI(3,4,5)P_3$  and the cells that had not encountered high levels of  $PI(3,4,5)P_3$  (naïve) resulted in a maximum difference of  $\approx 20\%$ . This was the difference between the mean  $PIP_3$ -Indexes in experienced and naïve cells after full induction of  $p110\alpha_L$  and  $PTEN_L$  co-expression (treatment with 25nM of  $\beta$ -estradiol and 50 $\mu$ M of doxycycline). A similar difference was observed between the two histories of the cells treated at 6.25nM of  $\beta$ -estradiol and 25 $\mu$ l of doxycycline (Figure 5.8 and 5.19). The difference between experienced

Table 6.1: Examples of toggle-switch hypothesis for polarisation at the plasma membrane.

Polarising molecules	Toggle-switch mechanism	Ref.
MinE in <i>Escherichia coli</i>	Mutual inhibition between positive feedback loops in MinE and MinD.	[97]
Cdc42-GTP polarisation in <i>Saccharomyces cerevisiae</i>	Mutual inhibition between positive feedback loops in MinE and MinD.	[17]
PI(3,4,5)P <sub>3</sub> in <i>Dictostelium discoideum</i>	Mutual inhibition between positive feedback loops on PI(3,4,5)P <sub>3</sub> and PTEN in the cell was found to be necessary for polarisation.	[65]
PKC3 in <i>Caenorhabditis elegans</i> embryo development	Mutual inhibition between feedback loops on Par1-Par2 complex and PKC3 complex is required for polarisation.	[95]
aPKC in <i>Drosophila melanogaster</i> embryo development	mutual inhibition between feedback loops on Par1 complex and aPKC complex is required for polarisation.	[95]

and naïve cells is smaller than the difference observed in other studies using gene transcription regulation, where differences between histories >40% [89, 51]. The smaller difference observed may suggest that there is a lag-period resulting from the long diffusion distances across the cell to the plasma membrane that is not observed in nucleus. Once the protein concentration near the plasma membrane is increased the switch occurs rapidly to result in the all-or-nothing response that was observed. Cells were either observed to have high GFP levels or mCherry levels at the plasma membrane but, GFP and mCherry were not found to co-exist at the same time on the membrane. Thus, the synthetic system may be used to understand switching behaviour of molecules in other membranes such as RabGTPase switching.

The Rab5-Rab7 enrichment in vesicle mediated endocytosis is one of the most well studied examples of molecular switching at the membrane. RabGTPase are another family of proteins that belong to the Ras-GTP superfamily and consequently are recruited to the membrane through interactions with specific GEFs, GAPs and scaffold proteins. On the vesicle-membrane, Rabs have been found to form distinct domains to spatially restrict cargo for unidirectional transport [90]. The early

endosome membrane is predominantly enriched by Rab5 GTPase and switches to Rab7-GTPase enrichment, marking maturation to late endosome [81]. The mechanism that is thought to regulate the Rab5-Rab7 switch was described as the "cut-out switch" model [22]. The model describes that self-activating Rab5-GTP activates self-activating Rab7-GTP but Rab7-GTP, upon reaching some unknown concentration, Rab7-GTP rapidly replaces Rab5-GTP as it exerts a negative feedback on Rab5-GTP. The presence of a single negative feedback supports the delay in enrichment observed in Rab7-GTP domain formation. The positive feedback on Rab5-GTP and Rab7-GTP is sufficient to trigger bistability with one steady-state in the early endosome (high levels of Rab5-GTP, low levels of Rab7-GTP) and the other steady-state in the late endosome (low-levels of Rab-GTP, high levels of Rab7-GTP). The switch between the two steady-states should be ultrasensitive and show some degree of hysteresis. The negative feedback asserted by Rab7-GTP on Rab5-GTP, would result in the delay of Rab7-GTP enrichment. This suggests that the negative feedback mechanism is experimentally supported by observing strong competition between Rab5-GTP and Rab7-GTP membrane enriched regions; but, very few studies seem to take this model into consideration due to the complexity of Rabs [4]. The two-loop system constructed in this study might suggest that the switching between two states due to the toggle-switch mechanism in a homogeneous system.

#### **6.4 Increasing non-linearity in the system may result in polarisation at the membrane**

Although the system constructed was useful in understanding bistability and hysteresis across the question remains as to why no spatial bistability was observed. With the emphasis that there is a delay caused by molecular diffusion from the cytosol to the membrane, I suggest that the non-linearity of the system would have to increase to overcome the delay of diffusion from within the cell to the plasma membrane. One way of increasing non-linearity in the system is to increase the amount of positive feedback (co-operativity) within each of the two loops. Previous studies have shown that feedback between multiple positive feedback loops can re-

sult in non-linearity which increases irreversibility of switching behaviour [104, 53]. Increase in non-linearity is also suggested in the theoretical models that are often used to describe polarisation i.e., Mori's wave-pinning and Turing-type models.

In brief, as discussed in the introduction chapter, for a polarising molecule ( $u$ ) and its unpolarised state ( $v$ ), the Turing-type model can result in the multiple peaks when the concentration of  $u < \text{some } u_{sat}$  in the characteristic domain of size  $L$  and the Mori's wave pinning model can produce a single large peak when the concentration of  $u > \text{some } u_{sat}$ . In other words, the activator and substrate dynamics result in a concentration at which  $u$  saturates the region, which has dimensions of  $L$  and in the mass conserved system, at low concentrations of  $u$  the Turing-type regime best describes the formation of multiple peaks at the plasma membrane but as the concentration of  $u$  increases at the plasma membrane the regime switches to Mori's wave-pinning type dynamics. This is consistent with observed dynamics of Cdc42-GTPase, where cells form several dynamic clusters of Cdc42-GTP before they form a single pole during early stages of the G1-Phase of the cell cycle. Therefore, both models suggest that there needs to be a sharper contrast between activator and substrate dynamics.

In the cell, sharper contrast between slow activator and the fast diffusing substrate dynamics is achieved by coupling multiple feedback loops within the cell. The positive feedback between Bem1-scaffolding protein and Cdc24- guanine exchange factor are linked to feedback that recruit Cdc42-GDP to the membrane, along with positive feedback that is established between actin dependent vesicle transport of active Cdc42-GTP to the membrane all act to decrease the diffusion rate of Cdc42-GTP at the plasma membrane [99, 61]. Meanwhile the fast diffusing inactive Cdc42-GDP is untethered and is able to diffuse from enriched regions on the plasma membrane and recycling between active Cdc42-GTP and inactive Cdc42-GDP is achieved by feedback from Rdi1, which is a guanine dissociation inhibitor (GDI) [56]. The number of feedback mechanisms that interact to result in differences between activator and membrane dynamics can result in an increase in the non-linearity of the system, as each positive feedback adds to the amplification of the response. The non-linearity also increases inhomogeneity across the cell regions within the cell and in this study,

I show that in the homogeneous well-mixed system, molecular species that are free to diffuse across the plasma membrane result in population bistability but not spatial bistability.

In conclusion, the two-loop construct showed population bistability but spatial bistability was not observed in this study. The lack of spatial bistability was attributed to the low degree of non-linearity in the system, confirming that polarisation requires a more complex two component system, which acts to govern both local and global dynamics at the plasma membrane.

## 6.5 Future perspectives

To make the synthetic system more biologically relevant to observe membrane dynamics that would result in polarisation, the system needs to incorporate shorter switching times as well as higher degree of non-linearity.

First, to increase non-linearity in the system, the constructed system can be compared to the theoretical models that suggest that the synthetic system needs interlinking between more number of feedback loops at the plasma membrane. By introducing higher levels of architecture we can re-engineer processes that are thought to result in polarisation with the toggle-switch mechanism at its core (Table 6.1). For example, in Cdc42-GTP levels of PI(3,4,5)P<sub>3</sub> are known to increase at poles but the function of the increase in PI(3,4,5)P<sub>3</sub> is unknown [68]. Introduction of heterologous proteins in the *S. cerevisiae* cells also provides an opportunity to quantify specific concentration of proteins in the cell, thereby making it a fully quantifiable tuneable synthetic system.

To increase the amount of dynamic and spatial control and decrease switching times, I constructed a blue-light control system that would be able to recruit p110 $\alpha$  to the plasma membrane of the cell upon illumination with blue-light. The system is based on the CIB1/CRY2- system that is found in *Arabidopsis thaliana* [105]. The amount of time for mCherry to localise to the plasma membrane was reduced to  $\approx$  5 minutes and this can be used to further understand the reaction space for cluster and polarisation at cellular membranes (Figure 6.1). Using this model I can see how

an spatial cues at the plasma membrane may result in cluster or pole formation.

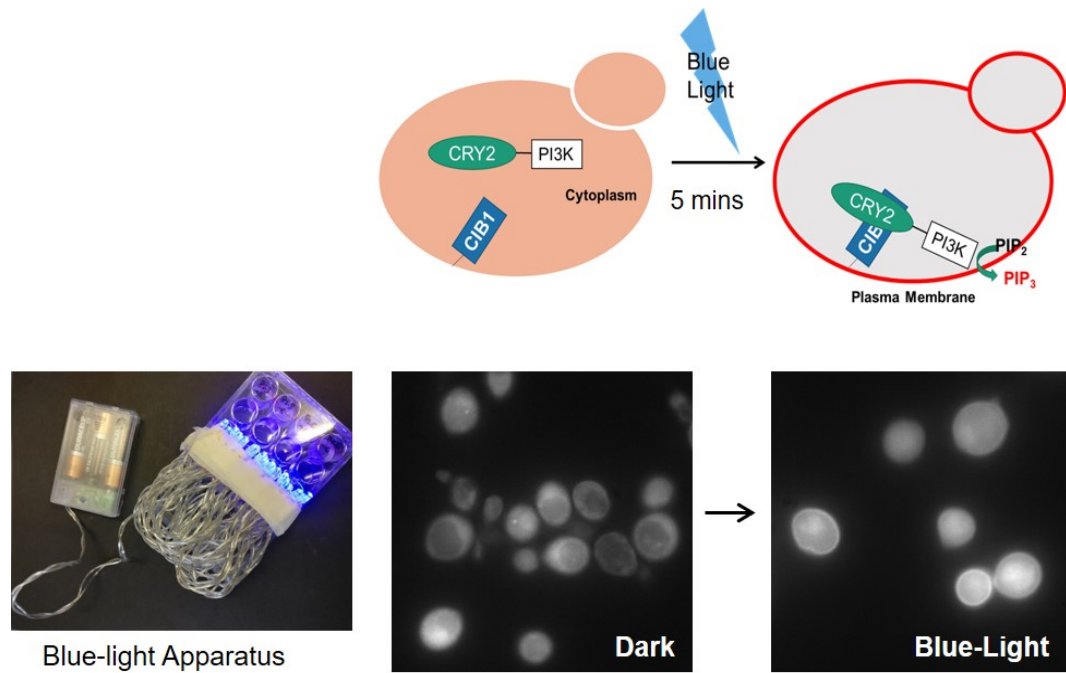


Figure 6.1: Development of the blue-light control system. Schematic representation of the Blue-light control system, where binding is induced by illumination to blue-light. The experimental set-up developed here included LED-lights attached to the lid of the 24-well plate and illumination after five minutes resulted in localisation of mCherry localisation to the plasma membrane, confirming membrane localisation of p110 $\alpha_C$  production of PI(3,4,5)P<sub>3</sub> at the plasma membrane.

## Chapter 7

# Materials and methods

### 7.1 Plastic consumables

<b>Description</b>	<b>Supplier</b>
Eppendorf Safe- Lock Tubes (1.5ml and 2ml)	Eppendorf, UK
Falcon <sup>TM</sup> tubes (15ml and 50ml)	FischerScientific, UK
Grenier CELLSTAR <sup>®</sup> 24-well, suspension culture plates (with lid)	Grenier CELLSTAR <sup>®</sup> , UK
Polystyrene Petri-dishes (92mm x16mm)	Sarstedt, Germany
0.2ml Thin-walled PCR Tubes	Eppendorf, UK
VWR <sup>®</sup> 96-well Real Time PCR Plates skirted plate (white)	VWR International, UK
VWR <sup>®</sup> Ultra clear films for qPCR	VWR International, UK

### 7.2 General glassware

All glassware including 15ml glass boiling tubes, glass pipettes, Duran bottles and 7ml glass vials were purchased from Duran Wheaton Kimble, Germany.

### 7.3 Protein gels and buffers

<b>Description</b>	<b>Supplier</b>
NuPAGE <sup>TM</sup> 4-12% Bis-Tris Protein Gels, 1.0mm, 10-wells	Thermo Fisher Scientific, UK
NuPAGE <sup>TM</sup> MOPS SDS Running Buffer (20X)	Thermo Fisher Scientific, UK

## 7.4 DNA ladders and protein markers

Description	Supplier
1Kb DNA Ladder	New England Biolabs, UK
PageRuler™ prestained Promega protein ladder (10- 180kDa)	ThermoFisher Scientific, UK

## 7.5 List of chemicals and reagents

Description	Supplier
$\beta$ -Estradiol	Sigma-Aldrich, UK
$\beta$ - Mercaptoethanol	Sigma-Aldrich, UK
2-Isopropanol	Fisher Chemicals, UK
Agarose	Sigma-Aldrich, UK
Ampicillin Sodium Salt	Sigma-Aldrich, UK
Chloroform	Fisher Chemicals, UK
Bulk dNTPs	Promega Express, UK
BSA, Molecular Biology Grade	NEB, UK
Doxycyclin hyclate	Sigma-Aldrich, UK
Dimethyl Sulfoxide (DMSO)	Sigma-Aldrich, UK
Ethanol	Fisher Chemicals, UK
Ethylenediamine tetraacetic acid, disodium salt dihydrate (EDTA) disodium salt	Fisher Chemicals, UK
Glacial Acetic Acid	Fisher Chemicals, UK
Glycerol	Fisher Chemicals, UK
Hydrochloric acid AR	Fisher Chemicals, UK
Latrunculin A from sea sponge	Sigma-Aldrich, UK
Lithium Acetate (LiOAc)	Sigma-Aldrich, UK
Milk (skimmed) Powder	Sigma-Aldrich
Polyethylene glycol (PEG 4000)	Sigma-Aldrich, UK
qPCR SyGreen Mix LoRox	PCR Biosystems, UK
Sodium Chloride	Fisher Chemicals, UK
Sodium Citrate	Fisher Chemicals, UK
Sodium Dodecyl Sulfate (SDS)	Melford, UK
Tris(hydroxymethyl)methylamine Hydrochloride (Tris-HCl)	Fisher Chemicals, UK
TRIZMA® Base	Sigma-Aldrich, UK
SuperSignal™ West Pico PLUS Chemiluminescent substrate	Thermo Fisher Scientific, UK
Tween®20	Sigma-Aldrich, UK
Ultrapure™ Salmon Sperm DNA Solution	ThermoFisher Scientific, UK

## 7.6 stains

Description	Supplier	Application
Bromophenol Blue powder	Sigma- Aldrich, UK	Protein Loading buffer
Ethidium Bromide, 1%	Fisher Chemicals, UK	To visualise DNA on Agarose Gel
Fluorescent Brightner 28	Sigma- Aldrich, UK	Chitin stain

## 7.7 Media and supplements

All BD Difco<sup>®</sup> media components were purchased from Fisher Chemicals, UK and all media supplements were purchased from Formedium, UK.

Description	Supplier
Bacto <sup>™</sup> Peptone	Fischer-Scientific, UK
BD Difco <sup>™</sup> Agar	Fischer-Scientific, UK
BD Difco <sup>™</sup> Tryptone	Fischer-Scientific, UK
BD Difco <sup>®</sup> Yeast Extract	Fischer-Scientific, UK
BD Difco <sup>®</sup> Yeast Nitrogenous Base w/o Amino Acids	Fischer-Scientific, UK
D(+)-Glucose, Anhydrous	Fisher Chemicals, UK
Kaiser Mixture Complete Supplement Mixture (CSM)	Formedium, UK
Kaiser Mixture Complete Supplement Mixture single Drop-Out (- Ade,- Ura )	Formedium, UK
Complete Supplement Mixture Double Drop-Out (- Ade, Ura)	Formedium, UK
Complete Supplement Mixture Quadruple Drop-Out (- Ade, His, Leu, Ura )	Formedium, UK

## 7.8 Stock solutions and media

### 7.8.1 Stock solutions

All stock solutions were prepared in 15ml falcon tubes or 2ml eppendorf tubes and stored at -20°C.

### 7.8.2 Media preparation

All components of media were mixed in deionised distilled water before heat sterilisation at 120°C for 20mins. In general batches of 1L were prepared and after sterilisation, liquid media was stored at room temperature and plates were stored at

Table 7.1: Stock Solutions used in this Study

Stock Solution	Solvent	Method
5mM $\beta$ -estradiol stock	Ethanol	Dissolve 1.36 mg in 1ml
5 $\mu$ M $\beta$ -estradiol stock	Filter Sterilized DMSO	Dilute 5 $\mu$ l of 5mM $\beta$ -estradiol stock in 1ml DMSO
1000X Ampicillin Stock	Distilled Water	Dissolve 100mg in 1ml and filter sterilise
20mM Doxycyclin	Distilled Water	Dissolve 1g in 10ml

4°C. Prior to use, plates were dried at 50°C in a dry heat oven for 10 minutes to remove any excess condensation.

### Bacterial media

#### Luria-Bertani Media for growth of *E. coli*

0.01 % Tryptone  
 0.005% Yeast Extract  
 0.085M NaCl  
 1.5% Agar for plating

#### Ampicillin containing Media for plasmid selection in *E. coli*

To make Ampicillin containing media for plasmid selection, 100 $\mu$ l of 1000X Ampicillin stock was added to 1L of autoclaved and cooled Luria-Bertani media. Autoclaved media was cooled to 50-55°C before the addition of the Ampicillin.

### Yeast media

#### YPD Media for growth of *S. cerevisiae*

0.02% Peptone  
 0.01% Yeast Extract  
 0.11M Glucose  
 2% Agar for plating

#### Drop-out Media for selection of *S. cerevisiae* transformants

To select for auxotrophic markers, amino acid drop-out media was prepared to a final composition of 0.01% YNB w/o amino acids, 0.11M Glucose and different amounts of complete synthetic mixtures (CSM) with specific amino acid drop-out were added

(see Table 7.2). For plating, 2% agar was added and the final mixture was autoclaved. All the amino acid supplement mixtures were purchased from Foremedium, UK.

Table 7.2: Amounts of drop-out supplement added to media (w/v)

Amount added (w/v)	CSM - Amino acid Dropout
0.2%	Kaiser- CSM single drop-out - ADE
0.19%	Kaiser- CSM Single drop-out- URA
0.08%	CSM Double drop-out -ADE-URA
0.06%	CSM Quadruple drop-out -ADE-HIS-LEU-URA

### Synthetic complete media *S. cerevisiae*

0.01% (w/v) YNB w/o amino acids  
 0.11M Glucose  
 0.2% Kaiser Complete supplement Mixture (CSM)  
 2% (w/v) Agar for plating

## 7.9 Molecular biology commercial kits

Table 7.3: Commercial molecular biology kits used in this study

Kit Name	Supplier	Application
E.N.Z.A. <sup>®</sup> Cycle Pure-Kit (V-spin column)	Omega Bio-Tek (Norcross, U.S.A.)	PCR purification
E.N.Z.A. <sup>®</sup> DNA Gel Extraction Kit (V-spin)	Omega Bio-Tek (Norcross, U.S.A.)	DNA Extraction from Agarose Gels
E.N.Z.A. <sup>®</sup> Plasmid DNA Mini-Kit I (V-spin column)	Omega Bio-Tek (Norcross, U.S.A.)	Plasmid purification from <i>E.coli</i> cells
Quick-Fusion Cloning Kit	Vazyme, Bimake, UK	Plasmid Construction

## 7.10 Antibodies

Description	Supplier
Anti-p110 $\alpha$ (#4249)	Cell Signal Technologies, UK
Anti- Mouse, HRP- conjugate (#W4021)	Promega, UK
Anti-PTEN (#9552)	Cell Signal Technologies, UK
Anti-rabbit, HRP- conjugate (#7074)	Cell Signal Technologies, UK
Anti-Sp35 (MT50) Polyclonal Antibody	York Bioasciences, UK

## 7.11 Enzymes and enzyme buffers

Enzyme or enzyme buffer	Use	Supplier
10X CutSmart <sup>®</sup> Buffer	Restriction enzyme digestion	NEB, UK
AflII (20,000 units/ml)	Restriction enzyme digestion	NEB, UK
BamHI (25,000 units/ml)	Restriction enzyme digestion	Promega, UK
Buffer E, D, H	Restriction enzyme digestion Buffers	NEB,UK
EcoRI (25,000 units/ml)	Restriction enzyme digestion	Promega, UK
Go <sup>®</sup> Taq Polymerase		
HpaI (5000 units/ml)	Restriction enzyme digestion	NEB, UK
Lyticase from <i>Arthrobacter luteus</i>	<i>S. cerevisiae</i> cell wall digestion	Sigma-Aldrich, UK
MultiCore <sup>™</sup> Buffer Pack	Restriction enzyme Digestion buffers	Promega, UK
Phusion <sup>®</sup> High-Fidelity DNA Polymerase	Polymerase Chain reaction (PCR)	NEB,UK
RNaseA (20 $\mu$ g/ $\mu$ l)	RNA digestion	Omega BioTek, Norcross, USA
Sall (25,000 units /ml)	Restriction enzyme digestion	Promega, UK
SpeI (25,000 units /ml)	Restriction enzyme digestion	Promega, UK
StuI (4000 units /ml)	Restriction enzyme digestion	Promega, UK
T4 DNA ligase	Ligation enzyme	Promega, UK
XhoI (25,000 units/ml)	Restriction enzyme digestion	Promega, UK

## 7.12 Bacterial and yeast organisms

### 7.12.1 Bacterial organisms

*Escherichia coli* cells were used for plasmid amplification. DH5 $\alpha$ <sup>™</sup> (F<sup>-</sup>  $\phi$ 80lacZ $\Delta$ M15  $\Delta$ (lacZYA-argF) U169 *recA1 endA1 hsdR17*(rk<sup>-</sup>, mk<sup>+</sup>) *phoA supE44 thi-1 gyrA96 relA1*  $\lambda$ ) was purchased from ThermoFisher scientific, UK.

### 7.12.2 Yeast organisms

All cells used in this project have been derived from *S. cerevisiae* BMA64-1A (isogenic to W303: *MATa his3-11\_15 leu2-3\_112 ura3-1 trp1D2 ade2-1 can1-100*, Euroscarf, Germany) or BMA64-1B (isogenic to W303: *MAT $\alpha$  his3-11\_15 leu2-3\_112 ura3-1 trp1D2 ade2-1 can1-100*, Euroscarf, Germany). To develop strains that can integrate the GEV system, the plasmid containing the Gall-  $\beta$ -estradiol receptor-Vsp34 fusion protein was integrated to the *mrp7* locus in the genome. To develop strains with the TET-ON system, the plasmid containing rtTA was integrated to the *leu2* locus in the genome. These strains were constructed by Dr. Chieh Hsu, University of Kent, UK.

Table 7.4: Background strains used in this study

Strain Name	Mating Type	Genotype	Purpose
CHK1	MATa	<i>mrp7::P_MRP7-GEV</i>	To develop GEV inducible system
CHK18	MAT $\alpha$	<i>leu2<math>\Delta</math>::P_CLN3-rtTA</i>	To develop TET-ON inducible system

## 7.13 Oligonucleotides and primer design

All oligonucleotides that were required were designed using ApE software were ordered from IDT technologies, USA (website: <https://eu.idtdna.com/pages>).

### 7.13.1 Primers used for cloning

Primers used to amplify cloning sequences using Quick-Fusion Cloning kit (see section 7.16.7), were designed to contain a 15bp overhang, a restriction endonuclease digestion site and a 18-22bp sequence required for the amplification of the insert sequence. The annealing temperature of the 18-22bp region was  $\approx$  55- 61°C and all sequences were amplified using Phusion<sup>®</sup> high fidelity DNA polymerase.

Table 7.5: Phusion primers used to amplify insert sequences for plasmid construction

Insert Sequence	Primers used
<i>mCherry</i>	GCTGGTAGTGCTGGTACTAGTATGGTTT CAAAGGGCGAAGAAGACAATATG
<i>mCherry</i> -antisense	GGCCCTATTTGTACAGAATTCTTACTTGTACAAT TCATCCATAACCACCGGTAG
<i>P_TEF1</i>	GGTACCGGGCCCCCCTCGAGCAA CAGGCGCGTTGG
<i>P_TEF1</i> anti-sense	ACCTTTAGACATTTTGGATCCTTGTAATT AAAACT- TAGATTAG
<i>2Xph(plcδ)</i>	CGCTCTAGAACTAGTGGATCCCAACAG GCGCGTTGGACTTTTAATTTTC
<i>2Xph(plcδ)</i> - antisense	GTGTCTAATTTTGAAGTTAACTTTGATACC ATTCTTTTGTGTTGTCAGCCATG
<i>ph(akt)</i>	
<i>ph(akt)</i> -antisense	GCTGGTAGTGCTGGTACTAGTATGCCTCC AAGAC- CATCATCAGGTG
<i>pten(K13E)*</i>	CCGGATCAATTCGGGGGATCCATGACAGCCAT CAT- CAAAGAGATCGTTAGCAGAAACGAAAGGAGATATC
<i>pten(K13E)</i> -antisense	AGCACTACCAGCACTGTGACGACTTTTGTAAAT TTGTGTATGCTGATC

\* K13E mutation was introduced to PTEN to disrupt PIP<sub>2</sub> binding ability of PTEN so that affinity to the membrane is via localisation domain.

### 7.13.2 Primers for copy number verification

To check the copy number of integrated plasmids, primers were designed for qPCR and Phusion PCR. Primers were designed to be at least 22 nucleotides in length to amplify a region of 60- 100 bp. Primers had an annealing temperature of 60°C and the last two nucleotides at the 3'- end consisted of 2 A/T's (eg: ... AA-3').

Table 7.6: qPCR primers used to determine copy number of integrated plasmids

qPCR	Primers used
<b>2Xph(plc<math>\delta</math>)</b> <i>2Xph(plc<math>\delta</math>)</i> antisense	GACACAACATTGAAGATGGAAGCGTT CGGATCTTTCGAAAGGGCAGATT
<b>act1</b> <i>act1</i> - antisense	GTTTCTGGTATGTGTAAAGCCGGTT ACGTAGGAGTCTTTTTGACCCAT
<b>ade2</b> <i>ade2</i> -antisense	AGTGAGACGTCCCTATTGAATGTT TCAGTACTTCCAAAGCTTCCGGAA
<b>gal1</b> <i>gal1</i> - antisense	GGTAGAAGTCACTACAGCTGCAA TTACCTTTATTTCGTGCTCGATCCTTC
<b>yegfp</b> <i>yeGFP</i> -antisense	CTCCGGTGAAGGTGAAGGTGAT GCAAACATTGAACACCATAACCGAA
<b>mCherry</b> <i>mCherry</i> -antisense	GTCCACATGGAAGGTTCTGTCAA CAAATATCCCAAGCGAATGGCAA
<b>ph(akt)</b> <i>ph(akt)</i> - antisense	CCAAGGCCCAACACCTTTATCAT CATCGTCTCTTCTTCCTGCCTCTT
<b>pten</b> <i>pten</i> -antisense	CTTTGAGTTCCCTCAGCCGTTA CCTCTGGTCCTGGTATGAAGAAT
<b>ura3</b> <i>ura3</i> -antisense	GCAGAATGGGCAGACATTACGAA AGGCCTCTAGGTTCCCTTTGTTACTT

### 7.13.3 Sequencing primer

Primers used for sequencing constructed plasmids in this study included:

Forward Primer   ACTATACTTCTATAGACACGCAAAC

Reverse Primer   TTTCGGTTAGAGCGGATGTG

## 7.14 External plasmids

Plasmids were obtained from different sources and used for cloning as vectors or templates for amplification of inserts for plasmid construction.

Table 7.7: List of External Plasmids used in this study

Plasmid Name	Application	Source/ Reference
pRS426-GFP(S65T)-2XPH(PLC $\delta$ )	Amplification of PIP <sub>2</sub> localisation domain	Stefan <i>et al</i> , 2002 [91]
pYES2-PTEN	For amplification of PTEN sequences for the construction of PTEN plasmids.	Victor <i>et al</i> , 2005 [84]
pRS306	<i>URA3</i> Integration Vector	Hsu <i>et al</i> , 2016 [51]
pRS402-GPD-GFP(S65T)	<i>ADE2</i> Integration Vector and amplification of yeGFP	Nakanishi <i>et al</i> , 2012 [71]
pCHK006-GAL1UAS-p110 $\alpha$ -linker-CAAX	Plasmid for p110 $\alpha_M$ construct	Dr. Chieh Hsu, University of Kent, UK
pCHK019-GAL1UAS-p110 $\alpha$ -linker	Plasmid for p110 $\alpha_C$ construct	Dr. Chieh Hsu, University of Kent, UK
pCHK040-GAL1UAS-PH(AKT)-Linker-mcherry	Vector for p110 $\alpha_L$ and mCherry reporter plasmid.	Dr. Chieh Hsu, University of Kent, UK
pCHK043-[TetO <sub>2</sub> ] <sub>7</sub> -yeGFP	Vector for GFP reporter plasmid construction.	Dr. Chieh Hsu, University of Kent, UK
pCHK052-[TetO <sub>2</sub> ] <sub>7</sub> -p110 $\alpha$ -Linker	Vector for PTEN <sub>L</sub> and PTEN <sub>C</sub> plasmid construction	Dr. Chieh Hsu, University of Kent, UK
pCHK068-[PtetO <sub>2</sub> ] <sub>7</sub> -yeGFP-CAAX	Vector for PTEN <sub>M</sub> plasmid construction	Dr. Chieh Hsu, University of Kent, UK
pTH761-CEN-mCherry_v4	Yeast codon optimised mCherry reporter	Chu <i>et al</i> , 2014 [21]

## 7.15 Software

Software	Website
ApE	<a href="http://www.biology.utah.edu/jorgensen/wayned/ape/">http://www.biology.utah.edu/jorgensen/wayned/ape/</a>
BibTeX	<a href="http://www.bibtex.org/">http://www.bibtex.org/</a>
ImageJ	<a href="http://rsbweb.nih.gov/ij/">http://rsbweb.nih.gov/ij/</a>
LaTeX	<a href="http://www.latex-project.org/">http://www.latex-project.org/</a>
Mathematica	<a href="http://www.wolfram.com/mathematica/">http://www.wolfram.com/mathematica/</a>
R Studio	<a href="https://www.rstudio.com/products/rstudio/">https://www.rstudio.com/products/rstudio/</a>

## 7.16 DNA methods

### 7.16.1 General cloning strategy

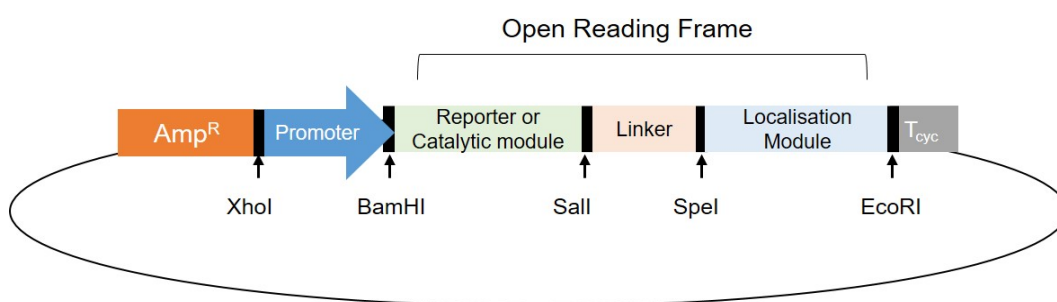


Figure 7.1: Schematic diagram illustrating open reading frame plasmid design.

Unless otherwise mentioned, plasmids were designed to express fusion proteins, which were made up of three parts: a reporter or catalytic module, a linker region and a plasma membrane localisation domain. Sequences in the open reading frame were flanked by endonuclease restriction enzyme digestion sites that allowed for convenient removal or insertion of sequences (Figure 7.1). Promoter sequences were flanked by XhoI and BamHI restriction enzyme digestion sites. The sequences within the open reading frame contained at least three modules that were separated by Sall, SpeI and EcoRI enzyme digestion sites. The open reading frame sequence was followed by a terminator sequence ( $T_{CYC1}$ ) to terminate expression in yeast cells.

### 7.16.2 Plasmids constructed in this study

construct plasmids, vectors were created by restriction enzyme digestion (Section 7.16.1) and the insert DNA sequences were used to construct a new plasmid using T4- ligation or Quick- Fusion Cloning Kit. Insert DNA sequences that were made for Quick-Fusion cloning kit were PCR amplified using primers designed (Section 7.13.1). Insert DNA sequences used for T4- ligase were restriction enzyme digested as described in section 7.16.1.

Table 7.8: List of Plasmids constructed in this study and cloning notes. **V:** plasmid vector used and **I:** describes the insert DNA modules. For insert modules that were used for Quick-Fusion cloning kit, see section 7.13.1.

Plasmid No.	Name	Cloning Notes ( <b>V:</b> Vector <b>I:</b> Insert)	Method
pRKC2	[TetO2] <sub>7</sub> -PTEN-Linker-CAAX	<b>V:</b> pCHK68 (BamHI/SalI) <b>I:</b> PTEN (K13E)	Fusion Cloning
pRKC13	[TetO2] <sub>7</sub> -PTEN-Linker	<b>V:</b> pCHK52 (BamHI/SpeI) <b>I:</b> pRKC2 (BamHI/SpeI)	T <sub>4</sub> ligase
pRKC14	[TetO2] <sub>7</sub> -PTEN-Linker-2XPH(PLC $\delta$ )	<b>V:</b> pRKC13 (BamHI/SpeI) <b>I:</b> pRKC3 (BamHI/SpeI)	T <sub>4</sub> ligase
pRKC15	GALIUAS-PH(AKT)-p110 $\alpha$	<b>V:</b> pCHK49 <b>I:</b> p110 $\alpha$	Fusion Cloning
pRKC20	<i>P</i> <sub>-</sub> <i>TEF1</i> -yeGFP	<b>V:</b> pRKC024 (XhoI/BamHI) <b>I:</b> Genomic DNA	Fusion Cloning
pRKC21	<i>P</i> <sub>-</sub> <i>ADH1</i> -yeGFP	<b>V:</b> pRKC024 (XhoI/BamHI) <b>I:</b> Genomic DNA	Fusion Cloning
pRKC22	<i>P</i> <sub>-</sub> <i>URA3</i> -yeGFP	<b>V:</b> pRKC024 (XhoI/BamHI) <b>I:</b> Genomic DNA	Fusion Cloning
pRKC23	<i>P</i> <sub>-</sub> <i>CLN3</i> -yeGFP	<b>V:</b> pRKC024 (XhoI/BamHI) <b>I:</b> Genomic DNA	Fusion Cloning
pRKC24	<i>P</i> <sub>-</sub> <i>TEF1</i> -mCherry-mCherry_v4	<b>V:</b> pRKC024 (EcoRI/SpeI) <b>I:</b> pTH761-CEN-mCherry_v4	Fusion Cloning
pRKC26	<i>P</i> <sub>-</sub> <i>TEF1</i> -PH(AKT)-mCherry_v4	<b>V:</b> pRKC24 (BamHI/SalI) <b>I:</b> pCHK049 (BamHI/SalI)	T4 ligase
pRKC28	<i>P</i> <sub>-</sub> <i>TEF1</i> -GFP-2XPH(PLC $\delta$ )	<b>V:</b> pRKC20 (BamHI/HpaI) <b>I:</b> 2XPH(PLC $\delta$ )	Fusion Cloning

### 7.16.3 Restriction enzyme digestion and DNA fragment purification

Restriction enzyme digestion of plasmids was performed to linearise vectors, cleave out specific DNA modules or to perform restriction enzyme checks on plasmids. To digest DNA for cloning purposes, a total volume of 50  $\mu\text{l}$  was set-up and to perform restriction enzyme checks of DNA plasmids, a 20  $\mu\text{l}$  reaction was set up. All reactions were incubated for at least 2 hours at 37° C and observed using DNA gel electrophoresis (see Section 7.16.4). To isolate the necessary fragments that were required for further cloning, the gel was visualised on a UV-transilluminator and the fragment was cut out using a scalpel. The DNA was purified from the gel using the protocol prescribed by the E.N.Z.A.® Gel Extraction Kit and eluted with 30  $\mu\text{l}$  of the elution buffer provided. The concentration and purity of the sample was determined using the method described in Section 7.16.10.

#### Restriction endonuclease digestion reaction

1-5 $\mu\text{g}$	Plasmid DNA
1X	10X Buffer
0.5 $\mu\text{g}$	BSA, Acetylated
5-10 U	each restriction enzyme

To ensure maximum activity of restriction endonucleases, double digests were performed using 10X Buffers that were determined using the Promega Restriction enzyme tool (<https://www.promega.co.uk/resources/tools/retool/>).

### 7.16.4 DNA gel electrophoresis

The concentration of the agarose gel was determined based on the size of the fragment that needed to be resolved (see Table 7.9). Agarose was added in 1X TAE electrophoresis buffer (40mM Tris- Base, 20 mM Acetic acid, 1mM EDTA) and heated for two minutes or until all agarose was completely dissolved in the TAE buffer. The mixture was cooled at room temperature for a few minutes before adding 0.5  $\mu\text{g}/\text{ml}$  of Ethidium Bromide, which was used to visualise the DNA (see Table 7.9). The mixture was poured into a gel cast to and solidified at room temperature for 30 minutes. Gel electrophoresis was performed using a Flowgen Biosciences Horizontal

gel electrophoresis system and the tank was filled with 1x TAE buffer until the gel was fully submerged. Electrophoresis was performed at the 120V for 15 minutes. After sufficient separation of the DNA fragment of interest, the gel was visualised and documented using the GeneSys G-box system.

Table 7.9: Concentration of agarose used to resolve DNA fragments

<b>Band size Resolution</b>	<b>Conc. of Agarose</b>
500 - 10, 000 bp	1.0 %
400- 7, 000 bp	1.2%
200 - 3, 000 bp	1.5%

### 7.16.5 T<sub>4</sub>- ligation

To ligate two DNA fragments that were digested with restriction endonucleases that produce cohesive ends, a reaction of a total volume of 5 $\mu$ l was set up and incubated 2 hours at room temperature. Depending on the DNA concentration that was determined using the method described in Section 7.16.10, a ratio of 1 : 1 - 3 : 1 volumes of insert DNA to linearised vector backbone was used.

#### T<sub>4</sub>- ligation mixture

1X            10X T<sub>4</sub>- Ligase Buffer  
 1U            T<sub>4</sub>- Ligase  
 1:1 - 1:3    Ratio of Vector: Insert  
 0.5 mM    ATP

### 7.16.6 Phusion<sup>®</sup> high fidelity DNA polymerase chain reaction

To amplify modules that were required for plasmid construction using Quick-Fusion Cloning kit, Phusion<sup>®</sup> High Fidelity DNA Polymerase (New England Biolabs, UK) was used. The reaction was assembled on ice in a thin walled 0.2 ml PCR tube and all Phusion PCRs were done using the hot-start program described below. Hot-start technique was used to reduce unspecific amplification of DNA. The technique involves pre-heating the thermocycler to the denaturation temperature (98° C) before placing the PCR tubes containing the reaction mixture into the machine. Upon completion of

the PCR program, 10  $\mu\text{l}$  of the PCR reaction was run on a gel to confirm amplification of the expected sequence length (see Section 7.16.4). The product was then purified from the remaining PCR mixture using the the protocol prescribed for the E.N.Z.A.® Cycle Pure-Kit. Purified DNA was eluted from the column using 30  $\mu\text{l}$  of the elution buffer and the yield and purity of the eluted product was measured (Section 7.16.10).

#### **Phusion® reaction mixture**

1X	5X Phusion Buffer
200 $\mu\text{M}$	10mM dNTPs
0.5 $\mu\text{M}$	10 $\mu\text{M}$ Forward Primer
0.5 $\mu\text{M}$	10 $\mu\text{M}$ Reverse Primer
100-250 ng	Template DNA
1 units/ 50 $\mu\text{l}$ PCR	Phusion polymerase

#### **Thermocycling conditions for Phusion DNA Polymerase amplification**

HOT START

98°C      10 minutes

INITIAL DENATURATION

98°C      30 seconds

AMPLIFICATION CYCLES (30 CYCLES)

Denaturation	98°C	10 seconds
Annealing	$T_{annealing}$	15 seconds
Extension	72° C	$t_{extension}$

FINAL EXTENSION

72° C      5 minutes

HOLD

16°C       $\infty$

where,  $T_{annealing}$  was determined based on the difference between predicted melting temperatures ( $\Delta T_M$ ) of the primers. If the difference between the two  $T_M$ 's  $< 4^\circ$

C then the lowest of the two temperatures was chosen as the  $T_{annealing}$ . When the difference was  $>4^{\circ}$  C then the  $T_{annealing}$  was determined by using gradient PCR. The parameter of  $t_{extension}$  was calculated as 30 seconds per kb.

### 7.16.7 Quick-Fusion cloning kit

Quick- Fusion Cloning kit was used to construct plasmids from linearised vector and phusion amplified PCR products. A total reaction volume of  $5\mu\text{l}$  was set up in a sterile 1.5ml eppendorf's tube. The reaction was incubated for 30 minutes at  $37^{\circ}\text{C}$  and the amounts of linearised vector and insert added to the reaction were calculated using the following equations:

**To determine volume of linearised vector:**

$$[0.005 \cdot \text{length of linearised vector}(\text{bp})]\text{ng}$$

**To determine volume of insert:**

$$[0.01 \cdot \text{length of insert (bp)}]\text{ng}$$

#### Fusion Cloning Reaction

10-50 ng	Linearised Vector
5-50 ng	Insert DNA
1X	5X Fusion Buffer
0.25 $\mu\text{l}$	Fusion Enzyme

### 7.16.8 Heat-shock transformation protocol of chemically competent *E. coli* cells

To amplify plasmids that were constructed either by  $T_4$  ligation or Fusion Cloning,  $2.5\mu\text{l}$  of ligation reaction was transformed into  $50\mu\text{l}$  of DH5 $\alpha$  *E. coli* cells (ThermoFisher Scientific, UK). Thawed cells were added to the ligation mixture and incubated on ice for 10 minutes. Heat-shock was performed at  $42^{\circ}$  C for 60 seconds. The cells were placed back on ice for 2 minutes. The reaction mixture was spread onto LB agar plates containing  $100\mu\text{g/ml}$  of Ampicillin and incubated overnight at

37° C.

### 7.16.9 Bacterial colony PCR and Mini-Prep

To select colonies for the isolation of amplified plasmids, at least 10 single colonies from transformation plates were streaked onto a fresh LB agar plate containing 100 $\mu$ g/ml of Ampicillin. The plate was incubated at 37°C for 8-10 hours and colony PCR was performed to select colonies containing the plasmid. Colony PCR was performed using *Taq* DNA Polymerase (ThermoFisher Scientific, UK). At least 5 colonies containing the insert were inoculated in 3ml of LB liquid media, containing 100  $\mu$ g/ml of Ampicillin and grown overnight at 37° C. Miniprep was performed using the E.N.Z.A. <sup>®</sup> Plasmid DNA Mini-Kit I with 2ml of the overnight culture. Purified plasmid was eluted with 50  $\mu$ l of the elution buffer provided. The purity and concentration of the product was checked using the method described in Section 7.16.10. Mini-prepped plasmids were stored at -20° C and restriction enzyme check was performed to select three plasmids for sequencing (see Section 7.16.11).

#### Colony PCR Mixture:

1X	10X <i>Taq</i> Buffer-Mg <sup>2+</sup>
1.5 mM	50mM MgCL <sub>2</sub>
0.2 mM	Each dNTP
0.5 $\mu$ M	Forward Primer
0.5 $\mu$ M	Reverse Primer
2.5 units	<i>Taq</i> DNA Polymerase (5U/ $\mu$ l)

#### Thermocycling conditions for *Taq* DNA polymerase amplification

INITIAL DENATURATION

94°C      3 minutes

AMPLIFICATION CYCLES (30 CYCLES)

Denaturation	94°C	45 seconds
Annealing	55°C	30 seconds
Extension	72°C	<i>taq<sub>extension</sub></i>

FINAL EXTENSION

72°C      10 minutes

HOLD

16°C      ∞

where,  $taq_{extension}$  describes the amount of time required to amplify the sequence of interest and is dependent on the length of the sequence. In general this was set to 60 seconds per 1kb.

#### 7.16.10 DNA concentration and purity determination

To check the concentrations of DNA samples, 2  $\mu$ l of eluted sample and 2  $\mu$ l of elution buffer (as blank) were loaded onto the micro-wells of a BMG LABTECH LVis Plate. The lid was closed and the plate was placed into the SpectroStar Omega (BMG Labtech, UK) plate reader to measure the absorbance at 260 nm ( $A_{260}$ ) and the ratio  $A_{260}/A_{280}$ . Pure DNA samples have a ratio of 1.8 - 2.0 and these samples were stored at -20° C for further use. Samples with high levels of RNA contamination that showed a ratio >2.0 were discarded.

#### Equation to Calculate DNA Yield:

$$Yield = A_{260} \cdot df \cdot \frac{1}{\epsilon} \cdot v \quad (7.1)$$

where, the DNA yield is determined in  $\mu$ g,  $\frac{1}{\epsilon}$  is the reciprocal of the DNA extinction co-efficient, which is equal to 50  $\mu$ g/ml for dsDNA,  $df$  represents the dilution factor and  $v$  is the total volume in ml.

#### 7.16.11 DNA sequencing

To verify the sequence of plasmids that were constructed in this study, plasmid DNA was sent to GATC, Germany for Sanger sequencing using the SUPREMERUN Tube Services (<https://www.eurofinsgenomics.eu/>). Samples were diluted in nuclease-free water to a final volume of 20  $\mu$ l. Plasmid DNA samples were diluted to a concentration of 50-100ng/ $\mu$ l and primers required for sequencing of the plasmid, were diluted to 10 pmol/ $\mu$ l.

### 7.16.12 LiAc/carrier DNA/ PEG transformation protocol for plasmid integration to *S. cerevisiae* genome

Plasmids were designed for gene integration so that linearisation of the plasmid results in homologous ends that allows integration into the genome. Reporter plasmids were integrated at the *ura3* gene locus and the plasmids containing PTEN or p110 $\alpha$  were integrated at the *ade2* gene locus. The enzymes StuI and AflII (NEB, UK) were used to linearise reporter (*ura3* plasmid) and catalytic plasmids (*ade2* plasmid), respectively. Linearised plasmids were transformed to yeast cells using the LiAc/ carrier DNA/ PEG protocol. Strains that were required for transformation were inoculated from glycerol stock onto YPD-Agar plates and grown overnight at 30° C. One colony of cells was inoculated into 3 ml of liquid YPD and was grown in a shaking incubator (180 RPM) at 30° C, overnight. On the next day, cells were diluted 1:100 in 20 ml of fresh liquid YPD and grown to an OD<sub>600</sub>  $\approx$ 0.4 (3-5hours). Cells were spun down at 4000 RPM, the pellet was washed with 20 ml of dH<sub>2</sub>O and resuspended in 10 ml of LiT solution (10 mM Tris-Cl pH 7.5 and 100 mM LiOAc). The resuspended cells were incubated at room temperature for 40 minutes with gentle shaking. Meanwhile, linearised plasmid DNA reaction mixture was prepared and the reaction was incubated for at least 30 minutes at 37°C. LiT was used to resuspend the cells (100 $\mu$ l per transformation reaction) and 100  $\mu$ l of cell suspension, 5  $\mu$ g of sterile salmon sperm carrier DNA (sterilised at 90° C for 10 minutes) and 300  $\mu$ l of PEG 4000 solution (50% (w/v) made in LiT and filter sterilised) were added to the linearized DNA. The reaction was incubated for 10 minutes at room temperature followed by heat shock at 42° C for 15 minutes. The cells were harvested by centrifugation at >10,000 RPM for one minute and the supernatant was discarded. The cell pellet was resuspended in 100  $\mu$ l of 10 mM Tris-HCl and spread onto selective plates. The plates were incubated at 30° C for 2-3 days. From the plate 5-10 colonies were selected and streaked onto fresh selection plate. Plates were incubated overnight at 30° C and selection was repeated one more time before glycerol stocks were made.

**Plasmid linearisation reaction**

1 $\mu$ g	Plasmid DNA
0.2 $\mu$ g	BSA
2U	Restriction enzyme
1X	CutSmart Buffer

**7.16.13 Glycerol stocks of yeast strains**

To make glycerol stocks, selected transformants were grown in 1ml of liquid YPD, overnight at 30°C and glycerol was added to make up 30% (v/v) of the solution. The tubes were frozen at -80°C.

**7.16.14 Haploid strains constructed in this study****7.16.15 Copy number determination of integrated plasmid to *S. cerevisiae* genome**

To determine the copy number of the integrated plasmid at the specific locus of the genome, qPCR and Phusion PCR were performed. Primers used to determine copy number are described in section 7.13.2.

**Copy number determination using quantitative PCR (qPCR)**

A fresh colony of haploid yeast cells was inoculated to 5ml of YPD liquid and grown overnight at 30°C. Cells were diluted to OD<sub>600</sub> 1-6 and 6ml of cell suspension was spun down at 4000RPM for five minutes. The pellet was resuspended in 1ml of sterile distilled water and transferred to a 2ml eppendorf tube. The cells were spun down at > 10, 000 RPM for one minute and the supernatant was discarded. The cell pellet was resuspended in 150 $\mu$ l of 1.0 M SCE (1M Sorbitol, 0.1M Sodium Citrate, 75 mM EDTA, pH adjusted to 7.0 using NaOH) and 20 $\mu$ l of lyticase, 2 $\mu$ l of RNase A and 1 $\mu$ l of  $\beta$  - mercaptoethanol were added. The mixture was incubated at 30°C for an hour and 500 $\mu$ l of lysis buffer (100mM Tris-HCl, 50mM EDTA, 1.2% SDS) was added and incubated at room temperature for 15 minutes. To the reaction, 360 $\mu$ l of 7M NH<sub>4</sub>OAc

Strain Name	Mating Type	Integration site::Inserted Sequence (Plasmid)	Parent Strain	Genetic Background
RKC2	<i>MAT<math>\alpha</math></i>	URA3 $\Delta$ :: <i>P</i> <sub>TEF1</sub> -GFP-2XPH(PLC $\delta$ ) . (pRKC28)	CHK18	CHK18
RKC7	<i>MAT<math>\alpha</math></i>	ADE2 $\Delta$ ::[TetO <sub>2</sub> ] <sub>7</sub> -PTEN-2XPH(PLC $\delta$ ) (pRKC14)	RKC2	CHK18
RKC11	<i>MAT<math>\alpha</math></i>	URA3 $\Delta$ :: <i>P</i> <sub>TEF1</sub> -yeGFP (pRKC20)	CHK18	CHK18
RKC12	<i>MAT<math>\alpha</math></i>	URA3 $\Delta$ :: <i>P</i> <sub>ADH1</sub> -yeGFP (pRKC21)	CHK18	CHK18
RKC50	<i>MAT<math>\alpha</math></i>	ADE2 $\Delta$ ::[TetO <sub>2</sub> ] <sub>7</sub> -PTEN-Linker-CAAX (pRKC2)	RKC2	CHK18
RKC51	<i>MAT<math>\alpha</math></i>	ADE2 $\Delta$ ::[TETO <sub>2</sub> ] <sub>7</sub> -PTEN-Linker (pRKC13)	RKC2	CHK18
RKC17	<i>MAT<math>\alpha</math></i>	URA3 $\Delta$ :: <i>P</i> <sub>TEF1</sub> -PH(AKT)-mCHv4 (pRKC24)	CHK001	CHK1
RKC35	<i>MAT<math>\alpha</math></i>	ADE2 $\Delta$ ::GAL1UAS-p110 $\alpha$ -Linker-CAAX (pCHK19)	RKC17	CHK1
RKC37	<i>MAT<math>\alpha</math></i>	ADE2 $\Delta$ :: GAL1UAS-p110 $\alpha$ -Linker (pCHK6)	RKC17	CHK1
RKC39	<i>MAT<math>\alpha</math></i>	ADE2 $\Delta$ ::GAL1UAS-PH(AKT)-p110 $\alpha$ (pRKC15)	RKC17	CHK1
RKC96	<i>MAT<math>\alpha</math></i>	URA3 $\Delta$ :: <i>P</i> <sub>CLN3</sub> -GFP (pRKC23)	CHK18	CHK18
RKC97	<i>MAT<math>\alpha</math></i>	URA3 $\Delta$ :: <i>P</i> <sub>URA3</sub> -GFP(pRKC22)	CHK18	CHK18

was added and thoroughly mixed by inverting the tube. 650 $\mu$ l of Chloroform was added to the mixture and the tube was vortexed for 30 seconds before centrifugation at >10,000 RPM for two minutes. The supernatant was discarded and the pellet was washed three times with 70% Ethanol. The pellet was air dried at room temperature for 30 minutes and resuspended in 50  $\mu$ l of 10 mM Tris-HCl. The purity and yield of the DNA extract was determined using the method described in Section 7.16.10. In a 96-well white skirted plate (Sarstedt, Germany) the following qPCR mixture was prepared on ice and a 96-well acetate film was used to seal the plate. The reaction was made using the 2X qPCRBIO SyGreen mix (PCR BioSystems, UK), which was vortexed for 30 seconds before use.

### qPCR Mixture

1X            2X qPCRBIO SyGreen mix  
400 nM    Forward Primer  
400 nM    Reverse Primer  
≈500ng    Genomic DNA

Data acquisition was performed using CFX Connect™ RealTime PCR Detection System (Biorad, UK) using the SYBR® Green channel and the following PCR program was used:

### qPCR Conditions

POLYMERASE ACTIVATION

95°C       3 minutes

AMPLIFICATION CYCLES (44 CYCLES)

95°C    5 seconds

60°C    30 seconds

MELT ANALYSIS

### **Calculating the number of copies using $C_q$ values**

To determine the number of copies of the transformed plasmid, the  $C_q$  values were obtained from the amplification curve. The threshold was set using the automatic threshold option. The mean ( $C_\mu$ ) was calculated for the internal control genes (*act1* and *gal1*) and the number of copies (CN) of the integrated plasmid was determined using the following formula:

$$CN = 2^{C_q - C_\mu} \quad (7.2)$$

Melt curve analysis was also used together with  $C_q$  values to confirm the quality of the product. In general, a single peak melt curve was concluded to have produced successful amplification of the gene.

## 7.16.16 Diploid strains constructed for this study

## Yeast mating

Simple mating was performed using *MATa* and *MAT $\alpha$*  haploid cells. A single colony of *MAT $\alpha$*  cells were spotted onto a fresh YPD- Agar plate and then *MATa* cells were mixed together. The diploid cells were grown overnight at 37°C and streaked onto SC drop-out agar plated. The plates were incubated for at least four hours at 30°C before a second selection was performed on a fresh SC drop-out agar plate.

Table 7.10: Diploid Strains

Diploid	Haploid Parent	Genotype		Function
	<i>MATa</i>	<i>ade2<math>\Delta</math>::ADE2</i> (Plasmid No.)	<i>ura3<math>\Delta</math>::URA3</i> (Plasmid No.)	
RKC91	RKC17	empty plasmid (pRS402)	<i>P<sub>-</sub>TEF1</i> -PH(AKT)-mCh_v4 (pRKC17)	Dual reporter Control
	RKC2	-	<i>P<sub>-</sub>TEF1</i> -GFP-2XPH(PLC $\delta$ ) (pRKC28)	
RKC41	RKC37	GAL1UAS-p110 $\alpha$ - Linker (pCHK19)	<i>P<sub>-</sub>TEF1</i> -PH(AKT)-mCh_v4 (pRKC17)	p110 $\alpha_C$
	RKC2	-	<i>P<sub>-</sub>TEF1</i> -GFP-2XPH(PLC $\delta$ ) (pRKC28)	
RKC67	RKC39	GAL1UAS-PH(AKT) -p110 $\alpha$ (pRKC15)	<i>P<sub>-</sub>TEF1</i> -PH(AKT)-mCh_v4 (pRKC17)	p110 $\alpha_L$
	RKC2	-	<i>P<sub>-</sub>TEF1</i> -GFP-2XPH(PLC $\delta$ ) (pRKC2) (pRKC28)	

Table 7.11: Diploid strains (Continued)

Diploid	Haploid Parent	Genotype		Function
	<i>MATa</i>	<i>ade2Δ::ADE2</i> _ (Plasmid No.)	<i>ura3Δ::URA3</i> _ (Plasmid No.)	
	<i>MATα</i>			
RKC40	RKC35	GAL1UAS-p110α - <i>Linker</i> - <i>CAAX</i> ( <i>pCHK6</i> )	<i>P</i> _ <i>TEF1</i> - PH(AKT)-mCh_v4 (pRKC17)	p110α <sub>M</sub>
	RKC2	-	<i>P</i> _ <i>TEF1</i> -GFP- 2XPH(PLCδ) ( <i>pRKC28</i> )	
RKC73	RKC37	GAL1UAS-p110- <i>Linkerα</i> ( <i>pCHK19</i> )	<i>P</i> _ <i>TEF1</i> - PH(AKT)-mCh_v4 (pRKC17)	p110α <sub>C</sub> + PTEN <sub>C</sub>
	RKC51	[TetO <sub>2</sub> ] <sub>7</sub> - PTEN(K13E)- <i>Linker</i> (pRKC13)	<i>P</i> _ <i>TEF1</i> -GFP- 2XPH(PLCδ) ( <i>pRKC28</i> )	
RKC71	RKC39	GAL1UAS- PH(AKT)-p110α ( <i>pRKC15</i> )	<i>P</i> _ <i>TEF1</i> - PH(AKT)-mCh_v4 (pRKC17)	Open Loop
	RKC51	[TetO <sub>2</sub> ] <sub>7</sub> - PTEN(K13E)- <i>Linker</i> (pRKC13)	<i>P</i> _ <i>TEF1</i> -GFP- 2XPH(PLCδ) ( <i>pRKC28</i> )	
RKC76	RKC35	GAL1UAS-p110α - <i>Linker</i> - <i>CAAX</i> ( <i>pCHK6</i> )	<i>P</i> _ <i>TEF1</i> v- PH(AKT)-mCh_v4 (pRKC17)	p110α <sub>M</sub> + PTEN <sub>C</sub>
	RKC51	[TetO <sub>2</sub> ] <sub>7</sub> - PTEN(K13E)- <i>Linker</i> (pRKC13)	<i>P</i> _ <i>TEF1</i> -GFP- 2XPH(PLCδ) ( <i>pRKC28</i> )	

Table 7.12: Diploid strains (Continued)

Diploid	Haploid Parent	Genotype		Function
	<i>MATa</i>	<i>ade2Δ::ADE2</i> _ (Plasmid No.)	<i>ura3Δ::URA3</i> _ (Plasmid No.)	
RKC31	RKC35	GAL1UAS- p110 $\alpha$ - <i>Linker</i> ( <i>pCHK19</i> )	<i>P</i> _ <i>TEF1</i> - PH(AKT)-mCh_v4 ( <i>pRKC17</i> )	p110 $\alpha_C$ + PTEN $_L$
	RKC7	[TetO $_2$ ] $_7$ - PTEN(K13E)- 2XPH(PLC $\delta$ ) ( <i>pRKC14</i> )	<i>P</i> _ <i>TEF1</i> -GFP- 2XPH(PLC $\delta$ ) ( <i>pRKC28</i> )	
RKC62	RKC39	GAL1UAS- PH(AKT)-p110 $\alpha$ ( <i>pRKC15</i> )	<i>P</i> _ <i>TEF1</i> - PH(AKT)-mCh_v4 ( <i>pRKC17</i> )	Toggle Switch
	RKC7	[TetO $_2$ ] $_7$ - PTEN(K13E)- 2XPH(PLC $\delta$ ) ( <i>pRKC14</i> )	<i>P</i> _ <i>TEF1</i> -GFP- 2XPH(PLC $\delta$ ) ( <i>pRKC28</i> )	
RKC89	RKC35	GAL1UAS-p110 $\alpha$ - <i>Linker</i> - <i>CAAX</i> ( <i>pCHK6</i> )	<i>P</i> _ <i>TEF1</i> - PH(AKT)-mCh_v4 ( <i>pRKC17</i> )	p110 $\alpha_M$ + PTEN $_L$
	RKC7	[TetO $_2$ ] $_7$ - PTEN(K13E)- 2XPH(PLC $\delta$ ) ( <i>pRKC14</i> )	<i>P</i> _ <i>TEF1</i> -GFP- 2XPH(PLC $\delta$ ) ( <i>pRKC28</i> )	
RKC64	RKC35	GAL1UAS- PH(AKT)-p110 $\alpha$ ( <i>pRKC15</i> )	<i>P</i> _ <i>TEF1</i> - PH(AKT)-mCh_v4 ( <i>pRKC17</i> )	p110 $\alpha_L$ + PTEN $_M$
	RKC7	[TetO $_2$ ] $_7$ - PTEN(K13E)- <i>Linker</i> - <i>CAAX</i> ( <i>pRKC2</i> )	<i>P</i> _ <i>TEF1</i> -GFP- 2XPH(PLC $\delta$ ) ( <i>pRKC28</i> )	

## 7.17 Inducing protein expression using synthetic promoters

### 7.17.1 Inducing expression using the GEV system

In brief, the GEV system is synthetic system that is constructed using a fusion protein of Gal4p, estradiol receptor and VPS34. Using  $\beta$ -estradiol, expression can be induced in a highly tuneable manner as increasing levels of  $\beta$ - estradiol result in increasing levels of translocation of fusion protein that allows binding of the GAL1UAS sequence and downstream expression of the protein. To induce cells using this system, cells were inoculated into 3 ml of SC- liquid and pre-incubated for 18-20 hours at 30°C in a a sterile 15ml boiling tube. Pre-incubated cells were diluted to make a cell suspension of  $OD_{600} \approx 0.04$ , using fresh SC- liquid. In a 15ml falcon tube, 10 ml of a 4X  $\beta$ -estradiol stock was prepared using 40  $\mu$ l of the 5  $\mu$ M  $\beta$ -estradiol stock (described in Table 7.1) and 9.96ml of SC-liquid. To induce cells with  $\beta$ -estradiol, a total volume of 3ml was prepared in a fresh boiling tube. Cells were innoculated to a final  $OD_{600}$  of 0.01 and the final concentration of  $\beta$ -estradiol was 25 nM. p110 $\alpha$  expression was controlled using the GEV system and induced cells were subjected to microscopy or growth assays as described in the following sections.

### 7.17.2 Inducing expression of TET-ON system

The TET-ON system is also a commonly used synthetic promoter that is used to control expression of proteins in *S. cerevisiae* cells. The presence of Tetracyclin or Doxycyclin relieves repression by rtTA. To induce expression using the TET-ON system, 50  $\mu$ M of Doxycyclin was used on the cells. Prior to induction, cells were grown for 18-20 hours in 3 ml of SC-liquid at 30°C. Cells were diluted to an  $OD_{600}$  of 0.04 and a 4X Doxycyclin stock was prepared using 100mul of the 20 mM Doxycyclin Stock solution (see Table 7.1) and 9.9 ml of fresh SC-liquid. Since, PTEN expression was controlled using the TET-ON system, p110 $\alpha$  was co-expressed to study the activity of PTEN. In a well of a 24-well cell suspension plate, a total volume of 1ml containing a final  $OD_{600}$  of 0.01 of cells, 50muM of Doxycyclin and 25 nM of

$\beta$ -estradiol was prepared. These cells were subjected to experiments as described below.

## 7.18 Yeast growth rate analysis

To observe differences in the growth rate of cells the doubling time determined in the log phase of the growth curve. Using 15 ml boiling tubes cells were inoculated to 3 ml of fresh SC-liquid and incubated for 18-20 hours at 30° C. The cells were diluted in 10 ml of fresh SC-liquid and the OD<sub>600</sub> was adjusted to 0.04. In a 24-well cell suspension plate, the conditions to analyse the growth rate were prepared to a final volume of 1 ml. The plate was placed in the BMG LABTECH SPECTROStar nano plate reader and the OD<sub>600</sub> was measured at 30°C for a total run time of 24 hours ( $\approx$  180 measurements). The plate was set to linearly shake at 400 RPM and then orbitally shake for 30 seconds prior to taking the OD<sub>600</sub> measurement. Orbital shaking was used to ensure a well-mixed sample before measurement of cell density. Measurement of cell density was taken in eight minute intervals. BMG LABTECH MARS program was used to process the data that were save as Microsoft Excel files. Mathematica (see Appendix) was used to fit log-phase data to an exponential curve, using the model described in equation 1.2. R-squared values were also calculated to measure goodness of fit. The doubling time was measured using equation 1.4, where the constant,  $a$  was determined from fitted data.

### Equation to calculate doubling time

We know that exponential growth model is described by:

$$N(t) = N_0 e^{at} \quad (7.3)$$

where,  $N(t)$  is cell density as a function of time,  $N_0$  is the initial cell density,  $a$  is a constant and  $t$  is time in minutes. To determine the doubling time of cells,  $N(t) = 2N_0$  at such that

$$2N_0 = N_0 e^{at} \quad (7.4)$$

$$\ln(2) = \ln(e^{at}) = at \quad (7.5)$$

Therefore, the doubling time ( $t_{doubling}$ ) can be determined as,

$$t_{doubling} = \frac{\ln(2)}{a} \quad (7.6)$$

### 7.18.1 Promoter strength analysis

To investigate strength of GFP expression driven by different promoters, amongst individual cells exp, FACS (fluorescence activated cell sorting) was used in this study for high throughput single cell quantification of GFP expression. The BD (Becton-Dickinson) FACSCalibur flow cytometer was used to assay the bacterial samples here. BD FACSCalibur having an Argon blue laser for excitation at 488 nm and the FL1 detector centred at 530 nm with 30 nm bandpass filter fits well for the GFP fluorescence quantification.

Cells were inoculated to overnight culture in 3 ml of SC-liquid in a 15ml boiling tube and diluted to  $OD_{600}$  to 0.01 using fresh SC-liquid. 3 ml of diluted culture was placed in a sterile 5ml round-bottom polystyrene tube and the tube was placed on ice prior to sampling by the BD FACSCalibur flow cytometer. A negative control strain (same strain but GFP free) was used to warmed up flow cytometer (Argon laser 488 nm, FL1 detector 530/30 nm) and appropriate instrument settings were made using the BD CellQuest Pro software on a MAC workstation. The settings for forward and side scatter detectors were adjusted to place the acquired cells in the proper location on the scatter graph. The gain for FL1 detector was set to 1.00 in log mode. Across all trials, 10,000 total events were collected for each sample with low flow rate at room temperature.

## 7.19 Fluorescence microscopy and quantification method

### 7.19.1 Sample preparation

To visualise cells using fluorescence microscopy, 3  $\mu\text{l}$  of cell culture was aspirated onto a clean glass slide (76x 26 mm, Menzel-Glaser, ThermoFischer, UK). A cover slip of thickness 0.16 -0.19 mm was gently placed onto the slide, avoiding air bubbles. A drop of immersion oil (Cargille immersion oil, Type LDF, Sigma-Aldrich, UK) was put on the coverslip before placing the slide on the stage.

### 7.19.2 Wide-field microscope Set-up and Image acquisition

The set-up used to image the cells is built around the Olympus IX2 UCB series microscope and Micro-Manager v1.4.22 software. The excitation light was emitted by a light emitting diode CoolLED pE4000 (CoolLED, UK), which was filtered using filter cubes. For green light excitation of mCherry fluorophore, Olympus U-MNG (excitation filter 530 - 550nm and bandwidth of 40) was used and for Blue light excitation of GFP fluorophore, Olympus U-MWB (excitation filter 450-480 nm and bandwidth 35) was used. To focus incident light onto the sample and emitted light from the sample, Olympus UPLSAP0 100XO NA 1.4 Oil Immersion objective lens was used and a complementary metal oxide semiconductor camera, Zyla 5.5 sCMOS (ANDOR, Oxford Instruments, UK) was used to detect fluorescence. In general each image was collected within 90 seconds. Images across all channels were acquired with the exposure time set to 100.0032 ms and pixel size of 0.065  $\mu\text{m}$ .

### 7.19.3 Setting scale-bar on ImageJ

Images were analysed using ImageJ program. To set scale bar, the size of the camera sensor chip and the magnification was used. The size of the camera chip was 6.5  $\mu\text{m}$  and the magnification used was 100x. These values were entered into image properties using the *Analyse > Set scale* option on the menu bar. The pixel aspect ratio and unit of length were set to 1.00 and  $\mu\text{m}$ , respectively. Using, *Analyse > Tools > Scale Bar* on the menu bar, 5  $\mu\text{m}$  was represented on representative images.

## 7.20 Image quantification

### 7.20.1 Machine learning based algorithm for quantification of cells

To increase the amount of cells detected and quantified, a machine learning based algorithm was developed in this study. The method of quantification is discussed in Chapter 2. The main steps included and lastly, the quantification of *PIP<sub>3</sub>- Index* of cells. All the source codes used for the machine learning based algorithm were developed by Dr. Chieh Hsu, University of Kent and are included in Appendix B.

### 7.20.2 Hysteresis experiments

To study the maintenance of memory on the membrane, cells were induced with  $\beta$ -estradiol in a 15ml boiling tube as described in section 7.17.1, to produce high PI(3,4,5)P<sub>3</sub> cells and uninduced cells were used to produce low PI(3,4,5)P<sub>3</sub> cells. From the culture, 200  $\mu$ l of induced and uninduced culture was put into a 15ml falcon tube and spun down at 4000RPM for 5 minutes. The cells were washed twice with 10ml of fresh SC-liquid media and collected at 4000 RPM for 5 minutes. Cells were suspended in 10ml of fresh SC-liquid and the OD<sub>600</sub> was adjusted to 0.04. In a 24-well plate cells were inoculated to a final volume of 1ml and an OD<sub>600</sub> of 0.01. These cells were grown in conditions described in table 7.13 for 16 hours at 30°C and then observed using fluorescence microscopy. Cells that were pre-induced with 25 nm of were referred to as memory cells and cells that were uninduced were referred to as naive cells.

Table 7.13: Growth conditions used to study maintenance of memory.

<b>Aim</b>	<b>Growth Condition</b>
To test wash steps	No inducer present
To observe difference in history at fully induced p100 $\alpha_L$ and PTEN $_{C/L}$	Presence of both inducers at 25nM $\beta$ Estradiol and 50 $\mu$ M Doxycyclin.
To observe difference in history at leakage PTEN $_{C/L}$	Presence of $\beta$ estradiol concentration gradient (25nM -0nM) and no Doxycyclin was present in the media.
To observe difference in history at leakage PTEN $_L$	Presence of $\beta$ estradiol concentration gradient (25nM -0nM) and 25 $\mu$ M or 5 $\mu$ M of Doxycyclin was added to the cells.

## 7.21 Protein methods

### 7.21.1 Preparation of cell- free lysate

To quantify the level of protein expression, western blot was performed on crude cell lysate. The method used to prepare cell lysate for western blot procedure was adapted from methods described by von der Haar *et al*, 2017. Cells were inoculated and grown in test conditions from which, 200 $\mu$ l of cells ( $OD_{600} \approx 10^8$ ) was harvested and resuspended in 200 $\mu$ l of lysis buffer (0.1M NaOH, 0.05M EDTA, 2% SDS, 2%  $\beta$  mercaptoethanol). The cell suspension was boiled at 90°C for 10 minutes. To neutralise the reaction 5  $\mu$ l of 4M Acetic acid was added and the tube was vortexed for 30 seconds. 10  $\mu$ l of the neutralised reaction was used to quantify the amount of protein extracted as described in Section 7.21.2. The samples were sonicated at 20% amplitude for 10 seconds and boiled for a further 10 minutes at 90°C after adding 50 $\mu$ l of loading buffer (0.25M Tris-HCl (pH6.8), 50% Glycerol, 2% SDS, 0.05%Bromophenol Blue).  $\approx 20\mu$ g of cell lysate was loaded onto a NuPAGE™ 4-12% Bis-Tris pre-cast gel.

### 7.21.2 Protein quantification using UV-Spectrometer

Cell lysate was prepared as described in Section 7.21.1 and 10 $\mu$ l of lysate was diluted in 1ml of distilled water. The diluted lysate was placed in a UV-transparent cuvette and the  $A_{280}$  was measured. To determine the amount of protein in the sample, the following equation was used:

#### Equation used to calculate protein concentration

$$\text{Concentration of protein } (\mu\text{g}/\mu\text{l}) = A_{280} \cdot \text{Dilution Factor } (0.01) \quad (7.7)$$

### 7.21.3 Gel electrophoresis and wet-transfer procedure

Gel electrophoresis was performed using XCell SureLock™ Mini-Cell Electrophoresis system at 100V for 2 hours. For separation of high molecular weight proteins, NuPAGE MOPS SDS Running buffer was used. To transfer proteins from gel to 0.2 micron Nitrocellulose Membrane, wet transfer was performed using a Mini TransBlot®

transfer apparatus. Fiber pads, Whatmann filter paper and the nitrocellulose membrane were cut to the dimensions of the gel (7x8cm) and equilibrated in transfer buffer (25mM Tris, 192mM Glycine, 20% methanole, pH8.3) for 15 minutes at room temperature. The Gel sandwich (fiber pad- filter paper- membrane- gel- filter paper -fiber pad ) was set-up in a gel holder cassette. The cassette was placed into the apparatus such that the gel was facing the cathode and the chamber was filled with transfer buffer. Transfer was performed at 70V and at 4°C for 2 hours. To confirm successful transfer, the membrane was stained using Ponceau stain (0.1% Ponceau S, 5% Acetic Acid) and destained by washing with distilled water.

#### **7.21.4 Immunoblotting for detection of Protein**

To perform immunoblotting for the detection of specific proteins, the transfer membrane was blocked using 5% milk in TBS for 1 hour at room temperature. The membrane was washed twice using 15ml TBS for 5 minutes each and incubated with 15ml of diluted primary antibody. All primary antibodies were diluted 1:1000 in 5% milk and TBS-T, except for p110 $\alpha$  antibody which was diluted in 5% BSA and TBS-T. Incubation times for primary antibodies varied and are given in Table 7.14. The transfer membrane was washed three times using TBS-T for five minutes and incubated with 10ml of diluted HRP-conjugated secondary antibody. Secondary antibody was diluted in 5% TBS (1:2000) and incubated for one hour at room temperature. After incubation, the transfer membrane was washed three times using TBS-T for five minutes and proceeded to detection. For detection of HRP -conjugated secondary antibody, 5ml of SuperSignal West Pico Plus reagent was prepared used on the transfer membrane. The blot was visualised and documented using Genesys G-Box system.

Table 7.14: Conditions used for immunoblotting detection of proteins. Primary Antibodies used in this study were diluted in either 5% BSA or milk, 1X TBS, 0.1% Tween<sup>®</sup> 20. Transfer membranes were incubated in 15ml of diluted primary antibodies for specified lengths of time. Secondary Antibodies were prepared in 5% Milk, 1X TBS, 0.1% Tween<sup>®</sup> 20 and the transfer membrane was incubated for one hour at room temperature before detection.

Primary Antibody	Dilution used	Incubation time	Secondary antibody
Anti- p110 $\alpha$ (4249, Cell Signal Technologies, UK)	1:1000 in 5% (w/v) BSA, 1X TBS, 0.1% Tween <sup>®</sup> 20	16-18 hours at 4°C	Anti- rabbit secondary HRP- conjugate (7074, Cell Signal Technologies, UK)
Anti- PTEN (9552, Cell Signal Technologies, UK)	1:1000 in 5% Milk, 1X TBS, 0.1% Tween <sup>®</sup> 20	2 hours at room temperature	Anti- rabbit secondary HRP- conjugate (7074, Cell Signal Technologies, UK)
Anti-GFP (11814460001, Roche, UK)	1:1000 in 5% Milk, 1X TBS, 0.1% Tween <sup>®</sup> 20	16-18 hours at 4°C	Anti- mouse secondary HRP- conjugate (W4021, Promega, UK)

## Appendix A

# Review of Phosphoinositol metabolism in *S. cerevisiae*

### A.0.1 PI(3)P and PI(3,5)P<sub>2</sub> are present on membranes involved in sensing environmental changes in the cell

PI(3)P is required for autophagosome formation during nutrient depletion and PI(3,5)P<sub>2</sub> is required for controlling vacuole size and morphology during hyperosmotic stress. PI(3,5)P<sub>2</sub> is synthesized by the phosphorylation of PI(3)P on late endosomal membranes, which fuse to the vacuolar membrane[31]. Vps34p, a Class III PI3K provides an economical way of dedicating PI(3)P enriched membranes to form endosomes or preautophagosome structures. For the formation of endosomes, Vps34p synthesizes PI(3)P and also binds to other proteins to form Complex II, which is required for PI(3,5)P<sub>2</sub> synthesis[12]. For preautophagosome formation, the kinase recruits proteins to form Complex I, which allows assembly of autophagosome complexes[43]. Therefore, PI(3)P and the Vps34p complexes play an important role in deciding cell fate in response to environmental changes.

During hyperosmotic stress, increased levels of Complex II elevate PI(3,5)P<sub>2</sub> levels to control vacuole size and morphology. In normal conditions the levels of PI(3,5)P<sub>2</sub> constitutes < 0.1% of total cellular phospholipids[29]. During hyperosmotic stress, the levels of PI(3,5)P<sub>2</sub> transiently increase by at least 20-fold for 30 minutes[10]. The increase in PI(3,5)P<sub>2</sub> is observed along with an increase in vacuole

fission and decrease in vacuolar membrane surface area. After 30 mins, the size of the vacuole returns to normal as the levels of PI(3,5)P<sub>2</sub> return to normal, suggesting that PI(3,5)P<sub>2</sub> plays an essential role in maintaining cell homeostasis through vacuole membrane fission and fusion during stress conditions.

During nutrient deprivation, inactivation of the target of rapamycin complex- I (TORC1) results in increased levels of Vps34p Complex- I formation. The key difference between Vps34p complex I and II is the presence of Atg14p[43]. The presence of Atg14 in Complex I results in the localisation of Vps34p complex on the membranes to form preautophagosomal structures, which matures into an autophagosome after recruitment of proteins binding to PI(3)P (eg: p40<sup>phox</sup>)[43]. The inactivation of the TORC1 results in upregulation of Atg14p and other components required for autophagosome formation[73]. The elevated levels of Atg14p increase the chances of the formation of Vps34p Complex I, which results in autophagosome formation at PI(3)P enriched membranes and the non-specific degradation of organelles in the cells.

### **A.0.2 PI(4)P and PI(4,5)P<sub>2</sub> are present on membranes that are involved in sensing growth conditions**

PI(4)P defines membranes involved in secretion and also acts as a substrate for the synthesis of PI(4,5)P<sub>2</sub> for cell growth. PI(4)P is one of the first phosphatidylinositol phosphates that was discovered and *S. cerevisiae* cells have been shown to maintain two distinct pools, known as the golgi and non-golgi pools. The two pools are synthesized by membrane-specific kinases and there are two main types of PI4K that are found to synthesise PI(4)P from PI in *S. cerevisiae*[92, 11]. Pik1p (TypeIII $\beta$ ) makes up 40-45% of total cellular PI(4)P from PI. Stt4p (TypeIII $\alpha$ ) makes up 40-60% of total PI(4)P as well as some PI(4,5)P<sub>2</sub>. Deletion of these membrane-specific kinases result in specific defects in the cell, suggesting that the different pools of PI(4)P do not intermix[101].

The golgi pool of PI(4)P is synthesised from PI by Pik1p, and the loss of function in the kinase is shown to have severe defects in cell growth and protein secretion[2]. In wild-type cells, it is found to be present in cytoplasmic puncta containing the

trans-golgi marker Sec7p, which is involved in the endoplasmic reticulum (ER)-to-golgi transport[46].

The majority of the non-golgi pool of PI(4)P is present on the plasma membrane for the synthesis of PI(4,5)P<sub>2</sub>, by Stt4p(stausporin and temperature sensitive protein)[92]. The PI(4)P at the plasma membrane is further phosphorylated by Mss4p (a PI 4-phosphate 5- Kinase) to produce PI(4,5)P<sub>2</sub>, which is required to maintain cell wall integrity, cytoskeleton structure and for polarised cell growth. Stt4p temperature sensitive mutants show loss of cell wall integrity, cytoskeleton structure and polarised growth[2]. These results show that plasma membrane PI(4)P predominantly acts as substrate to increase levels of PI(4,5)P<sub>2</sub>. During starvation, PI(4)P levels on the plasma membrane are significantly reduced to limit levels of PI(4,5)P<sub>2</sub> synthesis.

In *S. cerevisiae* PI(4,5)P<sub>2</sub> is produced from PI(4)P by Mss4p and plays an important role in regulating processes required for normal cell growth[106]. PI(4,5)P<sub>2</sub> is a major substrate for phospholipase C (Plc1p), to produce inositol (3,4,5)P<sub>3</sub> (IP<sub>3</sub>) and 1,2- Diacylglycerol (DAG). The deletion of PLC1 gene is associated with severe growth defects as IP<sub>3</sub> and DAG. IP<sub>3</sub> diffuses to the ER and binds to the IP<sub>3</sub> receptor, creating a channel to release intracellular calcium stores[7]. Calcium ions are required to stabilise components of the cytoskeleton and for the permeability of ion channels. In mammalian cells, DAG stays on the membrane to activate Protein Kinase C pathway resulting in cell proliferation and growth; however, it seems unclear if DAG acts in a similar manner as a secondary messenger in yeast to activate PKC homologue, Pkc1p. There is more evidence supporting the activation of Pkc1p by members of the RhoGTPase family[77].

Intact plasma membrane containing PI(4,5)P<sub>2</sub> along with other cell membrane stress receptors (Wsc1/2/3p, Mid2 and Mtl1) recruit Rom1p and Rom2p to the membrane in their active form[62]. Active Rom1p and Rom2p activate Rho1-GTPase, which in turn activates Pkc1p. Pkc1p activates the MAPK cascade, which includes Bck1p, Mkk1p and Mkk2p, resulting in normal cell growth and proliferation. During starvation and mechanical stress the levels of PI(4,5)P<sub>2</sub> and cell membrane stress receptors are reduced, respectively. The reduced levels of Pkc1p activation results in

a slower cell growth and G2-phase cell-cycle arrest, preventing bud formation[77].

During bud formation, Cdc42-GTPase form poles to define the bud-site in a PI(4,5)P<sub>2</sub> dependent manner[45]. Endosomes enriched with active Cdc42-GTPase are transported along actin filaments to the plasma membrane to regions already enriched with active Cdc42-GTP (as described in Introduction Chapter). In *S. cerevisiae* PI(4,5)P<sub>2</sub> is known to interact with at least 100 different proteins including those involved in actin cytoskeleton reorganisation[3].

**Phosphatidylinositol Metabolism in *S. cerevisiae***

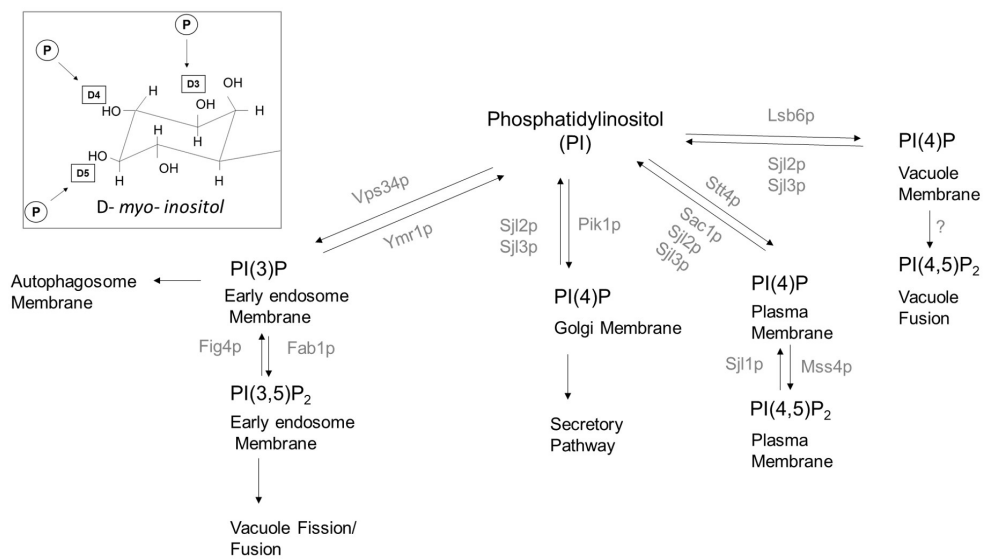


Figure A.1: Summary of phosphatidylinositol metabolism in *S. cerevisiae*. Phosphatidylinositol (PI) derivatives are produced by the phosphorylation of the D3, D4 and D5 positions in the *D-myoinositol* ring (inset). PI itself doesn't possess any known function other than to act as a substrate for membrane specific kinases. Phosphatase dephosphorylates derivatives to allow dynamic regulation of membranes.

# Appendix B

## Source Code

### B.1 Image segmentation

#### Python Script

##### B.1.1 Image restructuring .tiff → .jpeg

```
#python 3.4

import fnmatch
import os
import shutil
import argparse
from PIL import Image
import numpy as np

parser = argparse.ArgumentParser(description='Flattern data structure')
parser.add_argument('--source', action='store',
                    help='the original image folders')
parser.add_argument('--target', action='store',
                    default='data_restructured/',
                    help='where to store the image data')
```

```
args = parser.parse_args()

target_dir=args.target
source_dir=args.source

def flattern_data_structure(source_dir, target_dir):
print("flattening the data structure...")
for root, dirnames, filenames in os.walk(source_dir):
for dirnames in fnmatch.filter(dirnames, 'GFP'):
new_folder_name=root.replace(source_dir,"").replace("/","__").replace(" ", "_")
t=target_dir+"/"+new_folder_name
print("processing "+ t)
shutil.copytree(root,t)

def rename_tiffs(target_dir):
print("renaming the tif files...")
for root, dirnames, filenames in os.walk(target_dir):
for filenames in fnmatch.filter(filenames, 'img*.tif'):
if target_dir.endswith("/"):
new_file_name=root.replace(target_dir,"").replace("/","__")+ ".tif"
else:
new_file_name=root.replace(target_dir+"/","").replace("/","__")+ ".tif"
print("processing "+ new_file_name)
shutil.move(root+"/"+filenames,root+"/"+new_file_name)

def create_jpgs(target_dir, colour):
print("creating jpgs "+ colour+" channel")
for root, dirnames, filenames in os.walk(target_dir):
```

```
for filenames in fnmatch.filter(filenames, '*'+colour+'.tif'):
    image_file=root+"/"+filenames
    jpg_file=image_file.replace('tif','jpg')
    print("converting "+jpg_file)

    im3=Image.open(image_file)
    newImagedata=[]
    maxPixelValue=max(list(im3.getdata()))
    for i in im3.getdata():
        newImagedata.append(i*256/maxPixelValue)
    im2=Image.new('L',im3.size)
    im2.putdata(newImagedata)
    im2.save(jpg_file,"JPEG",quality=90)

while True:
    try:
        os.mkdir (target_dir)
        flatten_data_structure(source_dir, target_dir)
        rename_tiffs(target_dir)
        create_jpgs(target_dir,"mCh")
        create_jpgs(target_dir,"GFP")
        break
    except:
        print ("Something is wrong. Probably the target folder already exists.")
        break
```

### B.1.2 Identification of squares containing cells in the image

```
from __future__ import absolute_import
from __future__ import division
```

```
from __future__ import print_function

import argparse
import os
import shutil
import time
import csv
import csv
import numpy as np
import argparse
start_time=time.time()
import tensorflow as tf

def read_tensor_from_image_invert(file_name,input_mean=0,input_std=255):
    input_name = "file_reader"
    output_name = "normalized"
    file_reader = tf.read_file(file_name, input_name)
    image_reader = 255 - tf.image.decode_jpeg(file_reader, channels=3, name="jpeg_rea
float_caster = tf.cast(image_reader, tf.float32)
dims_expander = tf.expand_dims(float_caster, 0)
sess = tf.Session()
result = sess.run(dims_expander)
return result

def crop_and_resize2(
    file_name, index=0, cr=10, intrasteps=2, input_size=299, input_mean=0, input_std=
    axis_steps=cr+(cr-1)*intrasteps
```

```
x_pos=int(index/axis_steps)/(cr*(intrasteps+1))
y_pos=(index%axis_steps)/(cr*(intrasteps+1))
block=np.array([y_pos,x_pos,1/cr,1/cr])
cropblock=block*ori_size
file_reader = tf.read_file(file_name)
image_reader = tf.image.decode_and_crop_jpeg(file_reader,cropblock,channels=3)
float_caster = tf.cast(image_reader, tf.float32)
dims_expander = tf.expand_dims(float_caster, 0)
normalized = tf.divide(tf.subtract(dims_expander, [input_mean]), [input_std])
file_resized = tf.image.resize_images(normalized,[input_size,input_size])
return file_resized
```

```
def load_graph(model_file):
    graph = tf.Graph()
    graph_def = tf.GraphDef()
    with open(model_file, "rb") as f:
        graph_def.ParseFromString(f.read())
    with graph.as_default():
        tf.import_graph_def(graph_def)
    return graph
```

```
def drawboundary(ts,index,cr=10, intrasteps=2):
    axis_steps=cr+(cr-1)*intrasteps
    x_pos=int(index/axis_steps)/(cr*(intrasteps+1))
    y_pos=(index%axis_steps)/(cr*(intrasteps+1))
    cropblock=[[y_pos,x_pos,y_pos+1/cr,x_pos+1/cr]]
    return tf.image.draw_bounding_boxes(ts,cropblock)
```

```
def box_coor_imageJ(index,cr=10, intrasteps=2, ori_size=2048):
    axis_steps=cr+(cr-1)*intrasteps
    x_pos=int(index/axis_steps)/(cr*(intrasteps+1))
    y_pos=(index%axis_steps)/(cr*(intrasteps+1))
    block=np.array([x_pos,y_pos,1/cr,1/cr])
    cropblock=block*ori_size
    return cropblock

def draw_image_from_invert(ts,fname='invert.jpeg'):
    session=tf.Session()
    bb= tf.cast(ts, tf.uint8)
    cc=tf.squeeze(bb)
    output_image = tf.image.encode_jpeg(cc)
    file_name = tf.constant(fname)
    file = tf.write_file(file_name, output_image)
    session.run(file)
    session.close()

def sortIndex(cr=10, intrasteps=2):
    axis_steps=cr + (cr-1)*intrasteps
    xlen=[cr]+[cr-1 for x in range(cr-1)]
    ylen=[cr]+[cr-1 for x in range(cr-1)]
    a=[]
    for y in range(intra+1):
        for x in range(intra+1):
            for yy in range(xlen[y]):
                for xx in range(ylen[x]):
                    cornerNumber=x + y*axis_steps
                    a.append(cornerNumber+xx*(intrasteps+1)+yy*axis_steps*(intrasteps+1))
```

```
    return a

parser = argparse.ArgumentParser(description='Identifying the cells')
parser.add_argument('--image', action='store',
                    default='testImage.jpg',
                    help='the image file (default is testImage.jpg)')
parser.add_argument('--cropping', action='store',
                    default=10, type=int,
                    help='cropping tiles')
parser.add_argument('--intra', action='store',
                    default=4, type=int,
                    help='shifting steps')
parser.add_argument('--model_size', action='store',
                    default=96, type=int,
                    help='image size for model training')
parser.add_argument('--working', action='store',
                    default='./',
                    help='where all the images to process are')

print('initialising...')
args = parser.parse_args()

graph=load_graph(args.working+'CH_cell_ID_model_20180815.pb')
input_name = "import/Placeholder"
output_name = 'import/final_result'
input_operation = graph.get_operation_by_name(input_name)
output_operation = graph.get_operation_by_name(output_name)

image_file=args.image
cropping=args.cropping
```

```
intra=args.intra
model_size=args.model_size
total=(cropping+(cropping-1)*intra)**2

block_isCell=[]
tsStack=[]
interStack=[]
count=0

print("cropping the ori image into " + str(total)+ " pieces..." )
with tf.Session(graph=graph) as sess1:
    for i in range(total):
        print("cropping "+str(i)+" of "+str(total))
        norm=crop_and_resize2(image_file,index=i, intrasteps=intra,cr=cropping,input_
        #tsStack.append(sess1.run(norm))
        interStack.append(norm)
        print("time passed: " + str(time.time()-start_time))
        tsStack=sess1.run(tf.stack(interStack))

print("start calculating....")
print("time passed: " + str(time.time()-start_time))
with tf.Session(graph=graph) as sess2:
    for i in tsStack:
        print("calculating "+str(count)+" of "+str(total))
        result=np.squeeze(sess2.run(output_operation.outputs[0], {input_operation.output
        block_isCell.append(max(enumerate(result), key=lambda x: x[1])[0]==0) #0=good c
        count=count+1
    print("time passed: " + str(time.time()-start_time))

#sorting for ROI overlapping according to "layers"
```

```

coorList=[]
for i in sortIndex(cr=cropping, intrasteps=intra):
    if block_isCell[i]:
        coorList.append(box_coor_imageJ(index=i,cr=cropping,intrasteps=intra))

with open(image_file.replace('.jpg','_boxes.csv'), 'w', newline="") as csvfile:
    w1=csv.writer(csvfile)
    w1.writerows(coorList)

print("total time passed: " + str(time.time()-start_time))

```

\section{Identification of cell boundary}

### ImageJ macro

```

/*
 * Version 20180816
 * Directly process the regions identified to produce profiles around each cells
 * Should be no problem to act on unfinished folder
 * Chieh Hsu @ Uni Kent, UK
 * maxRadius=100
 */
setBatchMode(true);
roiManager("reset");

```

### B.1.3 Data import

```

dataRestructuredDir=getDirectory("select the dir");
subDirs = getFileList(dataRestructuredDir);
//getCellROIfromSquares("__62.8__+E__C1__1__GFP_ROI.zip","L:\\ML_first_trial\\
checkingOnWindows-ruk20180614\\data_restructured\\__62.8__+E__C1__1__GFP\\")

```

```
for (i = 0; i < subDirs.length; i++){
subDir=subDirs[i];
if(endsWith(subDir, "/")){
subDir=replace(subDir, "/", "")+"\\";
execSingleDir(dataRestructuredDir+subDir, "mCh"); //boundary based on mCh
execSingleDir(dataRestructuredDir+subDir, "GFP"); //boundary based on GFP
}
}
print("All done!");

function execSingleDir(currentDir, colour){
dataDir=currentDir+colour+"\\";
allFiles = getFileList(dataDir);
for (i = 0; i < allFiles.length; i++){
if(endsWith(allFiles[i], "boxes.csv")){
print("processing " +dataDir+ allFiles[i]);
squareROI=roiGeneratorML(allFiles[i], dataDir);
cellROI=getCellROIfromSquares(squareROI, dataDir);
profileAtTheBoarder(cellROI, dataDir, "mCh"); //processing the mCh picture
profileAtTheBoarder(cellROI, dataDir, "GFP"); //processing the GFP picture

}
}
}
```

#### B.1.4 Generating cell profiles

```
function profileAtTheBoarder(cellROI, boundaryDir, colourToProcess){
```

```
maxRadius=100;
steps=360;
angleIncrease= 2*PI/steps;
tempString=split(boundaryDir,"\\");
whichBoundary = tempString[tempString.length-1]; //mCh or GFP
profileName="profile_boundary_defined_by_"+whichBoundary;
experiment = tempString[tempString.length-2]; //also the basic name of the image
parentDir=File.getParent(boundaryDir)+"\\";
imageDir=parentDir+colourToProcess+"\\";
saveDir=parentDir+profileName+"\\";

if (!File.exists(saveDir)) File.makeDirectory(saveDir);
if (!File.exists(boundaryDir+cellROI)){
print("no cell boundary defined by "+whichBoundary+" in "+boundaryDir);
return false;
}

print("saving profiles");
roiManager("reset");
roiManager("Open", boundaryDir+cellROI);
tifFile=experiment+"__"+colourToProcess+".tif";

open(imageDir+tifFile);

for(rr=0; rr<roiManager("count");rr++){
roiManager("deselect");
roiManager("select", rr);
rawData=newArray(0);
boudaryRadius=newArray(steps);
indBegin=newArray(steps);
indEnd=newArray(steps);
```

```
resultFileName=experiment
+
"_"+colourToProcess+"_"+profileName+"_cell_"+toString(rr)+".csv";

if(File.exists(saveDir+resultFileName)){
print ("File exists: "+resultFileName);
}
else {
file=File.open(saveDir+resultFileName);
print("saving "+resultFileName);

List.setMeasurements;
xC=List.getValue("X");
yC=List.getValue("Y");

for(i=0; i<steps; i++){

x=xC+cos(i*angleIncrease)*maxRadius;
y=yC+sin(i*angleIncrease)*maxRadius;
makeLine(xC,yC, x, y);
lineProfile = getProfile();
indBegin[i]=rawData.length;
rawData = Array.concat(rawData,lineProfile);
indEnd[i]=rawData.length;

//find the boundary
roiManager("deselect")
roiManager("select", rr);
boudaryRadius[i]=0;
x=xC;
```

```
y=yC;
while (selectionContains(x, y)) {
x=xC+cos(i*angleIncrease)*boudaryRadius[i];
  y=yC+sin(i*angleIncrease)*boudaryRadius[i];
    boudaryRadius[i]=boudaryRadius[i]+1;
  }
}

Array.getStatistics(boudaryRadius, min, max, mean, stdDev);
maxR=max;
minR=min;
alignedRadius=((maxR-minR)+maxRadius);
alignedData=newArray(0);
print(file, maxR);

for(i=0; i<steps; i++){
lineProfile=Array.slice(rawData, indBegin[i], indEnd[i]);
zeros1=newArray(maxR-boudaryRadius[i]);
zeros2=newArray(boudaryRadius[i]-minR);
Array.fill(zeros1,0);
Array.fill(zeros2,0);
lineProfile=Array.concat(zeros1,lineProfile);
lineProfile=Array.concat(lineProfile,zeros2);
alignedData=Array.concat(alignedData,lineProfile);

lineProfiledata="";
for(j=0;j<lineProfile.length;j++){
lineProfiledata=lineProfiledata+toString(lineProfile[j])+", ";
}
print(file,lineProfiledata);
}
```

```
File.close(file);
}

}

close();
}

function roiGeneratorML(file, dir) {
print("refining cell containing regions...");
path=replace(dir, "\\\\", "\\\\\\\\\\");
    des=replace(file, "_boxes.csv", "_ROI.zip");
    if(File.exists(path+des)) {
        print("File exists: "+ des);
        return des;
    }

action="open="+path+file;
    run("Results... ", action);
newImage("Untitled", "8-bit black", 2048, 2048, 1);
roiManager("reset");

for (i=0; i<nResults; i++){
xpos=getResult("C1",i);
ypos=getResult("C2",i);
width=getResult("C3",i);
height=getResult("C4",i);
makeRectangle(xpos, ypos, width, height);
    run("Add...", "value=7");
addOverlap();
}

roiClearUpTooSmall();
```

```
roiManager("save", dir+des);
return des;
close();
}

function addOverlap(){
roiManager("add");
roiManager("deselect")
roiNumber=roiManager("count");
if (roiNumber==1) return true;

last=roiNumber-1;
  for (j=0; j<roiNumber-1; j++){
    roiManager("select", newArray(j,last));
    roiManager("AND");
    if(selectionType()!=-1){
      roiManager("add");
      roiManager("deselect")
      roiManager("select", newArray(j,last));
      roiManager("delete");
      return true;
    }
  }
}
```

### B.1.5 Discard ROI's that are too small

```
function roiClearUpTooSmall(){
roiManager("deselect");
roiNumber=roiManager("count");
toClean = newArray();
```

```
for (j=0; j<roiNumber; j++){
roiManager("deselect");
roiManager("select",j);
getStatistics(area);
if (area <12000 ) toClean=Array.concat(toClean,j);
}
roiManager("deselect");
if(toClean.length!=0) {
roiManager("select",toClean);
roiManager("delete");
}
}
```

### B.1.6 Boundary detection of cell

```
function getCellROIfromSquares(ROIfileName,workingDir){
cells=replace(ROIfileName,"_ROI.zip","_cells.zip");
if(File.exists(workingDir+cells)) {
    print("File exists: "+ cells);
    return cells;
}
tiffName=replace(ROIfileName,"_ROI.zip",".tif");
open(workingDir+tiffName);
    roiManager("reset");
    roiManager("Open", workingDir+ROIfileName);
run("Subtract Background...", "rolling=50");
run("Find Edges");
run("Smooth");
run("Smooth");
guessingROIstart = roiManager("count");
squareROINumber=guessingROIstart;
for (i=0;i<squareROINumber;i++){
```

```
addSixteenGuessing(i);
cleanUpGuessingROI(guessingROIstart);
guessingROIstart=roiManager("count");
}
for (i=squareROINumber-1;i>=0;i--){
roiManager("deselect");
roiManager("select", i);
roiManager("delete");
}
roiManager("deselect");
if(roiManager("count")>0) roiManager("save", workingDir+cells);
close();
return cells;
}
```

```
function cleanUpGuessingROI(startROI){

lastROI=roiManager("count");
if(startROI==lastROI) return "Can't Guess";
    holder=startROI;
roundest=0;
for (i=startROI; i<lastROI; i++){
rd=calculateRoundness(i);
if (rd>roundest){
roundest=rd;
holder=i;
}
}
toDelete=newArray();
if(roundest<0.8) holder=0;
```

```
for (i=startROI; i<lastROI; i++){
  if (i!=holder) toDelete=Array.concat(toDelete,i);
}
roiManager("deselect");
roiManager("select", toDelete);
roiManager("delete");
}
```

### B.1.7 Discard non-circular shaped ROI's

```
function calculateRoundness(guessRoi){
  roiManager("deselect");
  roiManager("select", guessRoi);
  run("Set Measurements...", "area perimeter");
  run("Measure");
  area=getResult("Area");
  perimeter=getResult("Perim.");
  roundness= 4*3.14*area/(perimeter*perimeter);
  if (area < 2000) roundness = 0.01;
  return roundness;
}

function addSixteenGuessing(squareRoi){
  roiManager("deselect");
  roiManager("select", squareRoi);
  getSelectionBounds(x, y, width, height);
  roiManager("deselect");
  xMid=x+0.55*width; //shift to cover different angles
  yMid=y+0.5*height;
  for(xx=1; xx<5; xx++){
    for (yy=1; yy<5; yy++){
      xPos=x+width*xx/5;
      yPos=y+height*yy/5;
```

```
angle=atan2((yPos-yMid),(xPos-xMid));
addOneROIforCell(angle,xPos,yPos);
}
}
}
```

### B.1.8 Add selction to ROI manager

```
function addOneROIforCell(angle,xInit,yInit){
cellDiameterEst=120; //Maxium cell diameter in pixel
steps=150; // must be less than 200
angleIncrease= -2*PI/steps; // change sign to reverse scan direction
distanceArray=newArray(steps);
xcoord=newArray(steps);
ycoord=newArray(steps);
for(i=0; i<steps; i++){
x=xInit+cos(angle+i*angleIncrease)*cellDiameterEst;
y=yInit+sin(angle+i*angleIncrease)*cellDiameterEst;
makeLine(xInit, yInit, x, y);
profile = getProfile();
maxLocs= Array.findMaxima(profile, 10);
//might need to change if the maximum is less "obious")
if(i==0){
distanceArray[i]=maxLocs[0];
} else {
distMaxLoc=newArray(maxLocs.length);
for(j=0; j<maxLocs.length; j++){
distMaxLoc[j]=abs(distanceArray[i-1]-maxLocs[j]);
}
rank=Array.rankPositions(distMaxLoc);
distanceArray[i]= maxLocs[rank[0]];
}
}
```

```
xcoord[i]=xInit+cos(angle+i*angleIncrease)*distanceArray[i];
ycoord[i]=yInit+sin(angle+i*angleIncrease)*distanceArray[i];
}
makeSelection("polygon", xcoord,ycoord);
if(selectionType()!=-1) roiManager("Add");
}
```

## B.2 Identification of redundant cells in GFP channel

### ImageJ Macros

```
setBatchMode(true);

dataRestructuredDir=getDirectory("select the dir");
subDirs = getFileList(dataRestructuredDir);

for (i = 0; i < subDirs.length;i++){
subDir=subDirs[i];
if(endsWith(subDir,"/")){
subDir=replace(subDir,"/","")+"\\";
listofredundantROIs(dataRestructuredDir+subDir); //boundary based on GFP
}
}

print("All done!");

function listofredundantROIs(workingDir){
if(File.exists(workingDir+"redudant.csv")){
print (workingDir+"redudant.csv exists; skipping...");
return;
}

print("working on" + workingDir);
```

```
roiManager("reset");
mChDir=workingDir+"mCh\\";
opencellROI(mChDir,true); //also open an image file
definedbymCh=roiManager("count");
GFPDir=workingDir+"GFP\\";
opencellROI(GFPDir,false);
definedbyGFP=roiManager("count")-definedbymCh;
toCleanmCh=newArray();
toCleanGFP=newArray();

for (i=0;i<definedbymCh;i++){
for (j=0;j<definedbyGFP;j++){
mChROI=i;
GFPROI=j+definedbymCh;
roiManager("deselect");
roiManager("select", newArray(mChROI,GFPROI));
roiManager("AND");
    if(selectionType()!=-1){
        if(calculateRoundness(mChROI) >= calculateRoundness(GFPROI)){
            toCleanGFP=Array.concat(toCleanGFP,j);
        }
        else toCleanmCh=Array.concat(toCleanmCh,i);
    }
}
}

Array.print(toCleanmCh);
Array.print(toCleanGFP);

file=File.open(workingDir+"redundant.csv");
print(file,arrayToCSV(toCleanmCh));
```

```
        print(file,arrayToCSV(toCleanGFP));
File.close(file);
close();
}

function arrayToCSV(ar){
result="";
for(j=0;j<ar.length;j++){
result=result+toString(ar[j])+",";
}
return result;
}

function opencellROI(colourDir,openImageQ){
allFiles = getFileList(colourDir);
for (i = 0; i< allFiles.length;i++){
if(endsWith(allFiles[i],"cells.zip")){
roiManager("Open", colourDir+allFiles[i]);
}
if(openImageQ && endsWith(allFiles[i],"tif")){
open(colourDir+allFiles[i]);
}
}
}

function calculateRoundness(guessRoi){
roiManager("deselect");
roiManager("select", guessRoi);
run("Set Measurements...", "area perimeter");
run("Measure");
area=getResult("Area");
```

```

perimeter=getResult("Perim.");
roundness= 4*3.14*area/(perimeter*perimeter);
if (area < 2000) roundness = 0.01;
return roundness;
}

```

## B.3 Quantification of PIP<sub>3</sub>-Index

### B.3.1 File import

#### Mathematica Script

```

NotebookDirectory[] (ClearSystemCache[];)
(chopArray(ar_):=ar
[[1;;All,1;;min(Table[Length[i], {i, ar}]]])
((redundant=Import[NotebookDirectory[]
<>redundant.csv]//. → Sequence[;])
(notredundantQ(a_,sel_,red_):=
(redundantCases=Switch[sel,mCh,red[[1]],GFP,red[[2]]];
matching=False;For[i=1,
i≤ Length[redundantCases], i++,
matching=matching∨StringMatchQ[a,*cell_ <> ToString
[redundantCases[[i]]<>.csv];;-matching)))

```

### B.3.2 Cells defined by mCherry channel

**Mathematica Script** (definedBy=mCh;) (SetDirectory[NotebookDirectory[]<>profile\_boundary

### B.3.3 Cell profiles defined by mCherry channel

#### Mathematica Script

```

Table[ListDensityPlot[i,ColorFunction→
({x}f4a1RGBColor[0,x,0]),{i,dataGFPmCh}]
Table[ListDensityPlot[i,ColorFunction→

```

```
{x}f4a1RGBColor[x,0,0]],{i,datamChmCh}]
```

### B.3.4 Cells defined by GFP channel

#### Mathematica Script

```
definedBy=GFP;
SetDirectory[NotebookDirectory[]
<>profile_boundary_defined_by_<>definedBy];
```

### B.3.5 Cell profiles defined by GFP channel

#### Mathematica Script

```
Table[ListDensityPlot[i,ColorFunction->
({x}f4a1RGBColor[0,x,0]),{i,dataGFPGFP}]
Table[ListDensityPlot[i,ColorFunction->
({x}f4a1RGBColor[x,0,0]),{i,datamChGFP}]
```

### B.3.6 Identifying cells for quantification

#### Mathematica Script

```
Cells defined by GFP channel Mathematica Script select = ;
datamChmCh = datamChmCh[[select]];
boundaryPositionmChmCh = boundaryPositionmChmCh[[select]];
dataGFPmCh = dataGFPmCh[[select]];
boundaryPositionGFPmCh = boundaryPositionGFPmCh[[select]];
```

#### **Cells defined by GFP channel**

```
select = ;
dataGFPGFP = dataGFPGFP[[select]];
boundaryPositionGFPGFP = boundaryPositionGFPGFP[[select]];
datamChGFP = datamChGFP[[select]];
boundaryPositionmChGFP = boundaryPositionmChGFP[[select]];
```

#### **Final Images used for Quantification Mathematica Script**

```
Table[ListDensityPlot[i, ColorFunction -> Function[x, RGBColor[x, 0, 0]]], i,
Join[datamChmCh, datamChGFP]]
```

```
Table[ListDensityPlot[i, ColorFunction -> Function[x, RGBColor[0, x, 0]]], i,
Join[dataGFPmCh, dataGFPGFP]]
```

### B.3.7 Calculating *PIP*<sub>3</sub>-Index

#### Mathematica Script

```
meanListmChmCh = Table[Mean[i], i, datamChmCh[;;, 2 ;;]];
meanListGFPmCh = Table[Mean[i], i, dataGFPmCh2[;;, 2 ;;]];
meanListGFPGFP = Table[Mean[i], i, dataGFPGFP[;;, 2 ;;]];
meanListmChGFP = Table[Mean[i], i, datamChGFP2[;;, 2 ;;]];
(meanListGFP=Join[meanListGFPmCh,meanListGFPGFP];)
(meanListmCh=Join[meanListmChmCh,meanListmChGFP];)
(expNumber=Length[meanListmCh];)
Table[Show [ListPlot[{meanListGFP[[i]],meanListmCh[[i]]},
PlotStyle-> {Green, Red}], ListLinePlot  $\left[ \begin{pmatrix} \text{boundaryPosition}[[i]] & 0 \\ \text{boundaryPosition}[[i]] & 4095 \end{pmatrix} \right.$ ,
PlotStyle-> Blue, {i, expNumber}
ratios=Table  $\left[ \frac{\text{meanListmCh}[[i,1;;i[[i]]]]}{\text{meanListGFP}[[i,1;;i[[i]]]]} \right.$ ,
{i,1,Length[meanListGFP]};
{ } Table[Show [{ListPlot[ratios[[i]],
ListLinePlot  $\left[ \begin{pmatrix} \text{boundaryPosition}[[i]] & 0 \\ \text{boundaryPosition}[[i]] & 4095 \end{pmatrix} \right.$ ,
PlotStyle-> Pink, ListLinePlot  $\left[ \begin{pmatrix} \text{boundaryPosition}[[i]] - 10 & 0 \\ \text{boundaryPosition}[[i]] - 10 & 4095 \end{pmatrix} \right.$ ,
PlotStyle-> Green, {i, expNumber}
finalRatio(datax_,boundaryData_):=
If[datax[[boundaryData - 2]] ≥ datax[[boundaryData - 10]],
 $\frac{\max(\text{datax}[[\text{boundaryData}-10;;\text{boundaryData}]]}{\min(\text{datax}[[\text{boundaryData}-10;;\text{boundaryData}]]} ,$ 
 $\frac{\min(\text{datax}[[\text{boundaryData}-10;;\text{boundaryData}]]}{\max(\text{datax}[[\text{boundaryData}-10;;\text{boundaryData}]]}$ 
boundaryPosition[[i]],{i,1,Length[ratios]})
```

# Bibliography

- [1] Amparo Andrés-Pons et al. “<em>In vivo</em> Functional Analysis of the Counterbalance of Hyperactive Phosphatidylinositol 3-Kinase p110 Catalytic Oncoproteins by the Tumor Suppressor PTEN”. In: *Cancer Research* 67.20 (Oct. 2007), 9731 LP –9739. URL: <http://cancerres.aacrjournals.org/content/67/20/9731.abstract>.
- [2] Anjon Audhya, Michelangelo Foti, and Scott D. Emr. “Distinct Roles for the Yeast Phosphatidylinositol 4-Kinases, Stt4p and Pik1p, in Secretion, Cell Growth, and Organelle Membrane Dynamics”. In: *Molecular Biology of the Cell* 11.8 (2000). PMID: 10930462, pp. 2673–2689. DOI: 10.1091/mbc.11.8.2673. eprint: <https://doi.org/10.1091/mbc.11.8.2673>. URL: <https://doi.org/10.1091/mbc.11.8.2673>.
- [3] Anjon Audhya et al. “Genome-wide lethality screen identifies new PI4,5P2 effectors that regulate the actin cytoskeleton”. eng. In: *The EMBO journal* 23.19 (2004), pp. 3747–3757. ISSN: 0261-4189. DOI: 10.1038/sj.emboj.7600384. URL: <https://www.ncbi.nlm.nih.gov/pubmed/15372071><https://www.ncbi.nlm.nih.gov/pmc/PMC522789/>.
- [4] F. a. Barr. “Rab GTPases and membrane identity: Causal or inconsequential?”. In: *The Journal of Cell Biology* 202.2 (2013), pp. 191–199. ISSN: 0021-9525. DOI: 10.1083/jcb.201306010. URL: <http://www.jcb.org/cgi/doi/10.1083/jcb.201306010>.
- [5] Serrano L. Becskei A1, Séraphin B. “Positive feedback in eukaryotic gene networks : cell differentiation by graded to binary response conversion”. In: *The EMBO journal* 20.10 (2001), pp. 2528–2535.

- [6] Carolyn A Beeton et al. “Comparison of the kinetic properties of the lipid- and protein-kinase activities of the p110alpha and p110beta catalytic subunits of class-Ia phosphoinositide 3-kinases.” In: *The Biochemical journal* 350 Pt 2 (2000), pp. 353–359. ISSN: 02646021. DOI: 10.1042/0264-6021:3500353.
- [7] P J Belde et al. “Inositol 1,4,5-trisphosphate releases Ca<sup>2+</sup> from vacuolar membrane vesicles of *Saccharomyces cerevisiae*.” eng. In: *FEBS letters* 323.1-2 (May 1993), pp. 113–118. ISSN: 0014-5793 (Print).
- [8] Felipe O Bendezu and Sophie G Martin. “Cdc42 explores the cell periphery for mate selection in fission yeast.” eng. In: *Current biology : CB* 23.1 (Jan. 2013), pp. 42–47. ISSN: 1879-0445 (Electronic). DOI: 10.1016/j.cub.2012.10.042.
- [9] Marc R Birtwistle et al. “Emergence of bimodal cell population responses from the interplay between analog single-cell signaling and protein expression noise.” eng. In: *BMC systems biology* 6 (Aug. 2012), p. 109. ISSN: 1752-0509 (Electronic). DOI: 10.1186/1752-0509-6-109.
- [10] Cecilia J Bonangelino et al. “Osmotic stress-induced increase of phosphatidylinositol 3,5-bisphosphate requires Vac14p, an activator of the lipid kinase Fab1p”. eng. In: *The Journal of cell biology* 156.6 (Mar. 2002), pp. 1015–1028. ISSN: 0021-9525. DOI: 10.1083/jcb.200201002. URL: <https://www.ncbi.nlm.nih.gov/pubmed/11889142><https://www.ncbi.nlm.nih.gov/pmc/PMC2173454/>.
- [11] James R. Brown and Kurt R. Auger. “Phylogenomics of phosphoinositide lipid kinases: Perspectives on the evolution of second messenger signaling and drug discovery”. In: *BMC Evolutionary Biology* 11.1 (2011), p. 4. ISSN: 14712148. DOI: 10.1186/1471-2148-11-4. URL: <http://www.biomedcentral.com/1471-2148/11/4>.
- [12] Patricie Burda et al. “Retromer function in endosome-to-Golgi retrograde transport is regulated by the yeast Vps34 PtdIns 3-kinase”. In: *Journal of Cell Science* 115.20 (2002), pp. 3889–3900. ISSN: 0021-9533. DOI: 10.1242/jcs.00090. URL: <http://jcs.biologists.org/content/115/20/3889>.

- [13] Nick Callamaras and Ian Parker. “Phasic characteristic of elementary Ca<sup>2+</sup> release sites underlies quantal responses to IP<sup>3</sup>”. In: 19.14 (2000).
- [14] Robert B Campbell, Fenghua Liu, and Alonzo H Ross. “Allosteric Activation of PTEN Phosphatase by Phosphatidylinositol 4,5-Bisphosphate”. In: *Journal of Biological Chemistry* 278.36 (2003), pp. 33617–33620. DOI: 10.1074/jbc.C300296200. URL: <http://www.jbc.org/content/278/36/33617.abstract>.
- [15] P J Casey. “Biochemistry of protein prenylation.” In: *Journal of lipid research* 33.12 (1992), pp. 1731–1740. ISSN: 0022-2275.
- [16] Dong-eun Chang et al. “Building biological memory by linking positive feedback loops”. In: 107.1 (2010), pp. 175–180. DOI: 10.1073/pnas.0908314107.
- [17] Angela H. Chau et al. “Designing synthetic regulatory networks capable of self-organizing cell polarization”. In: *Cell* 151.2 (2012), pp. 320–332. ISSN: 00928674. DOI: 10.1016/j.cell.2012.08.040. URL: <http://dx.doi.org/10.1016/j.cell.2012.08.040>.
- [18] Jiawen Chen and Yinghao Wu. “Understanding the Functional Roles of Multiple Extracellular Domains in Cell Adhesion Molecules with a Coarse-Grained Model”. In: *Journal of molecular biology* 429.7 (Apr. 2017), pp. 1081–1095. ISSN: 1089-8638. DOI: 10.1016/j.jmb.2017.02.013. URL: <https://www.ncbi.nlm.nih.gov/pubmed/28237680><https://www.ncbi.nlm.nih.gov/pmc/PMC5989558/>.
- [19] Jian-Geng Chiou et al. “Principles that govern competition or co-existence in Rho-GTPase driven polarization”. In: *PLOS Computational Biology* 14.4 (2018), pp. 1–23. DOI: 10.1371/journal.pcbi.1006095. URL: <https://doi.org/10.1371/journal.pcbi.1006095>.
- [20] Edwin Choy et al. “Endomembrane trafficking of ras: The CAAX motif targets proteins to the ER and Golgi”. In: *Cell* 98.1 (1999), pp. 69–80. ISSN: 00928674. DOI: 10.1016/S0092-8674(00)80607-8.

- [21] Dominique Chu et al. “Translation elongation can control translation initiation on eukaryotic mRNAs.” eng. In: *The EMBO journal* 33.1 (Jan. 2014), pp. 21–34. ISSN: 1460-2075 (Electronic). DOI: 10.1002/embj.201385651.
- [22] Perla Del Conte-zerial et al. “Membrane identity and GTPase cascades regulated by toggle and cut-out switches”. In: 206 (2008), pp. 1–9. DOI: 10.1038/msb.2008.45.
- [23] F T Cooke et al. “The stress-activated phosphatidylinositol 3-phosphate 5-kinase Fab1p is essential for vacuole function in *S. cerevisiae*.” eng. In: *Current biology : CB* 8.22 (Nov. 1998), pp. 1219–1222. ISSN: 0960-9822 (Print).
- [24] Elodie Couplan et al. “Polyunsaturated fatty acids inhibit PI3K activity in a yeast-based model system”. In: *Biotechnology Journal* 4.8 (2009), pp. 1190–1197. ISSN: 18606768. DOI: 10.1002/biot.200800229.
- [25] Scott M Coyle et al. “Mapping the functional versatility and fragility of Ras GTPase signaling circuits through in vitro network reconstitution”. In: (2016), pp. 1–34. DOI: 10.7554/eLife.12435.
- [26] Jayajit Das et al. “Digital signaling and hysteresis characterize ras activation in lymphoid cells”. In: *Cell* 136.2 (Jan. 2009), pp. 337–351. ISSN: 1097-4172. DOI: 10.1016/j.cell.2008.11.051. URL: <https://www.ncbi.nlm.nih.gov/pubmed/19167334><https://www.ncbi.nlm.nih.gov/pmc/PMC2662698/>.
- [27] Richard Day and Micheal Davidson. “NIH Public Access”. In: *Online* 366.5 (2007), pp. 1772–1775. DOI: 10.1039/b901966a.The.
- [28] Douglas J Demarini, Edward M Carlin, and George P Livi. “Constitutive promoter modules for PCR-based gene modification in *Saccharomyces cerevisiae*”. In: (2001), pp. 723–728.
- [29] S K Dove et al. “Osmotic stress activates phosphatidylinositol-3,5-bisphosphate synthesis.” eng. In: *Nature* 390.6656 (Nov. 1997), pp. 187–192. ISSN: 0028-0836 (Print). DOI: 10.1038/36613.
- [30] David G Drubin and W James Nelson. “Origins of Cell Polarity Review”. In: 84 (1996), pp. 335–344.

- [31] Jem A Efe, Roberto J Botelho, and Scott D Emr. “Atg18 regulates organelle morphology and Fab1 kinase activity independent of its membrane recruitment by phosphatidylinositol 3,5-bisphosphate.” eng. In: *Molecular biology of the cell* 18.11 (Nov. 2007), pp. 4232–4244. ISSN: 1059-1524 (Print). DOI: 10.1091/mbc.e07-04-0301.
- [32] Amir Erez et al. “Modeling of cytometry data in logarithmic space: When is a bimodal distribution not bimodal?” In: *Cytometry Part A* 93.6 (June 2018), pp. 611–619. ISSN: 1552-4922. DOI: 10.1002/cyto.a.23333. URL: <https://doi.org/10.1002/cyto.a.23333>.
- [33] Frank Faulhammer et al. “Growth control of Golgi phosphoinositides by reciprocal localization of sac1 lipid phosphatase and pik1 4-kinase.” eng. In: *Traffic (Copenhagen, Denmark)* 8.11 (Nov. 2007), pp. 1554–1567. ISSN: 1398-9219 (Print). DOI: 10.1111/j.1600-0854.2007.00632.x.
- [34] Teresa Fernandez-Acero et al. “A yeast-based in vivo bioassay to screen for class i phosphatidylinositol 3-kinase specific inhibitors”. In: *Journal of Biomolecular Screening* 17.8 (2012), pp. 1018–1029. ISSN: 10870571. DOI: 10.1177/1087057112450051.
- [35] Teresa Fernandez-Acero et al. “The yeast cell wall integrity pathway signals from recycling endosomes upon elimination of phosphatidylinositol (4,5)-bisphosphate by mammalian phosphatidylinositol 3-kinase”. In: *Cellular Signaling* 27.11 (2015), pp. 2272–2284. ISSN: 18733913. DOI: 10.1016/j.cellsig.2015.08.004. URL: <http://dx.doi.org/10.1016/j.cellsig.2015.08.004>.
- [36] Sebastiano De Franciscis and Alberto D Onofrio. “Cellular polarization: Interaction between extrinsic bounded noises and the wave-pinning mechanism”. In: (2013). DOI: 10.1103/PhysRevE.88.032709. arXiv: arXiv:1212.4996v1.
- [37] Tanya S Freedman et al. “A Ras-induced conformational switch in the Ras activator Son of sevenless”. In: *Proceedings of the National Academy of Sciences of the United States of America* 103.45 (Nov. 2006), pp. 16692–16697. ISSN: 0027-8424. DOI: 10.1073/pnas.0608127103. URL: <https://www.ncbi>.

- nlm.nih.gov/pubmed/17075039%20https://www.ncbi.nlm.nih.gov/pmc/PMC1629002/.
- [38] Jonathan B. Freeman and Rick Dale. “Assessing bimodality to detect the presence of a dual cognitive process”. In: *Behavior Research Methods* 45.1 (Mar. 2013), pp. 83–97. ISSN: 1554-3528. DOI: 10.3758/s13428-012-0225-x. URL: <https://doi.org/10.3758/s13428-012-0225-x>.
- [39] P Garcia et al. “The pleckstrin homology domain of phospholipase C-delta 1 binds with high affinity to phosphatidylinositol 4,5-bisphosphate in bilayer membranes.” eng. In: *Biochemistry* 34.49 (Dec. 1995), pp. 16228–16234. ISSN: 0006-2960 (Print).
- [40] Maria F. Garcia-Parajo et al. “Nanoclustering as a dominant feature of plasma membrane organization”. In: *Journal of Cell Science* 127.23 (2014), pp. 4995–5005. ISSN: 0021-9533. DOI: 10.1242/jcs.146340. eprint: <http://jcs.biologists.org/content/127/23/4995.full.pdf>. URL: <http://jcs.biologists.org/content/127/23/4995>.
- [41] Timothy S Gardner, Charles R Cantor, and James J Collins. “Construction of a genetic toggle switch in *Escherichia coli*”. In: *Nature* 403.6767 (Jan. 2000), pp. 339–342. ISSN: 0028-0836. URL: [http://dx.doi.org/10.1038/35002131%20http://www.nature.com/nature/journal/v403/n6767/supinfo/403339a0%7B%5C\\_%7DS1.html](http://dx.doi.org/10.1038/35002131%20http://www.nature.com/nature/journal/v403/n6767/supinfo/403339a0%7B%5C_%7DS1.html).
- [42] Anabel Gil et al. “A functional dissection of PTEN N-terminus: implications in PTEN subcellular targeting and tumor suppressor activity”. eng. In: *PloS one* 10.4 (Apr. 2015), e0119287–e0119287. ISSN: 1932-6203. DOI: 10.1371/journal.pone.0119287. URL: <https://www.ncbi.nlm.nih.gov/pubmed/25875300%20https://www.ncbi.nlm.nih.gov/pmc/articles/PMC4398541/>.
- [43] D J Gillooly et al. “Localization of phosphatidylinositol 3-phosphate in yeast and mammalian cells.” eng. In: *The EMBO journal* 19.17 (2000), pp. 4577–4588. ISSN: 0261-4189 (Print). DOI: 10.1093/emboj/19.17.4577.

- [44] Andrew B Goryachev and Marcin Leda. “Many roads to symmetry breaking: molecular mechanisms and theoretical models of yeast cell polarity”. In: *Molecular biology of the cell* 28.3 (2017), pp. 370–380. ISSN: 1939-4586. DOI: 10.1091/mbc.E16-10-0739. URL: <https://www.ncbi.nlm.nih.gov/pubmed/28137950><https://www.ncbi.nlm.nih.gov/pmc/PMC5341721/>.
- [45] Isabelle Guillas et al. “Phosphatidylinositol 4,5-bisphosphate is required for invasive growth in *Saccharomyces cerevisiae*”. In: *Journal of Cell Science* 126.16 (2013), pp. 3602–3614. ISSN: 0021-9533. DOI: 10.1242/jcs.122606. URL: <http://jcs.biologists.org/content/126/16/3602>.
- [46] Hiroko Hama, Jon Y Takemoto, and Daryll B Dewald. “Analysis of Phosphoinositides in Protein Trafficking”. In: 473 (2000), pp. 465–473. DOI: 10.1006/meth.2000.0959.
- [47] John F. HANCOCK and Robert G. PARTON. “Ras plasma membrane signalling platforms”. In: *Biochemical Journal* 389.1 (2005), pp. 1–11. ISSN: 0264-6021. DOI: 10.1042/BJ20050231. eprint: <http://www.biochemj.org/content/389/1/1.full.pdf>. URL: <http://www.biochemj.org/content/389/1/1>.
- [48] J A Hartigan and P M Hartigan. “The Dip Test of Unimodality”. In: *The Annals of Statistics* 13.1 (1985), pp. 70–84.
- [49] Benjamin D Hopkins et al. “PTEN function: the long and the short of it”. *eng*. In: *Trends in biochemical sciences* 39.4 (Apr. 2014), pp. 183–190. ISSN: 0968-0004. DOI: 10.1016/j.tibs.2014.02.006. URL: <https://www.ncbi.nlm.nih.gov/pubmed/24656806><https://www.ncbi.nlm.nih.gov/pmc/articles/PMC4043120/>.
- [50] Audrey S Howell et al. “Negative feedback enhances robustness in the yeast polarity establishment circuit”. In: *Cell* 149.2 (Apr. 2012), pp. 322–333. ISSN: 1097-4172. DOI: 10.1016/j.cell.2012.03.012. URL: <https://www.ncbi.nlm.nih.gov/pubmed/22500799><https://www.ncbi.nlm.nih.gov/pmc/PMC3680131/>.

- [51] Chieh Hsu et al. “Protein Dimerization Generates Bistability in Report Protein Dimerization Generates Bistability in Positive Feedback Loops”. In: *Cell-Reports* (2016), pp. 1–7. ISSN: 2211-1247. DOI: 10.1016/j.celrep.2016.06.072. URL: <http://dx.doi.org/10.1016/j.celrep.2016.06.072>.
- [52] Chieh Hsu et al. “Protein Dimerization Generates Bistability in Report Protein Dimerization Generates Bistability in Positive Feedback Loops”. In: *Cell-Reports* (2016), pp. 1–7. ISSN: 2211-1247. DOI: 10.1016/j.celrep.2016.06.072. URL: <http://dx.doi.org/10.1016/j.celrep.2016.06.072>.
- [53] Chieh Hsu et al. “Stochastic signalling rewires the interaction map of a multiple feedback network during yeast evolution.” In: *Nature Communications* 3 (2012), p. 682. ISSN: 2041-1723. DOI: 10.1038/ncomms1687. URL: <http://eutils.ncbi.nlm.nih.gov/entrez/eutils/elink.fcgi?dbfrom=pubmed%7B%5C%7Ddid=22353713%7B%5C%7Dretmode=ref%7B%5C%7Dcmd=prlinks%7B%5C%7D5Cnpapers3://publication/uuid/238A08DB-B7B0-418B-8DEF-D0D855D1EAE5>.
- [54] Steven J Isakoff et al. “Identification and analysis of PH domain-containing targets of phosphatidylinositol 3-kinase using a novel in vivo assay in yeast”. In: 17.18 (1998), pp. 5374–5387.
- [55] Steve Jean and Amy A Kiger. “Classes of phosphoinositide 3-kinases at a glance”. In: *Journal of Cell Science* 127.5 (Mar. 2014), pp. 923–928. ISSN: 0021-9533. DOI: 10.1242/jcs.093773. URL: <http://www.ncbi.nlm.nih.gov/pmc/articles/PMC3937771/>.
- [56] Ben Klünder et al. “GDI-Mediated Cell Polarization in Yeast Provides Precise Spatial and Temporal Control of Cdc42 Signaling”. In: *PLoS Computational Biology* 9.12 (2013), e1003396. ISSN: 1553-7358. DOI: 10.1371/journal.pcbi.1003396. URL: <http://dx.plos.org/10.1371/journal.pcbi.1003396>.
- [57] Aneta Koseska. “Cell signaling as a cognitive process”. In: *The EMBO Journal* (2017), pp. 1–15. DOI: 10.15252/embj.201695383.

- [58] Michael S Kuhns and Mark M Davis. “Disruption of extracellular interactions impairs T cell receptor-CD3 complex stability and signaling.” eng. In: *Immunity* 26.3 (Mar. 2007), pp. 357–369. ISSN: 1074-7613 (Print). DOI: 10.1016/j.immuni.2007.01.015.
- [59] Akihiro Kusumi et al. “Hierarchical mesoscale domain organization of the plasma membrane”. In: *Trends in Biochemical Sciences* 36.11 (2011), pp. 604–615. ISSN: 09680004. DOI: 10.1016/j.tibs.2011.08.001. URL: <http://dx.doi.org/10.1016/j.tibs.2011.08.001>.
- [60] M Laurent and N Kellershohn. “Multistability: a major means of differentiation and evolution in biological systems.” eng. In: *Trends in biochemical sciences* 24.11 (Nov. 1999), pp. 418–422. ISSN: 0968-0004 (Print).
- [61] Anita T Layton et al. “Modeling vesicle traffic reveals unexpected consequences for Cdc42p-mediated polarity establishment”. In: *Current biology : CB* 21.3 (2011), pp. 184–194. ISSN: 1879-0445. DOI: 10.1016/j.cub.2011.01.012. URL: <https://www.ncbi.nlm.nih.gov/pubmed/21277209><https://www.ncbi.nlm.nih.gov/pmc/PMC3052744/>.
- [62] David E Levin. “Cell wall integrity signaling in *Saccharomyces cerevisiae*”. eng. In: *Microbiology and molecular biology reviews : MMBR* 69.2 (June 2005), pp. 262–291. ISSN: 1092-2172. DOI: 10.1128/MMBR.69.2.262-291.2005. URL: <https://www.ncbi.nlm.nih.gov/pubmed/15944456><https://www.ncbi.nlm.nih.gov/pmc/PMC1197416/>.
- [63] Björn F. Lillemeier et al. “Plasma membrane-associated proteins are clustered into islands attached to the cytoskeleton”. In: *Proceedings of the National Academy of Sciences* 103.50 (2006), pp. 18992–18997. ISSN: 0027-8424. DOI: 10.1073/pnas.0609009103. eprint: <https://www.pnas.org/content/103/50/18992.full.pdf>. URL: <https://www.pnas.org/content/103/50/18992>.
- [64] Stella M. Lu and Gregory D. Fairn. “Mesoscale organization of domains in the plasma membrane – beyond the lipid raft”. In: *Critical Reviews in Biochemistry and Molecular Biology* 53.2 (2018). PMID: 29457544, pp. 192–207. DOI: 10.1080/10409238.2018.1436515. eprint: <https://doi.org/10.1080/>

- 10409238.2018.1436515. URL: <https://doi.org/10.1080/10409238.2018.1436515>.
- [65] Satomi Matsuoka and Masahiro Ueda. “Mutual inhibition between PTEN and PIP3 generates bistability for polarity in motile cells”. In: *Nature Communications* 9.1 (2018), p. 4481. ISSN: 2041-1723. DOI: 10.1038/s41467-018-06856-0. URL: <https://doi.org/10.1038/s41467-018-06856-0>.
- [66] R Scott McIsaac et al. “Fast-acting and nearly gratuitous induction of gene expression and protein depletion in *Saccharomyces cerevisiae*.” eng. In: *Molecular biology of the cell* 22.22 (Nov. 2011), pp. 4447–4459. ISSN: 1939-4586 (Electronic). DOI: 10.1091/mbc.E11-05-0466.
- [67] Taylor L Mighell, Sara Evans-Dutson, and Brian J O’Roak. “A Saturation Mutagenesis Approach to Understanding PTEN Lipid Phosphatase Activity and Genotype-Phenotype Relationships”. eng. In: *American journal of human genetics* 102.5 (May 2018), pp. 943–955. ISSN: 1537-6605. DOI: 10.1016/j.ajhg.2018.03.018. URL: <https://www.ncbi.nlm.nih.gov/pubmed/29706350>20<https://www.ncbi.nlm.nih.gov/pmc/articles/PMC5986715/>.
- [68] Prasenjit Mitra et al. “A novel phosphatidylinositol(3,4,5)P3 pathway in fission yeast”. In: *The Journal of Cell Biology* 166.2 (2004), pp. 205–211. ISSN: 0021-9525. DOI: 10.1083/jcb.200404150. URL: <http://jcb.rupress.org/content/166/2/205>.
- [69] Alexander Y Mitrophanov and Eduardo A Groisman. “Positive feedback in cellular control systems”. In: *BioEssays* 30.6 (2008), pp. 542–555.
- [70] Yoichiro Mori, Alexandra Jilkine, and Leah Edelstein-Keshet. “Wave-Pinning and Cell Polarity from a Bistable Reaction-Diffusion System”. In: *Biophysical Journal* 94.9 (2008), pp. 3684–3697. ISSN: 0006-3495. DOI: <https://doi.org/10.1529/biophysj.107.120824>. URL: <http://www.sciencedirect.com/science/article/pii/S0006349508704442>.
- [71] Kotaro Nakanishi et al. “Structure of yeast Argonaute with guide RNA.” eng. In: *Nature* 486.7403 (June 2012), pp. 368–374. ISSN: 1476-4687 (Electronic). DOI: 10.1038/nature11211.

- [72] Garth L Nicolson. “Biochimica et Biophysica Acta The Fluid — Mosaic Model of Membrane Structure : Still relevant to understanding the structure , function and dynamics of biological membranes after more than 40 years ”. In: *BBA - Biomembranes* 1838.6 (2014), pp. 1451–1466. ISSN: 0005-2736. DOI: 10.1016/j.bbamem.2013.10.019. URL: <http://dx.doi.org/10.1016/j.bbamem.2013.10.019>.
- [73] Takeshi Noda. “Regulation of Autophagy through TORC1 and mTORC1”. eng. In: *Biomolecules* 7.3 (July 2017), p. 52. ISSN: 2218-273X. DOI: 10.3390/biom7030052. URL: <https://www.ncbi.nlm.nih.gov/pubmed/28686223%20https://www.ncbi.nlm.nih.gov/pmc/PMC5618233/>.
- [74] Tomoko Okada and Toshihiko Ogura. “Nanoscale imaging of the adhesion core including integrin  $\beta$ 1 on intact living cells using scanning electron-assisted dielectric-impedance microscopy”. In: *PLOS ONE* 13.9 (Sept. 2018), e0204133. URL: <https://doi.org/10.1371/journal.pone.0204133>.
- [75] D Oliver et al. “Insights into the pathological mechanisms of p85  $\alpha$  mutations using a yeast-based phosphatidylinositol 3-kinase model”. In: 0 (2017), pp. 1–14. DOI: 10.1042/BSR20160258.
- [76] Mikiya Otsuji et al. “A Mass Conserved Reaction–Diffusion System Captures Properties of Cell Polarity”. In: *PLOS Computational Biology* 3.6 (2007), pp. 1–15. DOI: 10.1371/journal.pcbi.0030108. URL: <https://doi.org/10.1371/journal.pcbi.0030108>.
- [77] Pilar Perez and Teresa M Calonge. “Yeast Protein Kinase C”. In: *The Journal of Biochemistry* 132.4 (2002), pp. 513–517. ISSN: 0021-924X. DOI: 10.1093/oxfordjournals.jbchem.a003250. URL: <https://doi.org/10.1093/oxfordjournals.jbchem.a003250>.
- [78] Héloïse Philippon, Céline Brochier-Armanet, and Guy Perrière. “Evolutionary history of phosphatidylinositol- 3-kinases: ancestral origin in eukaryotes and complex duplication patterns”. eng. In: *BMC evolutionary biology* 15 (Oct. 2015), p. 226. ISSN: 1471-2148. DOI: 10.1186/s12862-015-0498-7. URL:

- <https://www.ncbi.nlm.nih.gov/pubmed/26482564><https://www.ncbi.nlm.nih.gov/pmc/articles/PMC4617754/>.
- [79] Beatrice Ramm, Tamara Heermann, and Petra Schwille. “The E. coli MinCDE system in the regulation of protein patterns and gradients”. In: *Cellular and Molecular Life Sciences* (July 2019). ISSN: 1420-9071. DOI: 10.1007/s00018-019-03218-x. URL: <https://doi.org/10.1007/s00018-019-03218-x>.
- [80] Brandon S. Razooky et al. “Nonlatching positive feedback enables robust bimodality by decoupling expression noise from the mean”. In: *PLOS Biology* 15.10 (Oct. 2017), pp. 1–26. DOI: 10.1371/journal.pbio.2000841. URL: <https://doi.org/10.1371/journal.pbio.2000841>.
- [81] Jochen Rink et al. “Rab Conversion as a Mechanism of Progression from Early to Late Endosomes”. In: *Cell* 122.5 (2005), pp. 735–749. ISSN: 00928674. DOI: 10.1016/j.cell.2005.06.043. URL: <http://linkinghub.elsevier.com/retrieve/pii/S0092867405006975>.
- [82] Isabel Rodriguez-Escudero et al. “Heterologous mammalian Akt disrupts plasma membrane homeostasis by taking over TORC2 signaling in *Saccharomyces cerevisiae*”. In: *Scientific Reports* 8 (May 2018), p. 7732. ISSN: 2045-2322. DOI: 10.1038/s41598-018-25717-w. URL: <http://www.ncbi.nlm.nih.gov/pmc/articles/PMC5955888/>.
- [83] Isabel Rodriguez-Escudero et al. “PI3K-dependent activation of mammalian PKB/AKT in *S. cerevisiae*: An in vivo model for the functional study of AKT mutants”. In: *Journal of Biological Chemistry* 3.11 (2009). DOI: 10.1074/jbc.M807867200.
- [84] Isabel Rodriguez-Escudero et al. “Reconstitution of the mammalian PI3K/PTEN/Akt pathway in yeast”. In: *Biochemical Journal* 390.2 (2005), pp. 613–623. ISSN: 0264-6021. DOI: 10.1042/BJ20050574. URL: <http://biochemj.org/lookup/doi/10.1042/BJ20050574>.
- [85] Isabel Rodriguez-Escudero et al. “Yeast-based methods to assess PTEN phosphoinositide phosphatase activity in vivo”. In: *Methods* 77 (2015), pp. 172–179. ISSN: 10959130. DOI: 10.1016/j.ymeth.2014.10.020.

- [86] Pauline Schaap. “Evolutionary crossroads in developmental biology: Dictyostelium discoideum”. eng. In: *Development (Cambridge, England)* 138.3 (Feb. 2011), pp. 387–396. ISSN: 1477-9129. DOI: 10.1242/dev.048934. URL: <https://www.ncbi.nlm.nih.gov/pubmed/21205784><https://www.ncbi.nlm.nih.gov/pmc/articles/PMC3014629/>.
- [87] R Schafer and Jasper Rine. “Protein Prenylation: Genes, Enzymes, Targets, and Function”. In: *Annu. Rev. Genet.* 30 (1992), pp. 209–37. ISSN: 1554-8929. DOI: 10.1021/cb500791f.
- [88] Wei Sha et al. “Hysteresis drives cell-cycle transitions in *Xenopus laevis* egg extracts”. In: *Proceedings of the National Academy of Sciences* 100.3 (2003), pp. 975–980. ISSN: 0027-8424. DOI: 10.1073/pnas.0235349100. URL: <https://www.pnas.org/content/100/3/975>.
- [89] Che-Chi Shu et al. “Bistability versus bimodal distributions in gene regulatory processes from population balance.” eng. In: *PLoS computational biology* 7.8 (Aug. 2011), e1002140. ISSN: 1553-7358 (Electronic). DOI: 10.1371/journal.pcbi.1002140.
- [90] Birte Sönnichsen et al. “Distinct membrane domains on endosomes in the recycling pathway visualized by multicolor imaging of Rab4, Rab5, and Rab11”. In: *Journal of Cell Biology* 149.4 (2000), pp. 901–913. ISSN: 00219525. DOI: 10.1083/jcb.149.4.901.
- [91] Christopher J Stefan, Anjon Audhya, and Scott D Emr. “The Yeast Synaptojanin-like Proteins Control the Cellular Distribution of Phosphatidylinositol ( 4 , 5 ) -Bisphosphate”. In: 13.February (2002), pp. 542–557. DOI: 10.1091/mbc.01.
- [92] Thomas Strahl and Jeremy Thorner. “Synthesis and function of membrane phosphoinositides in budding yeast, *Saccharomyces cerevisiae*”. eng. In: *Biochimica et biophysica acta* 1771.3 (Mar. 2007), pp. 353–404. ISSN: 0006-3002. DOI: 10.1016/j.bbaliip.2007.01.015. URL: <https://www.ncbi.nlm.nih.gov/pubmed/17382260><https://www.ncbi.nlm.nih.gov/pmc/PMC1868553/>.

- [93] Witold K. Subczynski and Akihiro Kusumi. “Dynamics of raft molecules in the cell and artificial membranes: approaches by pulse EPR spin labeling and single molecule optical microscopy”. In: *Biochimica et Biophysica Acta (BBA) - Biomembranes* 1610.2 (2003). Cholesterol-Rich Domains, pp. 231–243. ISSN: 0005-2736. DOI: [https://doi.org/10.1016/S0005-2736\(03\)00021-X](https://doi.org/10.1016/S0005-2736(03)00021-X). URL: <http://www.sciencedirect.com/science/article/pii/S000527360300021X>.
- [94] Carter J Swanson et al. “Calcium Stimulates Self-Assembly of Protein Kinase C  $\alpha$  In Vitro”. eng. In: *PloS one* 11.10 (Oct. 2016), e0162331–e0162331. ISSN: 1932-6203. DOI: 10.1371/journal.pone.0162331. URL: <https://www.ncbi.nlm.nih.gov/pubmed/27706148><https://www.ncbi.nlm.nih.gov/pmc/articles/PMC5051681/>.
- [95] Barry J Thompson. “Cell polarity: models and mechanisms from yeast, worms and flies”. In: *Development* 140.1 (2013), pp. 13–21. ISSN: 0950-1991. DOI: 10.1242/dev.083634. URL: <https://dev.biologists.org/content/140/1/13>.
- [96] P Varnai and T Balla. “Visualization of phosphoinositides that bind pleckstrin homology domains: calcium- and agonist-induced dynamic changes and relationship to myo-[ $^3$ H]inositol-labeled phosphoinositide pools.” eng. In: *The Journal of cell biology* 143.2 (Oct. 1998), pp. 501–510. ISSN: 0021-9525 (Print). DOI: 10.1083/jcb.143.2.501.
- [97] Anthony G Vecchiarelli et al. “Membrane-bound MinDE complex acts as a toggle switch that drives Min oscillation coupled to cytoplasmic depletion of MinD.” eng. In: *Proceedings of the National Academy of Sciences of the United States of America* 113.11 (Mar. 2016), E1479–88. ISSN: 1091-6490 (Electronic). DOI: 10.1073/pnas.1600644113.
- [98] Georg R Walther et al. “Deterministic versus stochastic cell polarisation through wave-pinning.” In: *Bulletin of mathematical biology* 74.11 (2012), pp. 2570–99. ISSN: 1522-9602. DOI: 10.1007/s11538-012-9766-5. URL: <http://www.pubmedcentral.nih.gov/articlerender.fcgi?artid=3480592%7B%5C%7Dtool=pmcentrez%7B%5C%7Drendertype=abstract>.

- [99] Roland Wedlich-Soldner et al. “Robust cell polarity is a dynamic state established by coupling transport and GTPase signaling”. In: *The Journal of cell biology* 166.6 (2004), pp. 889–900. ISSN: 0021-9525. DOI: 10.1083/jcb.200405061. URL: <https://www.ncbi.nlm.nih.gov/pubmed/15353546%20https://www.ncbi.nlm.nih.gov/pmc/PMC2172129/>.
- [100] Jürgen Wendland and Andrea Walther. “Ashbya gossypii: a model for fungal developmental biology”. In: *Nature Reviews Microbiology* 3.5 (2005), pp. 421–429. ISSN: 1740-1534. DOI: 10.1038/nrmicro1148. URL: <https://doi.org/10.1038/nrmicro1148>.
- [101] Stefaan Wera, Jan C T Bergsma, and Johan M Thevelein. “Phosphoinositides in yeast : genetically tractable signalling”. In: 1 (2001), pp. 9–13.
- [102] Thomas Wilhelm. “The smallest chemical reaction system with bistability”. In: *BMC Systems Biology* 3.1 (2009), p. 90. ISSN: 1752-0509. DOI: 10.1186/1752-0509-3-90. URL: <http://www.biomedcentral.com/1752-0509/3/90>.
- [103] Zhanghan Wu et al. “Membrane shape-mediated wave propagation of cortical protein dynamics”. In: *Nature Communications* 9.1 (2018), p. 136. ISSN: 2041-1723. DOI: 10.1038/s41467-017-02469-1. URL: <https://doi.org/10.1038/s41467-017-02469-1>.
- [104] Wen Xiong and James E Ferrell Jr. “A positive-feedback-based bistable ‘ memory module ’ that governs a cell fate decision”. In: 426.November (2003), pp. 460–465. DOI: 10.1038/nature02119.1..
- [105] Liang Yang, Weiliang Mo, and Xiaolan Yu. “Reconstituting Arabidopsis CRY2 Signaling Pathway in Mammalian Cells Reveals Regulation of Transcription by Direct Binding of CRY2 to DNA Report Reconstituting Arabidopsis CRY2 Signaling Pathway in Mammalian Cells Reveals Regulation of Transcription by Direct Binding of CRY2 to DNA”. In: *CellReports* 24.3 (2018), 585–593.e4. ISSN: 2211-1247. DOI: 10.1016/j.celrep.2018.06.069. URL: <https://doi.org/10.1016/j.celrep.2018.06.069>.

- [106] T Yoko-o et al. “The putative phosphoinositide-specific phospholipase C gene, PLC1, of the yeast *Saccharomyces cerevisiae* is important for cell growth.” eng. In: *Proceedings of the National Academy of Sciences of the United States of America* 90.5 (Mar. 1993), pp. 1804–1808. ISSN: 0027-8424 (Print). DOI: 10.1073/pnas.90.5.1804.
- [107] M. Zamparo et al. “Dynamic membrane patterning, signal localization and polarity in living cells”. In: *Soft Matter* 11.5 (2014), pp. 838–849. ISSN: 1744-683X. DOI: 10.1039/C4SM02157F. URL: <http://xlink.rsc.org/?DOI=C4SM02157F>.
- [108] Felipe E Zilly et al. “Ca<sup>2+</sup> induces clustering of membrane proteins in the plasma membrane via electrostatic interactions”. eng. In: *The EMBO journal* 30.7 (Apr. 2011), pp. 1209–1220. ISSN: 1460-2075. DOI: 10.1038/emboj.2011.53. URL: <https://www.ncbi.nlm.nih.gov/pubmed/21364530><https://www.ncbi.nlm.nih.gov/pmc/articles/PMC3094119/>.
- [109] A M Zorn and P A Krieg. “Developmental regulation of alternative splicing in the mRNA encoding *Xenopus laevis* neural cell adhesion molecule (NCAM).” eng. In: *Developmental biology* 149.1 (Jan. 1992), pp. 197–205. ISSN: 0012-1606 (Print).